RANDOM VIBRATION ANALYSIS OF AN OPTOMECHANICAL SYSTEM
MOUNTED ON AN AIR PLATFORM

A THESIS SUBMITTED TO
THE GRADUATE SCHOOL OF NATURAL AND APPLIED SCIENCES
OF
MIDDLE EAST TECHNICAL UNIVERSITY

BY

EGE YALÇIN

IN PARTIAL FULFILLMENT OF THE REQUIREMENTS
FOR
THE DEGREE OF MASTER OF SCIENCE
IN
MECHANICAL ENGINEERING

AUGUST 2022

Approval of the thesis:

**RANDOM VIBRATION ANALYSIS OF AN OPTOMECHANICAL
SYSTEM MOUNTED ON AN AIR PLATFORM**

submitted by **EGE YALÇIN** in partial fulfillment of the requirements for the degree
of **Master of Science** in **Mechanical Engineering, Middle East Technical
University** by,

Prof. Dr. Halil Kalıpçılar
Dean, Graduate School of **Natural and Applied Sciences**   _____

Prof. Dr. Mehmet Ali Sahir Arıkan
Head of the Department, **Mechanical Engineering**   _____

Prof. Dr. Mehmet Çalışkan
Supervisor, **Mechanical Engineering, METU**   _____

_____

Examining Committee Members:

Prof. Dr. Yiğit Yazıcıoğlu
Mechanical Engineering, METU   _____

Prof. Dr. Mehmet Çalışkan
Mechanical Engineering, METU   _____

Assoc. Prof. Dr. Mehmet Bülent Özer
Mechanical Engineering, METU   _____

Assoc. Prof. Dr. Kıvanç Azgın
Mechanical Engineering, METU   _____

Asst. Prof. Dr. Melih Çakmakcı
Mechanical Engineering, Bilkent University   _____

Date: 18.08.2022

I hereby declare that all information in this document has been obtained and presented in accordance with academic rules and ethical conduct. I also declare that, as required by these rules and conduct, I have fully cited and referenced all material and results that are not original to this work.

Name Last name : Ege Yalçın

Signature :

ABSTRACT

RANDOM VIBRATION ANALYSIS OF AN OPTOMECHANICAL SYSTEM MOUNTED ON AN AIR PLATFORM

Yalçın, Ege
Master of Science, Mechanical Engineering
Supervisor : Prof. Dr. Mehmet Çalışkan

August 2022, 131 pages

Vibrations in operating environment cause unwanted motion of the optical components of an optomechanical system mounted on air platform, downgrading its performance. This performance reduction is described by two optical parameters, namely, line-of-sight jitter and reduction in modulation transfer function (MTF). However, relatively few studies have been conducted on the prediction of these parameters, forcing engineers to rely on experimental data obtained from the physical model. By the time optomechanical system design is already completed and its physical model is manufactured, it usually proves to be expensive to apply any necessary changes to improve vibration performance.

Amplitude of a random vibration signal cannot be foreseen and predicted exactly. It behaves like a combination of many sinusoidal signals with differing frequencies and phases, which is a model of real-life operational conditions. Subjected to a stationarity test, Fourier transform is applied to this signal while it can be considered as a single PSD profile with a particular spectral energy distribution over frequency range of interest.

In this study, it is first verified that the time domain acceleration data acquired from the operating environment is stationary. Secondly, a finite element analysis model of the optomechanical system of concern is constructed. Then, using the results of the finite element analysis, the two optical parameters are calculated by a specialized analysis software. The calculated MTF reduction is tried to be verified through experimental measurements. Thus, it is aimed to predict MTF reduction accurately by using the appropriate simulation software at early stages of a project.

Keywords: Random Vibration, Optomechanical System, Modulation Transfer Function, Line-of-Sight, Jitter

ÖZ

HAVA PLATFORMUNA YERLEŞTİRİLEN BİR OPTOMEKANİK SİSTEMİN RASTLANTISAL TİTREŞİM ANALİZİ

Yalçın, Ege
Yüksek Lisans, Makina Mühendisliği
Tez Yöneticisi: Prof. Dr. Mehmet Çalışkan

Ağustos 2022, 131 sayfa

Çalışma ortamındaki titreşimler, hava platformuna yerleştirilmiş bir optomekanik sistemdeki optik parçalarda istenmeyen harekete yol açarak sistemin performansını düşürebilir. Performanstaki bu düşüşü tanımlayan iki optik parametre vardır. Bunlar, görüş hattındaki oynama ve modülasyon transfer fonksiyonunun değerindeki azalmadır. Ancak bu parametrelerin kestirimi üzerine nispeten az sayıda çalışma yapılmıştır. Bu durum mühendisleri mecburen fiziksel modelden elde edilen deneysel verilere bağımlı hale getirmektedir. Optomekanik sistemin tasarımı tamamlandıktan ve fiziksel model üretildikten sonra titreşim performansını artırmanın maliyeti ise genellikle yüksek olmaktadır.

Rastlantısal bir titreşim sinyalinin genliği tam olarak öngörülüp kestirilemez. Bu sinyaller farklı frekans ve fazlara sahip birçok sinüsoid sinyalin kombinasyonu gibi davranır. Bu durum, gerçek hayattaki çalışma ortamının bir modelidir. Durağanlık testinden geçen bu sinyale Fourier dönüşümü uygulandıktan sonra sinyal, ilgilenilen frekans aralığında belirli bir spektral enerji dağılımına sahip tek bir PSD profili olarak düşünülebilir.

Bu çalışmada önce, çalışma ortamından alınan zaman bölgesindeki ivme verisinin durağan olduğu doğrulanmıştır. İkinci olarak, ilgilenilen optomekanik sistemin sonlu eleman analiz modeli oluşturulmuştur. Ardından sonlu eleman analiz sonuçları kullanılarak iki optik parametre özel bir analiz yazılımında hesaplanmıştır. Hesaplanan MTF düşüşü, deneysel ölçümlerle doğrulanmaya çalışılmıştır. Böylece MTF düşüşünün projenin erken safhalarında uygun simülasyon yazılımı kullanılarak doğru bir şekilde kestirilmesi hedeflenmiştir.

Anahtar Kelimeler: Rastlantısal Titreşim, Optomekanik Sistem, Modülasyon Transfer Fonksiyonu, Görüş Hattı, Titreme

To my family

ACKNOWLEDGMENTS

TABLE OF CONTENTS

LIST OF TABLES

LIST OF FIGURES

FIGURES

xviii

LIST OF ABBREVIATIONS

ABBREVIATIONS

CAD: Computer-aided design

CL: Converging Lens

DC: Direct current

DOF: Degree of freedom

FEA: Finite element analysis

FOV: Field of view

FPA: Focal plane array

FRF: Frequency response function

Hz: Hertz

IR: Infrared

LI-TX: Decenter error of line-of-sight in image space along x-axis

LI-TY: Decenter error of line-of-sight in image space along y-axis

LI-TV: Vector sum of decenter error in image space in xy-plane

LI-RX: Angular line-of-sight error in image space about x-axis

LI-RY: Angular line-of-sight error in image space about y-axis

LI-RV: Vector sum of angular line-of-sight error in image space in xy-plane

LL: Large Lens

LO: Low outgassing

LO-RX: Angular line-of-sight error in object space about x-axis

LO-RY: Angular line-of-sight error in object space about y-axis

LO-RV: Vector sum of angular line-of-sight error in object space in xy-plane

LoS: Line-of-sight

LOSRAY: The ray that is traced by the software through the optical line-of-sight

Lp/mm: Number of line pairs per millimeter

M1: Mirror 1

M2: Mirror 2

MFL: Movable Focus Lens

MFoG: Movable Focus Group

MTF: Modulation transfer function

MWIR: Midwave infrared

MZoG: Movable Zoom Group

MZL: Movable Zoom Lens

ND: Non-dripping

NFOV: Narrow field of view

ProE: ProEngineer

PSD: Power spectral density

RMS: Root mean square

SDOF: Single degree-of-freedom

WFOV: Wide field of view

LIST OF SYMBOLS

SYMBOLS

dB: Decibel

dBfs: Decibels relative to full scale

δ_θ: Finite amount of disturbance of the optical surface

E: Young's modulus (also known as "modulus of elasticity")

f: Frequency in Hertz

g: Gravitational acceleration of Earth (9.81 m/s^2)

H(f): Harmonic frequency response function

ρ: Density

σ: One root-mean-square value, or "one sigma"

$S_x(f)$: Input random PSD profile

$S_y(f)$: Random PSD response

T: Integration time in seconds

υ: Poisson's ratio

W_d: Jitter weighting factor

CHAPTER 1

INTRODUCTION

This thesis involves the analysis and testing of the effects of random vibrations on the optical performance of an optomechanical system mounted on an air platform. Therefore, the introduction of the thesis focuses on the two main concepts, which are random vibrations and optomechanical systems.

1.1   Random Vibrations

Vibrations are oscillations that occur about an equilibrium state of a dynamic system. Vibrations can be classified as "deterministic" or "random" depending on their profiles or signatures. In case of harmonic vibrations, which is a very special form of periodic vibration with a single frequency, the time signature repeats itself in a constant period of time. Thus, sinusoidal or harmonic vibration includes one single pre-dominant frequency only. Random vibrations, however, are vibrations whose amplitude at a given time cannot be foreseen and predicted exactly. They can be visualized as the combination of many different sinusoidal vibration profiles with different amplitudes, frequencies and phases. Thus, random vibrations simulate physical operating conditions more realistically and they are capable of exciting more than one resonant frequency in a structure at the same time as opposed to sinusoidal or single frequency excitation owing to their rich frequency contents, enabling more precise structural and assembling diagnosis. Random vibrations can be modelled statistically by assuming that they are stationary, which implies that their statistical properties like mean and standard deviation as well as higher order properties do not change depending on the time at which they are sampled or observed. Hence, the response of a structure to a specified random excitation can be

readily estimated on computer by using a proper computer-aided design (CAD) model of the structure and a general purpose finite element analysis software. Figure 1.1 shows examples of a sinusoidal and random vibration signal.
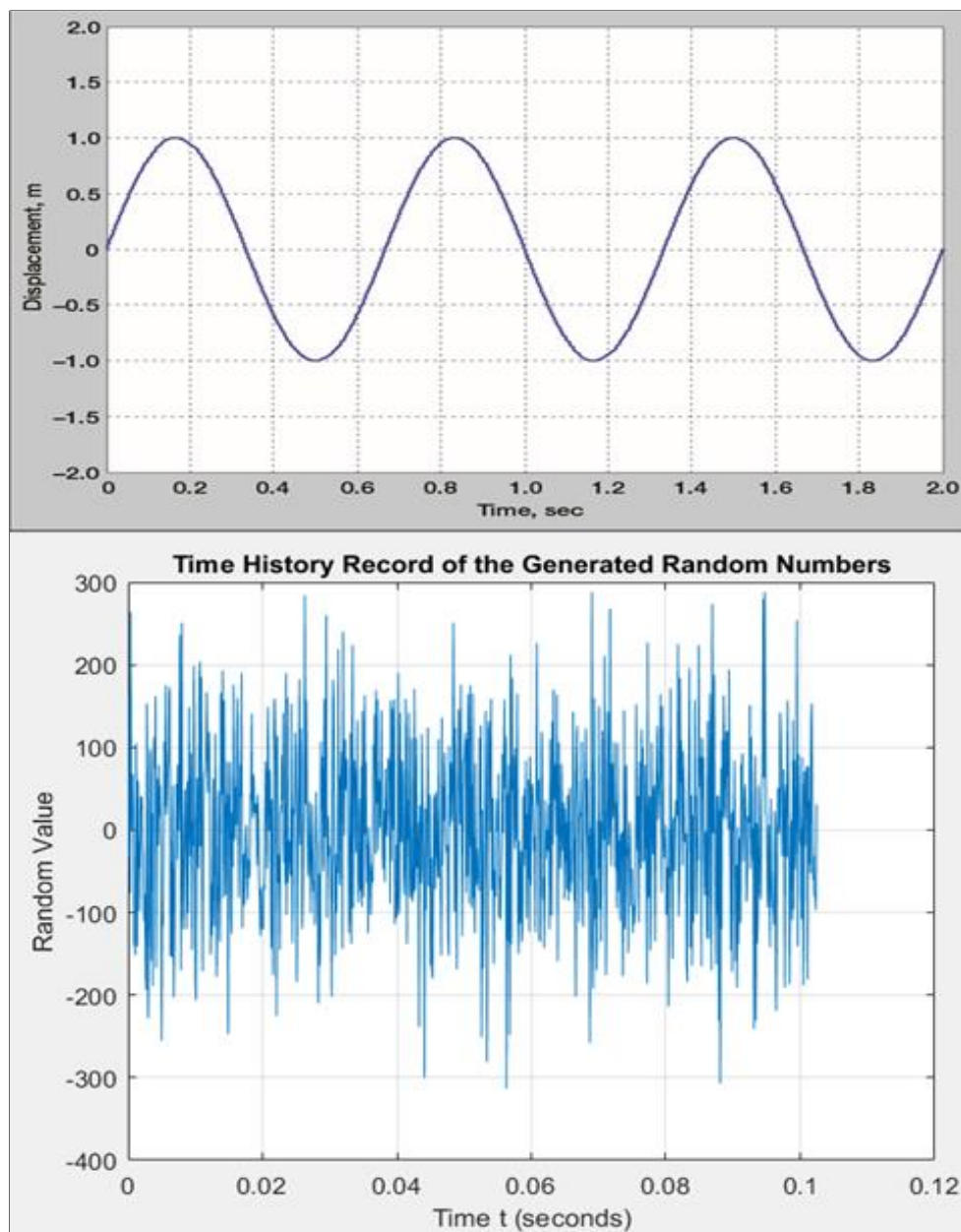
Figure 1.1. Examples of harmonic (top) and random (bottom) vibration signals

2

The acceleration responses of different points in the structure to random vibrations can also be measured in the form of time histories by an accelerometer. During this measurement, the random vibration excitation is applied to the structure by a shaker or by a sound signal in the case of acoustically induced vibrations. This vibratory response is converted into information in frequency domain by applying Fourier transformation. The plot of the energy associated with this data with respect to frequency is known as the Power Spectral Density (PSD). The unit of PSD is the power in square of the unit divided by frequency in Hertz or radians per second. An example of a PSD plot is shown in Figure 1.2. The square root of the area under PSD gives the root-mean-square (RMS) value of the data over the given frequency range. It represents the distribution of power or energy with respect to frequency. In the defense industry, standards such as MIL-STD-810 have been written by the Department of Defense of the United States. In these standards, the unit "acceleration squared per Hz" or the normalized unit "g squared per Hz" is often used [1]. By assuming the PSD to show normally distributed Gaussian behavior as in Figure 1.3, it is estimated that the peak response amplitude is less than one RMS 68.3% of the time, less than two RMS 95.4% of the time and less than three RMS 99.7% of the time. Doyle et al. [2] note that designing a structure for five RMS levels is an accepted practice because there is a risk of encountering amplitudes higher than three RMS as the duration of random excitation increases.
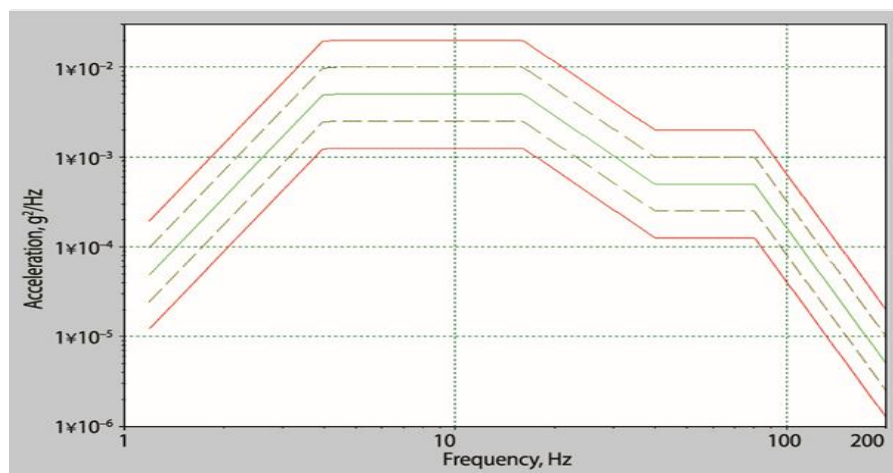
Figure 1.2. Example of a Power Spectral Density plot
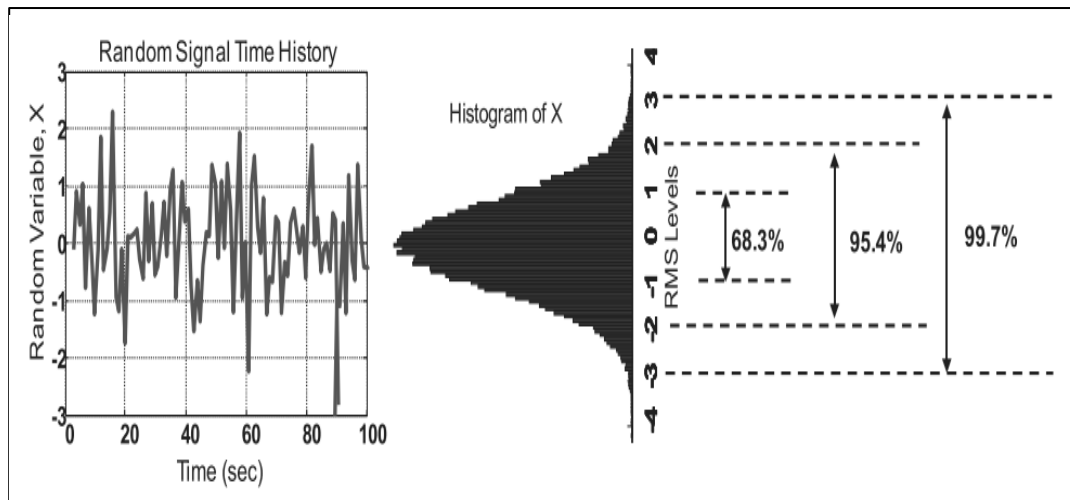
Figure 1.3. Random variable with zero mean and RMS equal to one [2]

1.2 Optomechanical Systems

Random vibration response analysis and measurement have applications in many mechanical structures, one of which is optomechanical systems. An optomechanical system is an assembly of optical and mechanical components that enable enhanced vision for human users. These enhancements include wide or narrow fields of view, different amounts of mechanical or digital magnification, and the ability to perceive objects that emit electromagnetic energy in wavelengths such as infrared (3 to 5 or 8 to 12 micrometers) that are not normally visible to the naked human eye. Optomechanical systems can be mounted on the platforms of many different warfare vehicles such as tanks, ships, and aircraft. The random vibration PSD that is applied to an optomechanical system depends on the vehicle or platform on which it is mounted. This thesis focuses on an optomechanical system that is mounted on an air platform for demonstration purposes. The methodology could be applied to any platform though. For any mission critical platform, the primary and most accurate source of input PSD is the time-based acceleration data collected during the operation of the real-life platform. Even though standard input PSD's have also been included in the MIL-STD-810 standard for several well-known American

4

aircraft models, they are suitable for only preliminary or rough modelling and testing [1].

1.2.1   Line-of-Sight Jitter

As opposed to most other structures, the main concerns in an optomechanical system under random excitation are not only structural integrity but also optical performance or accuracy, which makes it a special application area. In other words, while it is crucial for an optomechanical system to maintain its structural integrity (i.e. survive) during extreme vibration conditions, it is equally important for that system to maintain an acceptable optical performance during less extreme but much more frequent random vibrations. Such operational random vibration causes the optical components, usually lenses, mirrors and prisms, to move. This produces jitter in the line of sight, both in image space and object space. Jitter is the rapid oscillation of the line-of-sight about its nominal position either in translation or rotation. Some of the components of this jitter are shown in Figure 1.4 [2]. The components shown in Figure 1.4 include translations in image space along the x and y-axes (LI-TX and LI-TY), rotation in image space about the x-axis (LI-RX), and rotation in object space about the x-axis (LO-RX).

Figure 1.4. Nominal line-of-sight (a) and line-of-sight of a disturbed optical surface (b)

The line of sight is the hypothetical line within the optomechanical system along which rays from an illumination source proceed through the optical components and eventually focus on the sensor. The sensor is the electro-optical component that forms the image. The plane in the sensor on which the image is formed is the focal plane array (FPA), and it constitutes the image space. Random vibration may cause line of sight to translate either along the optical axis, which causes defocus (loss of focus), or in the image space in two directions perpendicular to the optical axis, which results in decenter. These translations are expressed in terms of micrometers on the FPA. The object space is the physical space in which the object that is tried to be perceived exists. Random vibration causes the line of sight to rotate about the two axes perpendicular to the optical axis. This rotation is expressed in microradians [3]. Special software can be used to calculate these errors. The errors can also be measured experimentally in terms of number of pixels, which can be converted to micrometers or radians, by directing the optomechanical system towards a point target in a collimator as the shaker applies random PSD to it.

1.2.2   MTF Reduction

The effect of random vibration on the optical performance of a system can also be quantified by the change in its modulation transfer function (MTF). The MTF of an optical system is a dimensionless quantity that ranges from 0 to 1 and determines how well the optical system can resolve the contrast in a pair of adjacent black and white lines. The terms "wavenumber" and "spatial frequency" both have the unit of reciprocal length. However, "wavenumber" specifically defines the spatial frequency of a physical wave while the term "spatial frequency" applies to all structures that are periodic across space. So, MTF is a function of spatial frequency, which can be expressed as the number of line pairs (lp) in 1 mm when used in optical performance measurement applications. As the spatial frequency increases, the black-white line pairs get closer to each other, and so it is harder for the optical system to resolve them; reducing MTF. In the optical design software, the maximum possible MTF curve for a given optical system is calculated. However, this MTF is

6

ideal; and it cannot be exactly achieved in real life due to factors such as microscopic surface errors on the optics that occur during manufacturing and slight deviations in the tolerances of the mechanical components that hold these optics. Random vibrations and other operational conditions further reduce this MTF [2].

The response PSD of the line-of-sight to a specified random PSD input is equal to the product of the square of the modulus of the harmonic FRF and the input PSD. The harmonic FRF is defined as the ratio of the steady-state response of a system to an applied sinusoidal input, which may be a force, an imposed displacement, or any other quantity [28]. Figure 1.5 illustrates the calculation of the response to the random PSD input [28].
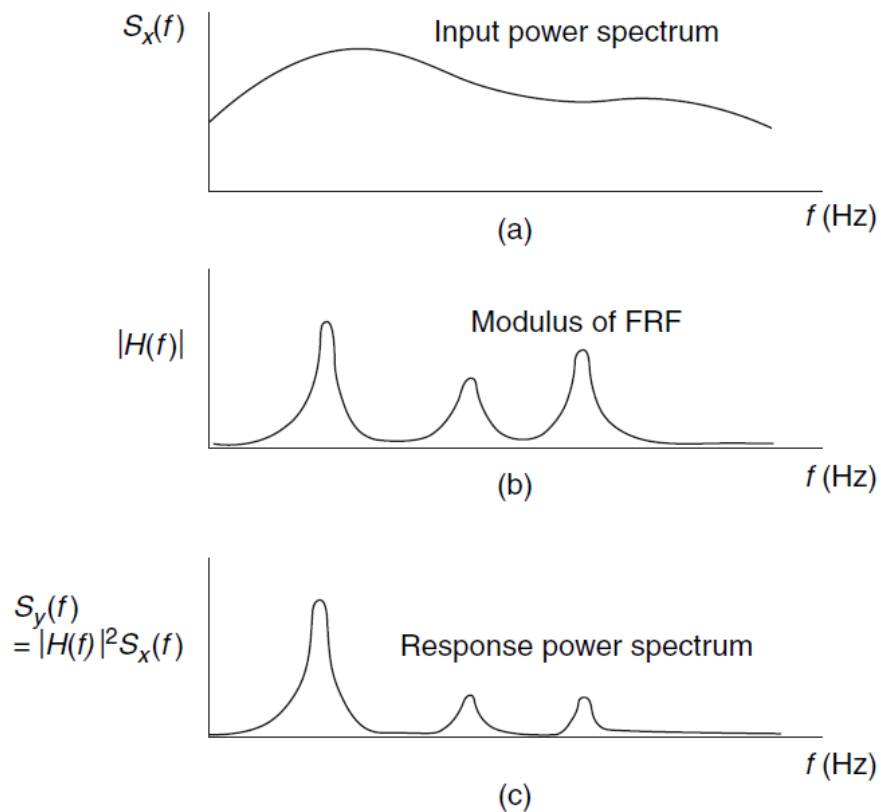
Figure 1.5. Calculation of the response PSD from input PSD and system FRF [28].

The root-mean-square of this response PSD is calculated by taking the square root of the area under it. During this process, phase information of the random

response data is lost; and this information is vital for correctly determining the effects of random excitation on optical performance. Even if the nodal RMS values of displacement of an optical surface remain the same, it is the phase information that reveals how this displacement is distributed along the nodes. Equal displacements with different distributions have dramatically different effects on optical performance. General purpose finite element software cannot distinguish between these distributions [23]. However, specific software has been developed to decompose random response displacement of each node into rigid-body motion and elastic deformation, which have different effects on optical performance [3, 23]. The schematics of these motions are shown in Figure 1.6.

(a)   (b)

Figure 1.6. Rigid-body motion (a) and elastic deformation (b) on the surface of an optical component under random vibration [3].

There are also optical parameters, such as integration time, that affect how the response PSD is processed in order to calculate its effect on the optical performance. The integration time is the length of time for which the detector can collect photons from the illumination source until it forms an image. Depending on the integration time, the PSD response of the line of sight to random excitation can be divided into slow drift response and fast jitter response with a weighting factor [3]. Fast jitter corresponds to the frequencies in the random response that are faster than the detector integration time so that the full extent of the jitter can be seen constantly in the image. The fast jitter component causes the reduction in MTF. The MTF reduction due to the fast jitter is an exponential function of the forcing frequency in Hertz, and its expression involves both this frequency and the RMS of the jitter component of the random response (Equations 1.1 through 1.6). The reduced MTF of the optical system due to random vibration is calculated by

8

multiplying the nominal MTF that is not subjected to any physical operational conditions by the MTF effect due to the jitter [3].

Equation (1.1):

$$S_y(f) = |H(f)|^2 * S_x(f)$$

Equation (1.2):

$$\Delta_{rms} = \sqrt{\int_0^\infty (W_d(f) * S_y(f))df}$$

Equation (1.3):

$$W_d(f) = 1 - \frac{2(1 - \cos(C))}{C^2}$$

Equation (1.4):

$$C(f) = 2\pi f T$$

Equation (1.5):

$$MTF_{JitterRandom}(f) = e^{-2\pi^2 \Delta_{rms}^2 f^2}$$

Equation (1.6):

$$MTF_{Net}(f) = MTF_{Nominal} * MTF_{JitterRandom}(f)$$

In Equations 1.1 through 1.4, T denotes the detector integration time in seconds, f denotes the frequency in Hertz, W_d denotes the jitter weighting factor, Δ_{rms} denotes the root-mean-square of the jitter component of the random response $S_y(f)$, $H(f)$ denotes the harmonic frequency response function, and $S_x(f)$ denotes the PSD profile of the input random excitation.

Figure 1.7 shows the plots of the jitter and drift weighting functions on the same set of axes [3].
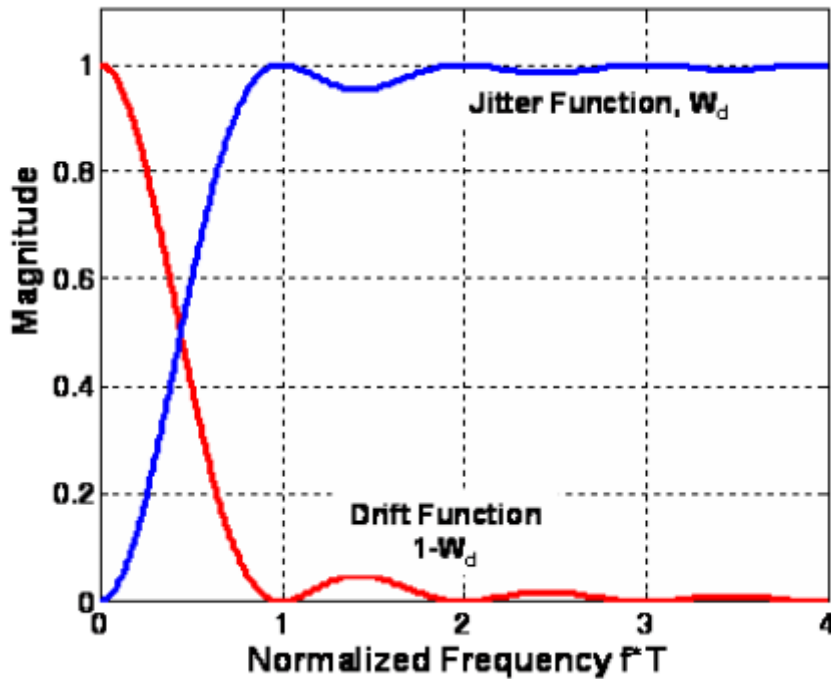
Figure 1.7. Drift and jitter weighting functions

Both line-of-sight errors and reduction in the MTF of an optomechanical system can be determined in two ways. The first way is to estimate these quantities by finite element and optomechanical analysis software, and the second way is to measure them by the actual optomechanical system and appropriate force exciters, transducers, and optical measurement devices like collimators. This thesis considers the MTF reduction in particular because it is the primary optical performance parameter in most applications in ASELSAN. So, in this thesis, it is aimed to first estimate MTF reduction by software and then verify these results through measurements on the actual optomechanical system. However, other parameters estimated through the software, such as line-of-sight jitter and percent contributions of modes to this jitter, are also presented and discussed to obtain additional insight into how optical performance under vibration can be further improved during early design stage.

1.3 Motivation and Aim

Optomechanical systems are very frequently mounted on aircrafts and other vehicles to provide additional, enhanced sight of the environment to the pilot or driver during operations. Vibrations in the operating environment cause the optical or mechanical components of an optomechanical system to move, reducing optical performance. The excitation usually propagates through the micron or millimeter order-of-magnitude clearances between the mechanical parts themselves or the mechanical and optical parts. As discussed in Section 1.2, effect of vibrations on optical performance is described by two parameters, which are line-of-sight jitter and MTF reduction. There have been relatively few literature on the prediction of the effect of mechanical vibration on optical performance. As a result, engineers usually have to rely on the experimental data, which is obtained after the design is already completed and manufactured. At this point, it is more difficult and expensive to apply changes to improve the optical performance under vibrations. This inconvenience is the main motivation behind writing this thesis.

The aim of this thesis is to predict the MTF reduction in optomechanical systems under vibration, which is the primary optical parameter for many applications in ASELSAN, by using simulation software. The ultimate aim of the thesis is to draw attention to the research field of predicting optical parameters under vibrations and other dynamic loads by using specialized software, and to the currently available licensed software like SigFit. Thus, consideration of optical performance under vibration can be pushed to the earlier stages of a project's lifecycle.

1.4 Outline and Workflow of the Thesis

In Chapter 1, an introduction to the two main aspects of the thesis topic, which are random vibration and optomechanical systems, is presented. The terminology and measurement methods of random vibration are summarized, and it is highlighted how random vibration is involved in the optomechanical design

efforts. The definition of an "optomechanical system" is explained. It is noted that this thesis deals with an optomechanical system mounted on the platform of an air vehicle, i.e. an air platform and so it is subject to the MIL-STD-810 environmental testing standard. Then, the two main effects of random vibration on any optomechanical system, which are line-of-sight errors and reduction in MTF, are explained. Finally, it is emphasized that both of these quantities can be calculated through software or measured by exciting the actual optomechanical system with appropriate force exciters, transducers and collimators. It is noted that this thesis attempts to verify the simulation of the MTF reduction parameter in particular through the measurements taken from the actual system. The motivation for writing the thesis and aim of the thesis are also presented.

In Chapter 2, a literature survey that highlights the most significant studies and conference papers related to the topic is presented. The necessity and significance of the thesis topic relative to this survey are emphasized. In the literature survey, it is found that while there are numerous papers related to digital algorithms that are used to compensate the effects of vibration on image or film scripts or video material electronically, few papers consider the mechanical effects of vibration on the structural or optical performance of an optomechanical system, which is the topic of this thesis. A complex optomechanical system has been focused on in two papers found in this survey. The first one [15] considers the effects of vibration on both the structural integrity and optical performance of the system. However, it belongs to 1995, when the finite element analysis and measurement capabilities were not fully flourished. The other paper [21] considers the image degradation in a complicated astronomical telescope due to vibration. The systems considered in remaining papers and theses are relatively simple. However, all papers that have been found in this literature survey provide useful methods and conclusions that can be exploited in this thesis as well, since similar vibration analysis and measurement methods can be used for most dynamic systems with small but ingenious modifications. These modifications may include reasonable simplifications and assumptions as well. In this thesis, a moderately complex optomechanical system mounted on an air platform is selected for such an analysis.

In Chapter 3, random vibration analysis of the air platform optomechanical system on ANSYS is presented. First, the simplifications and assumptions that are applied to the CAD model prior to the ANSYS analysis are explained. The first simplification is the consideration of motors and electronic components which do not directly contribute to the structural stiffness of the optomechanical system as point masses applied at their centers of gravity. The second simplification is the removal of thin mechanical components and fasteners that also do not directly affect structural stiffness and unnecessarily increase the computation time. The adhesives are modelled as pinball-radius bonded contact regions. Once the CAD model is constructed and meshed successfully, modal analysis is performed without pre-stress to determine the first 20 natural frequencies and mode shapes of the optomechanical system. The first natural frequency is expected to be above 100 Hz to comply with the design requirement. Then, harmonic analysis is performed to determine the frequency response function of the optomechanical system. This response is used to calculate the line-of-sight errors and reduction in MTF as explained in Chapter 1. Before moving onto random vibration analysis, the stationarity of the time record that has been collected from the actual air platform is verified by using the Reverse Arrangements Test. Finally, random vibration analysis is through, where the input PSD is the vibration data that was obtained from a real-life air platform. The deformations on the lens and mirror surfaces due to this PSD excitation are obtained. This deformation data is used in the appropriate optical and optomechanical analysis software, which is explained in Chapter 4. This procedure is repeated for another configuration of the finite element model described above, where the pinball-radius bonded contact of one of the lenses is replaced with an elastic adhesive model.

In Chapter 4, by employing the deformation data obtained in Chapter 3, computation of the effects of random vibration on the optical performance of the system is presented for both configurations of the finite element model. The results of the ANSYS analysis are imported into the appropriate analysis software to estimate the effect of the lens and mirror surface deformations due to random vibration on the optical performance of the system. The software generated tables of numerical results, which include the line-of-sight jitter, the contributions of each

mode to different jitter components, and the reduction in MTF. These results are examined in detail, and conclusions are reached regarding to the change in optical performance due to random vibration. The percent contributions of modes are examined together with the mode shapes found by ANSYS modal analysis. The line-of-sight jitter displacement components are compared with the random deformation results found by ANSYS random response analysis. However, the MTF reduction needed to be verified experimentally, which is the focus of Chapter 5.

In Chapter 5, experimental measurements of the MTF under random vibration due to random excitation are presented. A physical optomechanical system is placed on a shaker and in front of one of the collimators in ASELSAN's environmental condition lab. The optomechanical system is powered as in its operational environment, and the system is directed to look at a target in a collimator as video data is collected from it on a connected monitor. Half-moon target is used for MTF measurement. Then, the shaker beneath the system is excited with the same PSD that was used in the ANSYS analysis. Again, conclusions are reached regarding to the change in optical performance. Then, this MTF data is compared with that obtained from the software in Chapter 4, which is the topic of the last chapter, Chapter 6.

In Chapter 6, the results of Chapters 4 and 5 are compared and the possible reasons for the discrepancies between these results are discussed. The conclusions are also included in this final chapter. The MTF reduction under random vibration calculated by the analysis software is much lower than that measured experimentally. Both the finite element method and the experiments have their own shortcomings. Nevertheless, this study is an attempt to replicate the testing procedure in the simulations at the early design phase of a project; and it provides a solid basis and methodology on which similar, more sophisticated studies can be conducted.

The workflow of the thesis, which is closely related to the outline described above, is schematized in Figure 1.8.
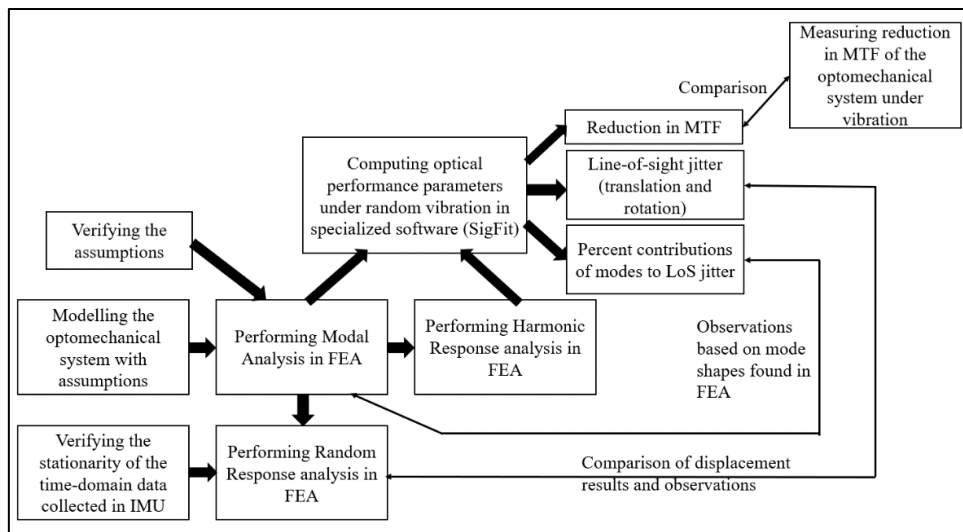
Figure 1.8. Workflow of the thesis

CHAPTER 2

LITERATURE REVIEW

With the development of theoretical and computational capabilities in the 1980's, more studies have been conducted on the effects of random vibrations on the structural integrity or optical performance of different optical systems. These systems include an airborne infrared imager, a satellite imager and an astronomical telescope. The main methods associated in these studies are finite element analysis and testing. Doyle and Cerrati et al. and Avşar have tried to verify the finite element analysis results from the CAD model of the system with the test results from the actual system, with moderate success. There are also studies where the authors have developed mathematical formulas to calculate the reduction in the MTF of the system due to low or high frequency vibrations [4-7]. These studies are cited frequently in later studies [8-9] and are employed in the programming of optomechanical design software like SigFit by the Sigmadyne company [2]. However, many of these studies are related to the digital algorithms and control systems [9, 25-27] that are used to process and enhance the image or film scripts or video material electronically. Such approaches are not directly related to the topic of this thesis. Several textbooks related specifically to the optomechanical design efforts against operational conditions like vibration, shock and thermal loads have also been published [2, 10-14]. However, as the summaries of several papers below imply, recently there does not appear to exist a significant effort to apply this information to an actual, moderately complicated airborne reconnaissance system, by the currently available computation and testing capabilities. Even if such studies exist, they are most likely stored as confidential internal documents by defense industry or other private companies. This thesis attempts to obtain non-confidential, general conclusions that

are useful for not just the student's company but also for the whole defense industry and academia as reference.

In 1995, Doyle and Cerrati et al. [15] developed an MSC/NASTRAN finite element model of the gimbal assembly of the Airborne Infrared Imager (AIRI) to predict its structural response under operational random vibration conditions. They entered the flight vibration data collected from the AIRI mock-up as input. The values that they predicted by the software included the first four natural frequencies, the angular error rates about the elevation and azimuthal axes in degrees per second and the line-of-sight jitter (angular positioning error) of the gimbal assembly in microradians. They, then, performed experimental modal analyses and shaker tests to collect experimental data and compare them with those predicted by the software. They mounted accelerometers onto the gimbal assembly and the rate sensing gyro to the top of the elevation bridge. A white-noise with a root-mean square acceleration of 0.78g of random input from 10 Hz to 2000 Hz was assigned to the three axes of the AIRI sensor suit. The accelerometers acquired the PSD response of the gimbal assembly to this input; and the rate sensing gyros recorded the angular error rates and the line-of-sight jitter about the elevation and azimuthal axes due to this random vibration. The authors performed this procedure for both the original and structurally stiffened designs of the gimbal assembly. By comparing the results for these two designs, they noted that the stiffened design had higher first natural frequency, and both the elevation and azimuthal angular rate errors in degrees per second and line-of-sight jitter in microradians were considerably reduced in the stiffened design. Finally, the authors noted that the discrepancies between the values predicted by finite element model and the values measured experimentally were due to the finite element model covering a wider range of frequencies (up to 300 Hz) as opposed to the gyro which could not sense rates above 100 Hz.

In 2007, Bonin and McMaster [16] optimized the design of a simple Cassegrain telescope structure subjected to a specified random vibration PSD in single direction. The telescope structure consisted of a primary mirror, a secondary mirror and a mechanical component called "spider" that held these two mirrors together. The authors first performed random vibration response analysis of this

structure on the NX Nastran finite element analysis (FEA) software. They conducted this analysis by two different ways, one of which was static and the other was dynamic. The surface deformations of the mirrors calculated by the FEA software with both methods were converted into Zernike polynomials by the SigFit software package, enabling it to determine their effects on optical performance. In the static method, it was assumed that the structure was a single degree-of-freedom (SDOF) system and that the applied random vibration PSD had a flat, constant and lightly damped value around the resonant frequency. With this method, the static G-load equivalent of the random vibration PSD was calculated by PSD input at resonant frequency in g squared per Hz, the resonance frequency of the so-assumed SDOF system in Hz, and the transmissibility of this system. The authors first found the first three natural frequencies of the actual structure by a FE analysis. Then, they looked up the PSD input value corresponding to the first natural frequency of 468 Hz in the input random PSD that they planned to apply. Finally, they approximately calculated the transmissibility of the SDOF system by considering it as a lightly-damped "beam-type" structure. Thus, with these numerical data in hand, the equivalent static G-load was found. This load was then applied in the X direction (one of the two axes perpendicular to the optical axis) and random response analysis was performed on the FEA model. In the dynamic method, the authors directly used the three mode shapes for random response analysis. The authors observed very little correlation between the results obtained by the two methods, which they noted might be due to the model's behavior not matching the assumptions required for the static analysis. Ultimately, the authors used the dynamic method to optimize their design because they considered it to be more rigorous.

In 2008, Avşar [17] analyzed the random vibration response of a very simple optomechanical system that was designed at ASELSAN and consisted of one lens, one case, and a layer of elastomer. Avşar determined the predicted natural frequencies and PSD responses by ANSYS, a commercial FEA software, in the frequency range from 10 to 500 Hz. Then, he verified these results with experimental measurements. The measurements were acquired from a modal test and the random vibration test. The acceleration data in three mutually perpendicular axes were

collected by two triaxial accelerometers. One accelerometer was placed on the vibration table to verify the vibration profile input to the optomechanical system, and the other was placed on the system to collect vibration data. The discrepancy in the results of the modal analysis between finite element and experiments did not exceed 10% whereas the discrepancy in the results of the random vibration analysis did not exceed 11.4%, which Avşar considered acceptable. As the main reason for this difference, he noted that in the experiments, he could not place the accelerometer at the exact same point as the finite element model due to the accelerometer's size. Avşar then used the Zemax optical design software to determine the reduction in system MTF caused by specified amounts of decenter motions in mm and tilt motions in degrees (the two main motions of the lens caused by vibration). He, then determined the amount of decenter and tilt motions of the system caused by the AH-1 helicopter vibration profile by random vibration analysis in ANSYS; and compared it with the table of MTF reductions he had obtained from Zemax to see how much MTF was reduced for this system due to random vibration. Thus, Avşar verified that optical performance was degraded when subjected to vibration environment.

In 2012, Ünal [18] measured the angular movement of mirrors in microradians in the prism and mirror mounts of a laser system under vibration and shock by an autocollimator at ASELSAN. For these measurements, he manufactured five different optomechanical barrel designs. For each design, he bonded the same mirror by five different adhesives. This amounted to a total of 25 specimens (5 barrels and 5 adhesives). The purpose of this set of measurements was to determine the most stable mirror and adhesive configuration out of these 25 specimens under vibration and shock. In the measurements, vibration PSD of 14 Grms and shock of 40g for 6 milliseconds were applied by two different shakers. The adhesives that were used were reported as Milbond, Masterbond-2LO (low outgas), Masterbond-2ND (non-dripping), OP-67-LS and ELC-1043. It was found that mirrors bonded with OP-67-LS, ELC-1043 and Masterbond-2ND had more angular movement than those bonded with Milbond and Masterbond-2LO. Masterbond-2LO is still frequently used at ASELSAN to bond lenses and mirrors in optomechanical systems, including those that are mounted on air platforms.

In 2016, Ke et al. [19] introduced an automatic optimization scheme in the Isight software. This optimization procedure used the inputs and outputs of the parametric CAD modelling software, ProE (or Creo as it is currently known), the finite element pre-and post-processing software Patran, the finite element analysis software Nastran and the optomechanical software Sigfit consecutively. Through this optimization process, the authors aimed to determine the support positions of a large-aperture mirror such that the root-mean-square (RMS) of optical surface error (deformation) was minimized after it was assembled with a gravitational load of 1g. They also aimed this optimization process to be automated and smart so that only one user input was required and that the transitions between software were carried automatically. They represented the support positions in terms of the inner and outer circle radii. The authors noted that each search step in their optimization method took only two minutes whereas it took an hour in their previous manual optimization method, hence, saving large amounts of time and manpower. The authors used advanced computer skills such as creating batch documents with .bat extension for each software and writing appropriate commands in text files with .txt extension so that each software automatically performed its task without opening the graphical user interface (GUI) when an input parameter file containing the parameters of the large-aperture mirror was supplied. After each search step, the authors only changed the few parameters in the input parameter file and re-ran the optimization process in Isight. In their example optimization process, the optimization is completed in 66 search steps, amounting to a total of about 2 hours (whereas each software manually required 1 hour for only 1 search step). Finally, Ke et al. note that this optimization process is designed to minimize the RMS surface error of a large-aperture mirror for a given topology. So, for a large-aperture mirror with different topology, another optimization process needs to be developed from scratch. It should be noted that this paper considers the effects of the residual static loading after an assembly process rather than vibrations. However, it was included in this literature survey to illustrate the state-of-art in utilizing the relationships between the CAD, finite element analysis, optimization and optomechanical software.

In 2017, Serief [20] determined the frequency of the micro-vibrations in arc-radian scale that affected the optical performance of the Alsat-1B satellite imager by conducting ground-based mechanical vibration tests. Then, by adopting the modulation transfer function (MTF) formulas in the existing literature for low frequencies [4], he plotted the MTF contribution of these micro-vibrations in two dimensions as a function of spatial frequency and spatial direction. Finally, by multiplying this MTF contribution with the static MTF provided by the telescope and imager, he obtained the overall MTF. Serief concluded that micro-vibrations restricted the MTF to lower values, thereby reducing the optical performance. He noted that this MTF estimate considered only the effects of micro-vibrations and did not include the any effect caused by the linear motion of the payload or platform. He considered these effects separately in his 2018 paper [24].

In 2018, McBride and Stratton [21] measured the image degradation in milli-arcseconds in the Daniel K. Inouye Solar Telescope due to vibration sources at 31 locations on four areas identified in and around the telescope. The inner areas are the telescope and enclosure foundations, and the outer areas are the utility building containing the large pumps and compressors and the outside areas, which include the cars that are driven on the roadway and parking lots. The telescope's total vibration budget is specified in arcseconds and was divided into 31 locations by scaling the total budget by the square root of 31. Path analysis is performed by direct measurement of the single-input single-output (SISO) frequency response function (FRF) between vibration source motions and image motion on the focal plane. The authors measured the FRF function on each of the 31 locations. The FRF functions were measured to determine the sensitivity of each location to a given force input. This enabled the authors to convert the allocated vibration budget in arcseconds for each location into an allowable amount of force in Newtons. They accomplished this by simply dividing the budget by the FRF value at a given frequency. The force is easier to physically measure by simply placing a load cell on the location. Hence, convenience is improved in vibration mitigation for the solar telescope.

In 2019, Pause [22] analyzed the effects of mechanical modification on the maximum stress due to shock and natural frequencies of an optical assembly. He used SolidWorks Simulation commercial finite element analysis (FEA) tools. He compared the results of the standard and ruggedized assemblies where the housing material was aluminum 6061-T6 in both cases. The term "ruggedized" referred to the case where Pause made the assembly lighter by minimizing the number of parts in the assembly by uniting some parts that were originally separate and changing the assembly method from pins to C-mount fixing at the end. In the shock analysis, he applied an input of 100g for 1 second along the optical axis, which he considered as moderate in his range of common values from 12g to 11000g. In the random vibration analysis, he applied an extreme PSD input of 10.94g rms in the frequency range of 0 – 1500 Hz. In his comparison, Pause noted that the ruggedized assembly had an improved ability to withstand shock and vibration because they could better absorb the forces of the applied shock and possessed higher natural frequencies owing to its reduced mass. For further research, Pause suggested further modifications to be made to the ruggedized system so that it can withstand the shock of 100g and the PSD spectrum of 10.94 g rms. He also suggested FEA comparison of the same mechanical design with different materials. Since this research considers the effects of vibration and shock on only structural integrity rather than optical performance, the applied shock and random vibration are viewed as extreme.

CHAPTER 3

FINITE ELEMENT ANALYSIS OF THE OPTOMECHANICAL SYSTEM

This chapter describes the optomechanical system to be analyzed in this thesis, its finite element model developed by commercial finite element analysis software. Specifications of this finite element model, and other operations that are performed to import the FEA results into the optomechanical analysis software are also discussed.

3.1 Description of the Optomechanical System

The optomechanical system that is analyzed in this thesis is the midwave infrared (MWIR) optomechanical assembly that is mounted on the platform of an aerial vehicle, similar to that considered by Doyle and Cerrati et al [15], excluding the gimbal. It allows the pilot of the vehicle to view their environment on the vehicle's monitor in the MWIR range, which is 3 to 5 micrometers. The infrared optics enable the pilot to perceive objects only by perceiving their temperature difference from the surroundings without requiring light. This allows easy and quick detection of the enemy airforces and incoming missiles by perceiving the heat from their exhausts. The optical and mechanical elements are assembled together by applying an adhesive. This adhesive covers the gap between the outer diameter of the lens and the inner diameter of the mechanical element. DC motors and electronic cards are used to move the optical assemblies and to control this motion. These motions allow the optomechanical system to work at different magnifications and fields of view. Wide field of view (WFOV) gives the largest angle of view with the lowest perception distance and narrow field of view (NFOV) gives the smallest angle of view with the highest perception distance.

The optomechanical system considered in this thesis consists of three stationary and three movable sub-assemblies, each of which has a different optical function. Ultimately, the rays are focused on the focal plane of the detector after they are refracted and reflected through all of these sub-assemblies. The sub-assemblies are held together by one large but lightweight mechanical bench part. These sub-assemblies include lenses and mirrors, which are referred to as "optical components" or "optical parts" in the rest of the thesis.

Moderately complex optomechanical systems are usually required to work in more than one field of view and are required to be adjustable to the correct field of view whenever needed. Each field of view means an optical design with different lens positions. Therefore, the lenses whose positions change should be attached to an optomechanical component that can be moved. The trajectory of motion is determined by the range of lens positions. The power required for this motion is provided by a high-precision DC motor and the control of this motion is provided by electronic cards. In the analysis and experimental studies for the thesis, all optical components are in the positions corresponding to the narrowest field of view, at which the effects of vibration can be seen most clearly.

From the outer world to the detector, the sub-assemblies can be listed as follows:

- The large lens (LL) that collects all of the thermal radiation from the observed environment and the optomechanical components that hold it in its fixed place (Figures 3.2, 3.3 and 3.9 in the following pages)
- The first movable zoom group (MZoG1), which contains Movable Zoom Lens 1 (MZL1) (Figure 3.4 in the following pages) and helps to change the field of view by zooming into or out of the image
- The second movable zoom group (MZoG2), which contains Movable Zoom Lens 2 (MZL2) and Movable Zoom Lens 3 (MZL3) (Figure 3.4 in the following pages) and also helps to change the field of view by zooming into or out of the image

26

- The stationary first folding mirror (M1) that deviates the angle of the light ray by 90 degrees (Figures 3.5 and 3.10 in the following pages)
- The movable focus group (MFoG), which contains Movable Focus Lens 1 (MFL1) and Movable Focus Lens 2 (MFL2) (Figures 3.6 and 3.11 in the following pages) and helps to obtain a focused image at a given field of view
- The stationary second folding mirror (M2) that again deviates the angle by 90 degrees and thus directs the light rays toward the detector (Figure 3.7 in the following pages)
- The converging lens (CL) that focuses the light rays on the detector (Figure 3.8 in the following pages)
- The detector, on which the image is formed
- The bench that holds all of the above optical sub-assemblies together

As their name implies, folding mirrors are used to prevent the optomechanical system from becoming too long in the optical axis by "folding" the axis by 90 degrees. Otherwise, it would be much more difficult to maintain the concentricity between the lenses and the optomechanics. Furthermore, folding mirrors are needed to maintain the system design within a constrained volume, which is usually given by the customer and other design departments, and can be changed only slightly if that is even possible. The rotation of 90 degrees is achieved by the phenomenon of reflection, where the light rays are reflected from the surface of the mirror with the same angle as the incidence angle. The mirror is placed at a 45-degree angle to the original optical axis to obtain the 90-degree reflection.

Refraction occurs as the rays pass through each lens. As they move from the air into the lens material and from the material back into the air, their angle of incidence changes due to Snell's law. Every medium change causes the angle to change and also loss of some radiation energy. In order to minimize this loss, both surfaces of each lens are coated with a thin film according to a prescription designed by the thin film design engineers. Finally, the detector, on which all the rays eventually focus to form the image, works in the midwave infrared range (3 to 5 micrometers).

Other auxiliary components that help the rays to proceed through the optical layout include:

- DC motors
- Pinion gears at the ends of DC motor shafts
- Electronic cards for driving and controlling the position of the DC motors
- Pins attached to the barrels of the movable groups

Figures 3.1 through 3.11 show the block diagram of the optomechanical system considered in the thesis and the interface details and CAD models of the optical sub-assemblies. In Figure 3.1, some parts of the model are simplified due to confidentiality.
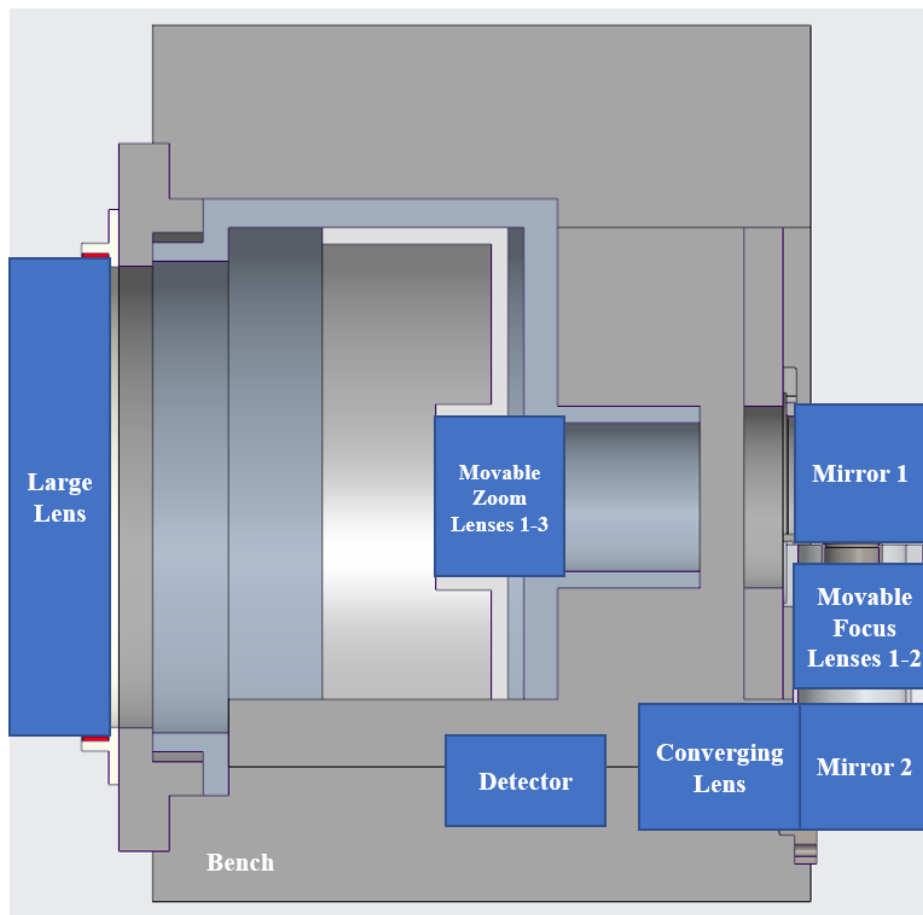
Figure 3.1. Block diagram of the optomechanical system considered in the thesis
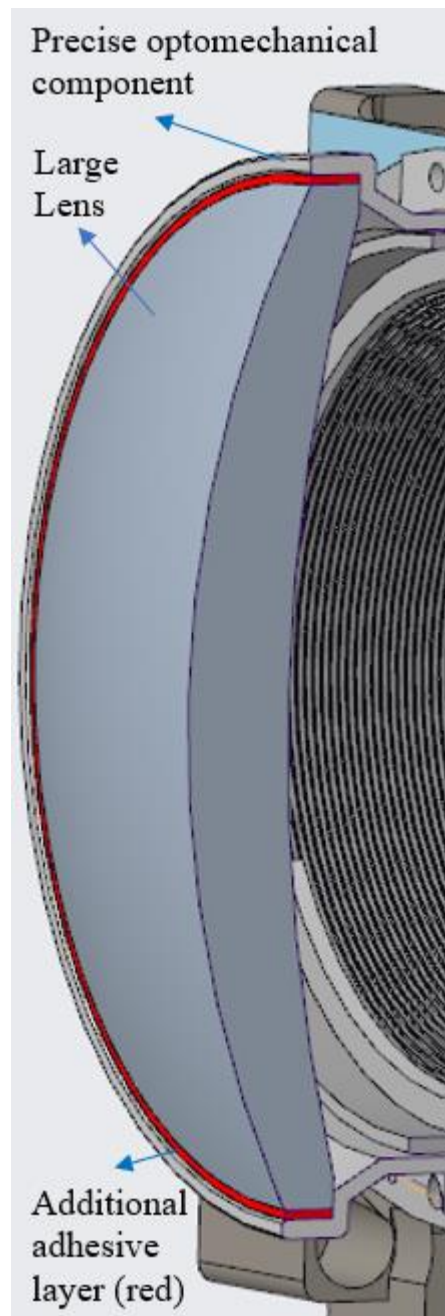
Figure 3.2. Interface details of the large lens
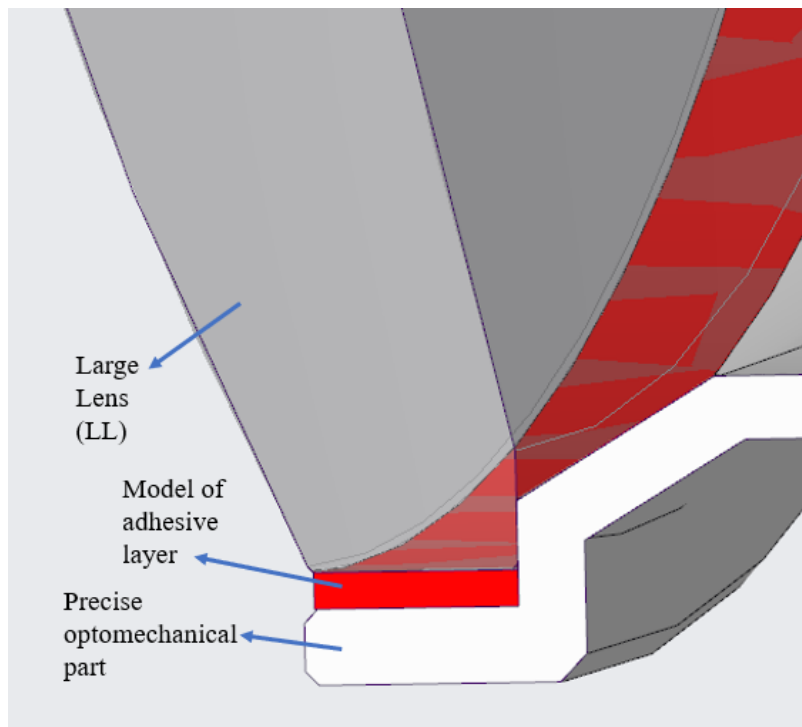
Figure 3.3. Interface details of the large lens (close-up)
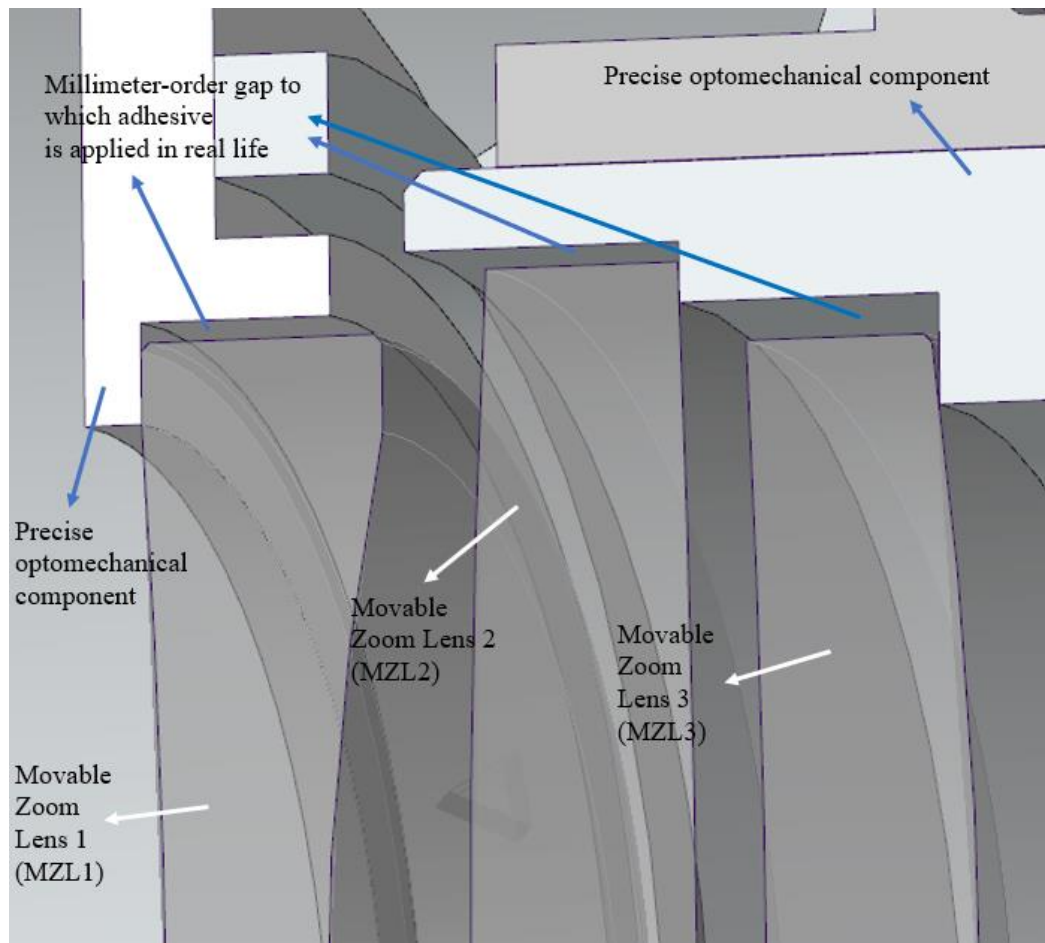
Figure 3.4. Interface details of the movable zoom groups
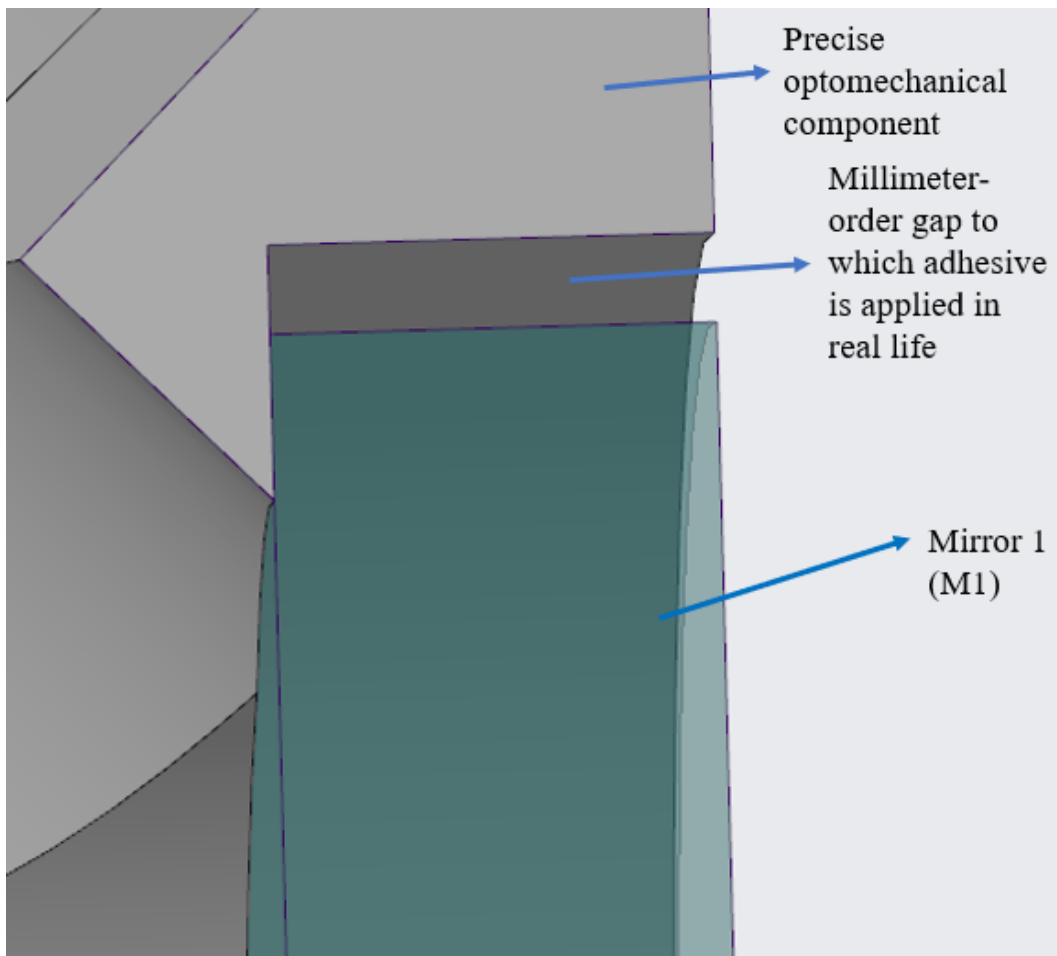
Figure 3.5. Interface details of Mirror 1
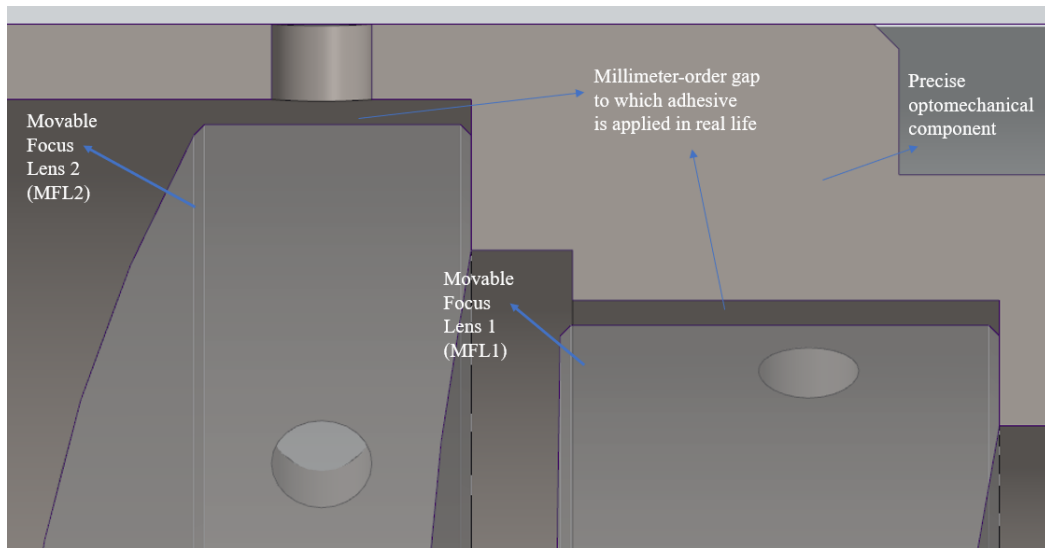
Figure 3.6. Interface details of the movable focus group
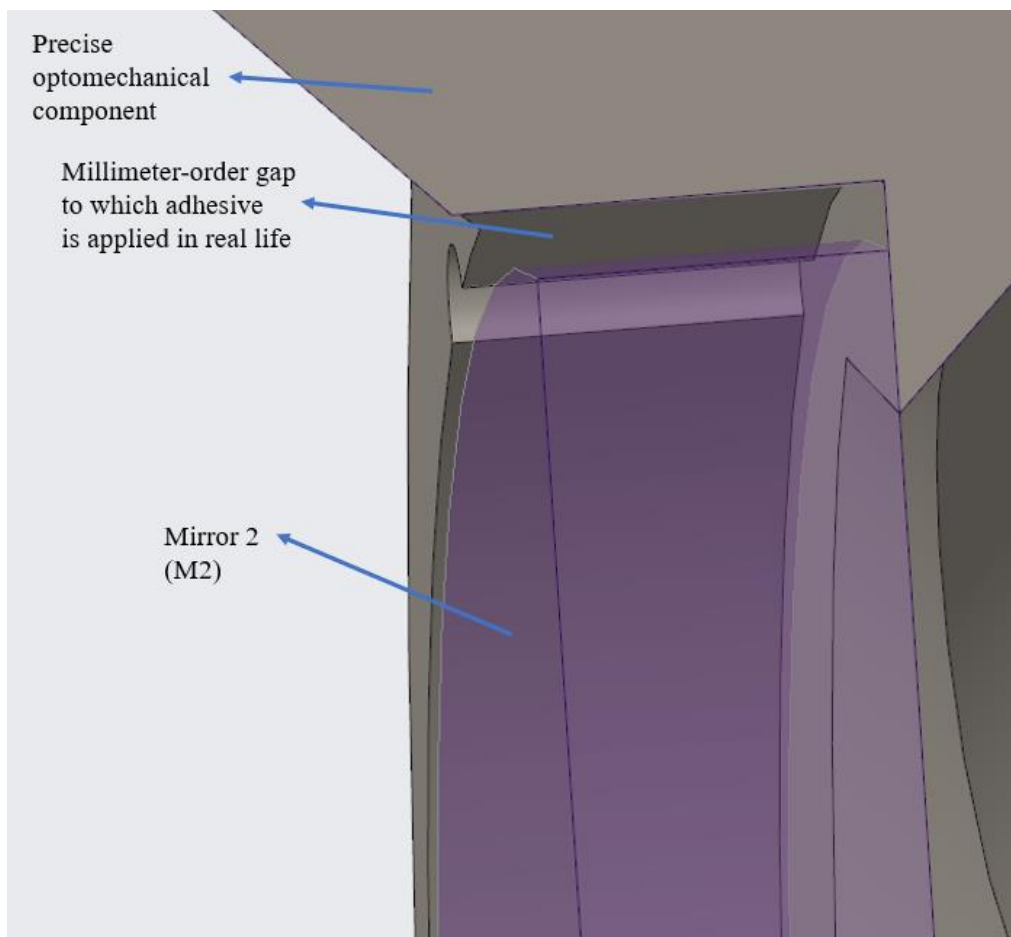
Figure 3.7. Interface details of Mirror 2
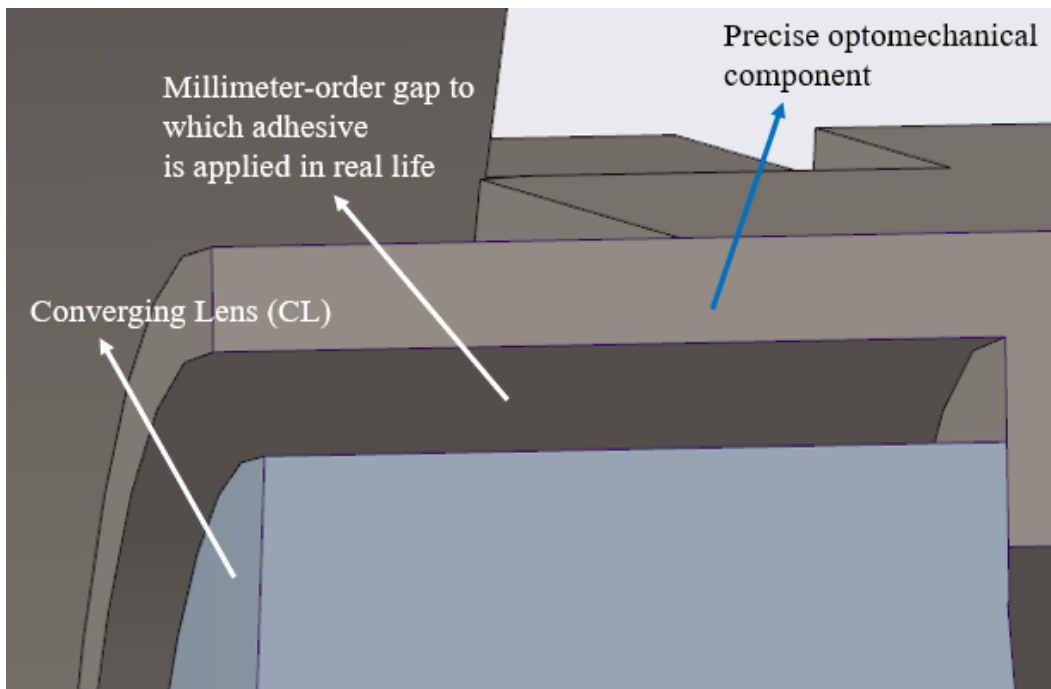
Figure 3.8. Interface details of the converging lens

Figure 3.9. CAD model of the front lens and its holder
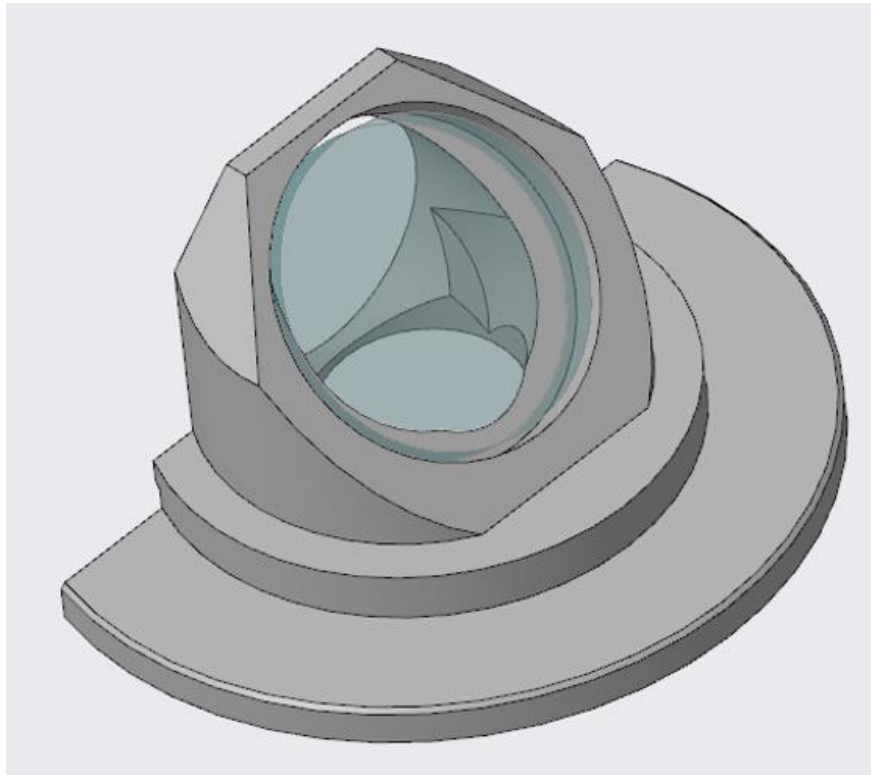
Figure 3.10. CAD model of Mirror 1 and its holder
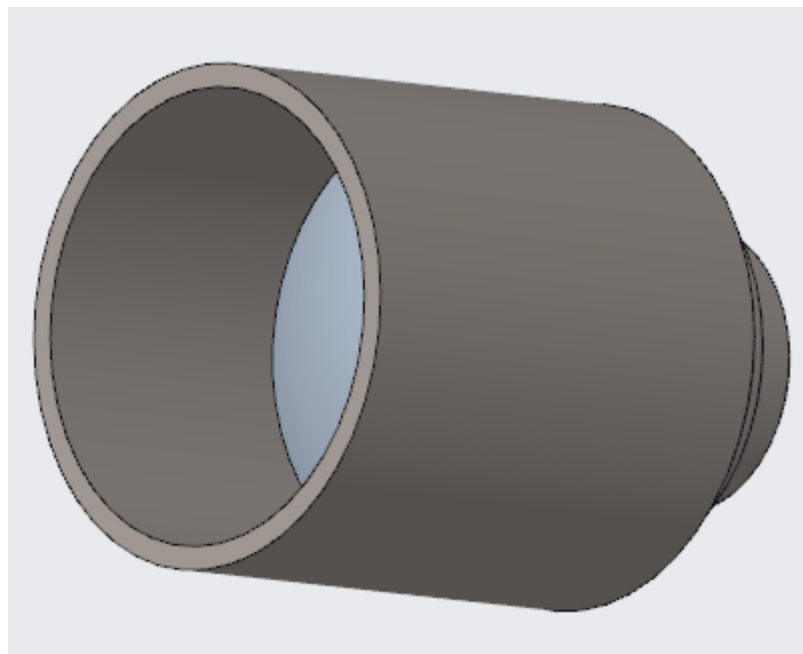
Figure 3.11. CAD model of the movable focus group and its holder (CAD models
of the movable zoom groups are also similar)

Inevitably, there are variations in the external environment where the system is used. During the system design, these variations should also be considered carefully. As outlined by Pause in his paper [22], they can be listed as follows:

- Variations in the ambient temperature
- Changes in the ambient atmospheric pressure
- Changes in the operational moisture
- Changes in the dynamic excitations during operation

In military applications, an optomechanical system is usually required to work within a wide temperature range typically from minus 40 degree to plus 70 degree Celsius because missions are possible anywhere on Earth. Toward both ends of this spectrum, especially the metal optomechanical components may contract or expand. For the stationary sub-assemblies, this contraction or expansion may create additional stress on the lenses. For the movable sub-assemblies, this is even more dangerous as it may cause the parts that move together to become stuck and effectively cause failure in operation. Changes in atmospheric pressure and moisture have similar effects. As the first three changes are not within the scope of this thesis, they are not discussed in further detail.

Dynamic excitations, the last item in this list, are inseparable components of environmental conditions. They occur in the form of harmonic or random excitation as well as shock, and they occur during most of the life-time of the optomechanical system, including its transport to the customer. However, transport excitations are not in the scope of this thesis. Excitations that occur during the operation after the system is mounted on the air platform are of major concern in this thesis. However, depending on their amplitudes, operational excitations can be classified into two types. The first type of operational excitations is those that have just sufficient energy to produce concern for optical performance. They are usually in the form of random excitations, or random and sinusoidal excitations combined, with the sinusoidal component coming from the engine/power plant of the air vehicle on which the system is mounted. For this type, the system is still required to function with a reasonable optical performance by implementing the necessary design efforts. The

36

second type of operational excitations is those with such a high amplitude that optical performance is out of the question. This type is usually in the form of shock from sudden dropping. In this case, the system is required to maintain only its integrity, i.e. survive, and there is no requirement for optical performance. The second type is related to the structural mechanics and strength of the system as a whole and it is not in the scope of this thesis. So, this thesis considers the first type of operational excitations and its effects on the optical performance.

While a commercial finite element analysis software like ANSYS is sufficient to determine the dynamic response parameters of the optomechanical system like natural frequencies, frequency response functions to harmonic excitation, and displacement under random PSD excitation, another software is needed to predict the effects on optical performance parameters. As mentioned previously, these parameters include line-of-sight error and MTF reduction.

3.2   Description of the Finite Element Model

For the finite element analysis, the 2021 R1 version of ANSYS Workbench was used. Before the CAD model of the design was imported into ANSYS, some manipulations or simplifications had to be applied to reduce the computation time. First, the bench part that held the sub-assemblies together was simplified extensively by erasing the fillets or thin ledges that could cause meshing failure. The optomechanical parts in the sub-assemblies were also simplified as needed. The thin parts that did not have a significant effect on the stiffness of the system were deleted. The models of the motors, electronic cards and cooling fans around the optomechanical system were also overlooked. The parts that were neglected in the CAD model were added as Point Masses in the Geometry section of the model. These point masses were placed in their centers of gravity. The masses and centers of gravity were calculated by using the CAD software, and the corresponding coordinate systems were added in ANSYS. The adhesive interfaces between the optical and optomechanical parts were modelled as bonded contacts with the

appropriate pinball radius regions that were input manually. All other contacts were also bonded.

In the finite element model, it was assumed that the dynamic properties of the adhesives or the movable optical groups on their own did not have any significant effect on the natural frequencies of the optomechanical system and that the optical and optomechanical components were firmly attached together without any relative motion caused by the adhesives. These assumptions were verified by performing separate finite element analyses of the movable optomechanical groups with appropriate fixed supports with and without adhesive, where it was found that none of the groups had a vibration mode lower than 300 Hz (one tenth of 1.5 times the highest frequency of interest, the 1.5 factor being conservative) and that no relative motion was observed between the optical part and the adhesive. Furthermore, since the effects of vibration on optical performance were observed most clearly in the narrow field of view, the movable optical groups were assumed to be stationary in the position that gave the narrow field of view. The DC motor was assumed to apply sufficient torque to maintain the lenses in their position with respect to their weights. This assumption was also verified through real-life assemblies.

The micrometer order-of-magnitude radial gap between the movable optical groups and the optomechanical barrels in which they were assembled was also considered. In order to take this gap into account, the bonded contact was not defined directly between the mating diameters, but instead it was defined between the surfaces of the slot and the pins. The pins were modelled as integral protrusions of the optomechanical parts containing the movable optical groups. In total, four of such bonded contacts were modelled in the Connections section of the finite element model; two from the first and two from the second movable zoom group. Figures 3.12 and 3.13 show the definitions of two of these Bonded contacts.

38
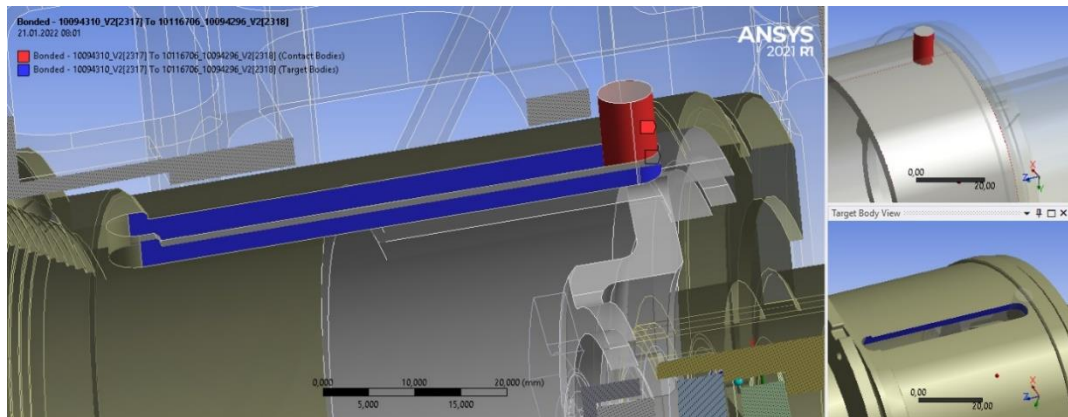
Figure 3.12. Definition of the bonded contact between the surfaces of the pin and the slot for the first movable zoom group
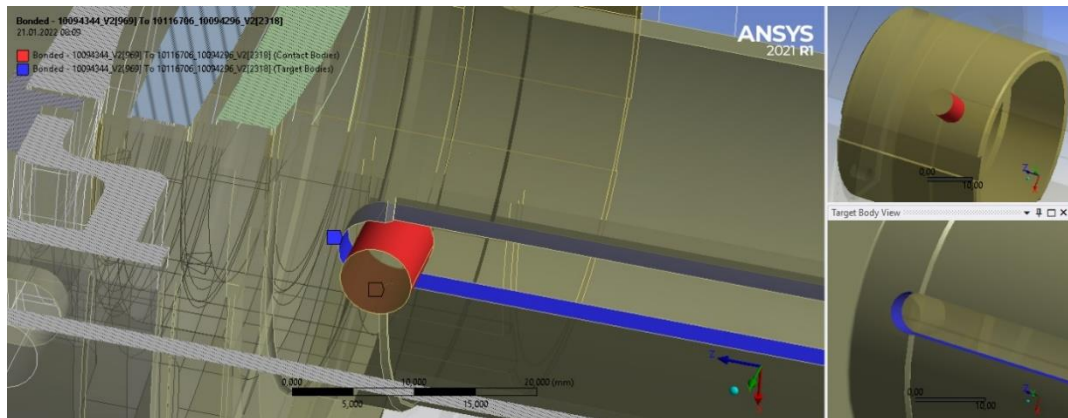
Figure 3.13. Definition of the bonded contact between the surfaces of the pin and the slot for the second movable zoom group

The global coordinate system of the entire optomechanical system in general was such that the x-axis was the direction along which the system was the thinnest and except for few optical parts, the z-axis corresponded to the line-of-sight. The y-axis was perpendicular to the x-axis, and both were parallel to the focal plane array of the sensor at the end of the optical path. Furthermore, coordinate systems were also added to the vertex points of each optical component so that the optomechanical analysis software that would be used to predict the optical performance could recognize them. The vertex point is the point on the lens surface that intersects with the light ray passing exactly on the optical axis. Here, it was crucial that the origins

and axis directions of the coordinate systems in the finite element model aligned with those in the raw model that was imported from the optical design software by the optical design engineer. Each of these coordinate systems was manually identified in the Details section by inputting a number greater than 11, starting with 12 in the coordinate system on the vertex of the first optical surface and continuing with 13, 14, and so on. The numerical order of the coordinate systems determined the order in which the ray would pass through the optical components. An example of the definition of a coordinate system placed on the optical surface is shown in Figure 3.14. The "Coordinate System" entry was changed manually from "Program Controlled" to "Manual" by the user, which enabled the user to enter the "Coordinate System ID" manually. ANSYS automatically defined the coordinate system ID as 12, which was then changed by the user.

Definition	
Type	Cartesian
Coordinate System	Manual
Coordinate System ID	14,
APDL Name	
Suppressed	No
Origin	
Define By	Global Coordinates
Origin X	6,7314e-015 mm
Origin Y	1,827e-014 mm
Origin Z	-124,35 mm
Location	Click to Change
Principal Axis	
Axis	X
Define By	Fixed Vector
Orientation About Principal Axis	
Axis	Y

Details   Section Planes
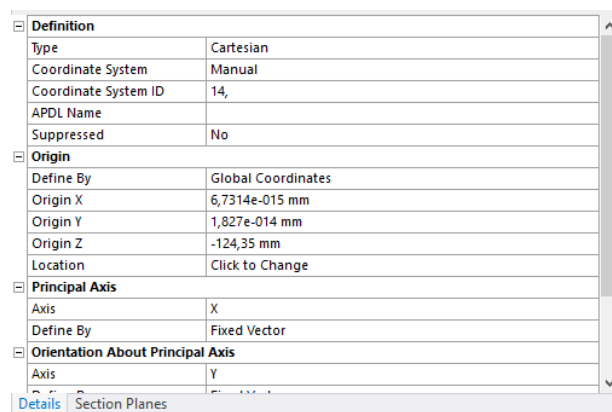
Figure 3.14. Definition of a coordinate system placed at the vertex of an optical surface

A mesh size of 5 mm for all parts was used with the exception of 2 mm mesh size for the optical parts in order to predict their deformations under random excitation more accurately. Figure 3.15 shows a view of the meshes in the finite element model. There was a total of 795183 nodes and 490300 elements in the model. The average mesh quality was 0.74 with a standard deviation of 0.24.
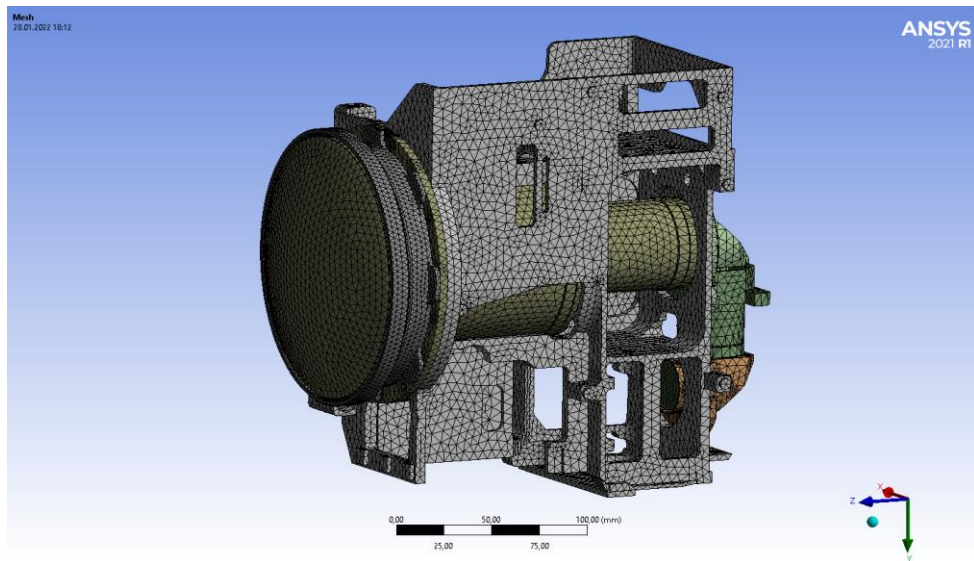
Figure 3.15. View of the meshes in the finite element model

The schematic of the performed finite element analyses on ANSYS Workbench is presented in Figure 3.16. As the schematic implies, first Modal Analysis is performed. Then, both the Harmonic Response and Random Vibration analyses are based on the results of this Modal Analysis.
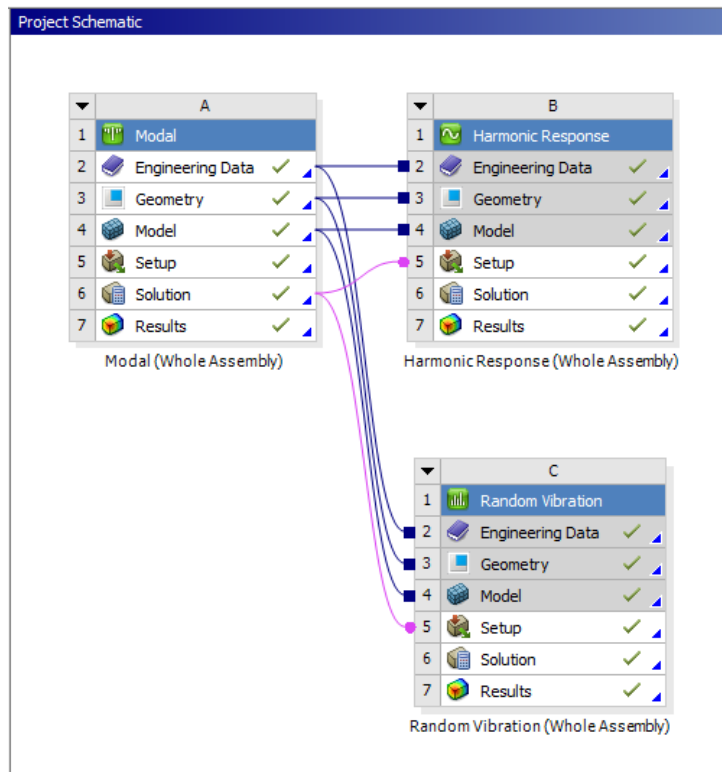
Figure 3.16. Schematic of the performed finite element analyses on ANSYS Workbench

3.3 Modal Finite Element Analysis

The first analysis that was performed in ANSYS was the modal analysis. However, before performing the modal analysis of the whole optomechanical system, the rigidity of its movable zoom groups and adhesives needed to be determined. For this purpose, finite element analyses of the movable zoom groups with and without adhesive were performed. These analyses are described in Sections 3.3.1 and 3.3.2. Then, the modal analysis of the optomechanical system according to the results of these analyses is described in Section 3.3.3.

3.3.1 Modal Analysis of the First Movable Zoom Group

Modal analysis was conducted for the first movable zoom group with and without adhesive to determine if the adhesive had its own effects on the dynamic properties of the optomechanical system in the frequency range of interest (10 to 2000 Hz). It was also aimed to determine if the first movable zoom group had its own structural natural frequencies. Frequencies below 300 Hz (one-tenth of 1.5 times the highest frequency of interest, the 1.5 factor being conservative) would be considered significant. Such a consideration was made because the first movable group was attached to the larger optomechanical part through a pin and slot where the pin was modelled as an integral protrusion of the part to reduce the number of contact definitions and so computation time. For the first movable zoom group, the x and y axes are both parallel to the optical part. The z-axis acts as the optical axis and it is normal to the optical part. Figures 3.8 and 3.9 show the directions of these axes together with the first mode shape of the first movable zoom group without and with adhesive, respectively.

In the case with adhesive, the adhesive was modelled as a solid circular part that covered the entire clearance between the outer diameter of the optical part and the inner diameter of the optomechanical part. Two bonded contacts were defined; one for the contact with inner diameter and other for the contact with outer diameter. Thus, the adhesive acted as a bridge between the optical and optomechanical parts, and its material properties were also considered in the analysis. To be able to include the effect of the adhesive accurately, the mesh size was adjusted to its dimensions. A face sizing of 1.2 mm was applied to the surfaces of the inner and outer diameters and a face sizing of 0.12 mm was applied to both sides, which corresponded to 3 meshes along tangential thickness and 8 meshes along radial thickness of the adhesive. Figure 3.17 shows the meshing of the adhesive in the cross-section. It was assumed that the adhesive acted like an elastic material similar to aluminum and other materials and so it had a constant modulus of elasticity. However, in reality, adhesives are viscoelastic materials whose moduli of elasticity change significantly with the frequency and temperature as well as geometry. To be able to determine the

stiffness and damping coefficient of an adhesive as a viscoelastic material, many tests and experiments have to be conducted, which was the topic of Avşar's thesis [17] for another adhesive that could not be used in this optomechanical system due to design constraints. Then again, experience has shown that it is reasonable to assume the adhesive to be an elastic material since it acts like one when it is applied around the optical parts in relatively low, millimeter-order thickness in vibration environment tests. The value calculated in Avşar's thesis for the adhesive was around 2 MPa. This was also considered as the Young's modulus of the adhesive in this thesis to get a conservative estimate of the adhesive's elasticity.

For the optical parts, the same mesh size (2 mm) was applied as in the mesh of the whole optomechanical system. Table 3.1 shows the compared material properties of the adhesive, aluminum and germanium as defined in ANSYS. Aluminum is the material of most of the optomechanical components and germanium is the material of the movable optical components in the system. Since this system works in the IR wavelength range, germanium is a preferable optical material.
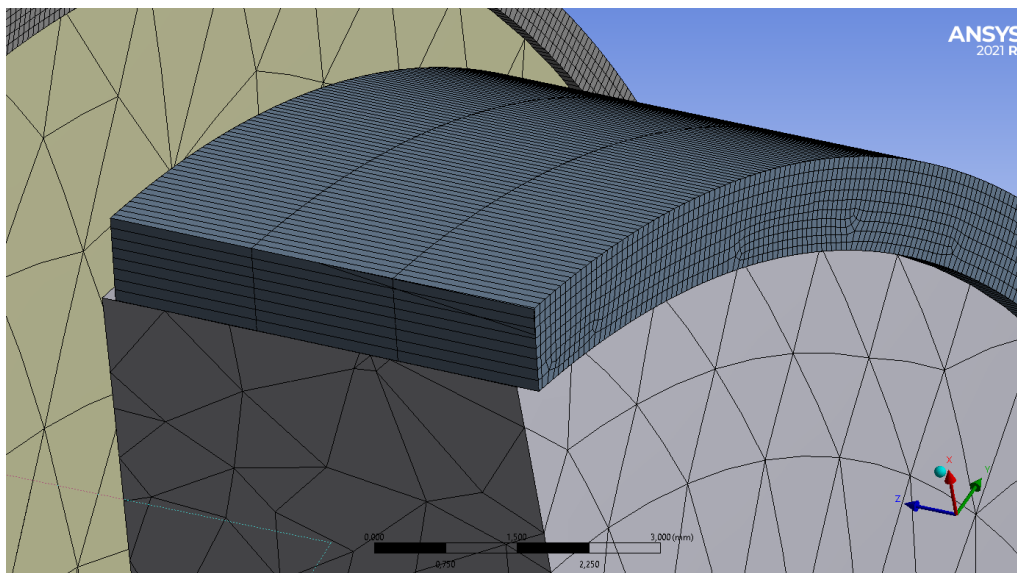
Figure 3.17. Meshing of the adhesive model around the optical part

Table 3.1. Material Properties of the Adhesive, Aluminum and Germanium as defined in ANSYS

Material Property	Adhesive	Aluminum	Germanium
Young's Modulus, E	2 MPa	68900 MPa	130000 MPa
Density, ρ	1500 kg/m^3	2700 kg/m^3	5323 kg/m^3
Poisson Ratio, υ	0.45	0.33	0.3

In the case without adhesive, bonded contact with appropriate pinball radius was defined between the outer diameter of the optical part and the inner diameter of the optomechanical part while keeping the millimeter order-of-magnitude radial space between these diameters empty. Thus, the same degrees of freedom of the optical part were constrained as in the case with adhesive without significant loss of accuracy since the inclusion of the adhesive did not cause any relative motion as indicated by the following Table 3.3 and Figure 3.20.

In both cases (with and without adhesive), only bonded contacts were used; and the fixed supports were selected as the top surfaces of the pin protrusions. The top surfaces of the pin protrusions being fixed represented how the pins were constrained in the general optomechanical system. In the system, five of the six degrees of freedom of the pin were constrained. The pin was only free to translate along the optical axis (z-direction).

Sectional views of the first movable zoom group with and without adhesive are shown in Figure 3.18.
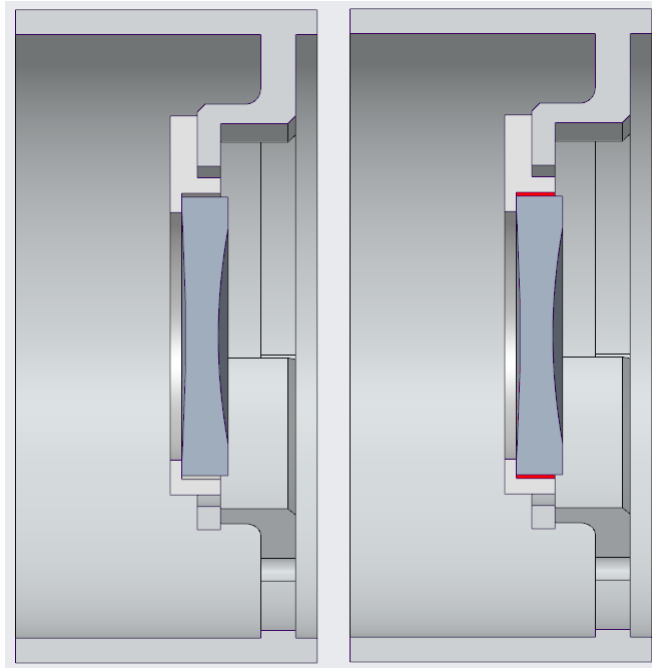
Figure 3.18. Sectional views of the first movable zoom group with (right) and without (left) adhesive

For the first movable zoom group without adhesive, the first 20 natural frequencies were found as listed in Table 3.2.

Table 3.2. First 20 natural frequencies of the first movable zoom group without adhesive

	Mode	☑ Frequency [Hz]
1	1,	380,74
2	2,	1238,7
3	3,	2217,6
4	4,	2387,4
5	5,	2489,1
6	6,	3172,5
7	7,	3404,7
8	8,	3904,9
9	9,	4235,6
10	10,	4506,7
11	11,	4662,6
12	12,	5750,9
13	13,	5805,
14	14,	6203,5
15	15,	6326,5
16	16,	7614,5
17	17,	7729,6
18	18,	8061,5
19	19,	8205,5
20	20,	8965,5

As implied by the results, there were no structural modes below 300 Hertz. So, the first movable zoom group could be assumed as rigid and there was no need to consider its elasticity separately. Figure 3.19 shows the first mode shape of the first movable group without adhesive at 381 Hz. Here, the first movable zoom group has a bending structural mode about the axis formed by the two pins on the xy-plane while the pins around the fixed support do not move at all.
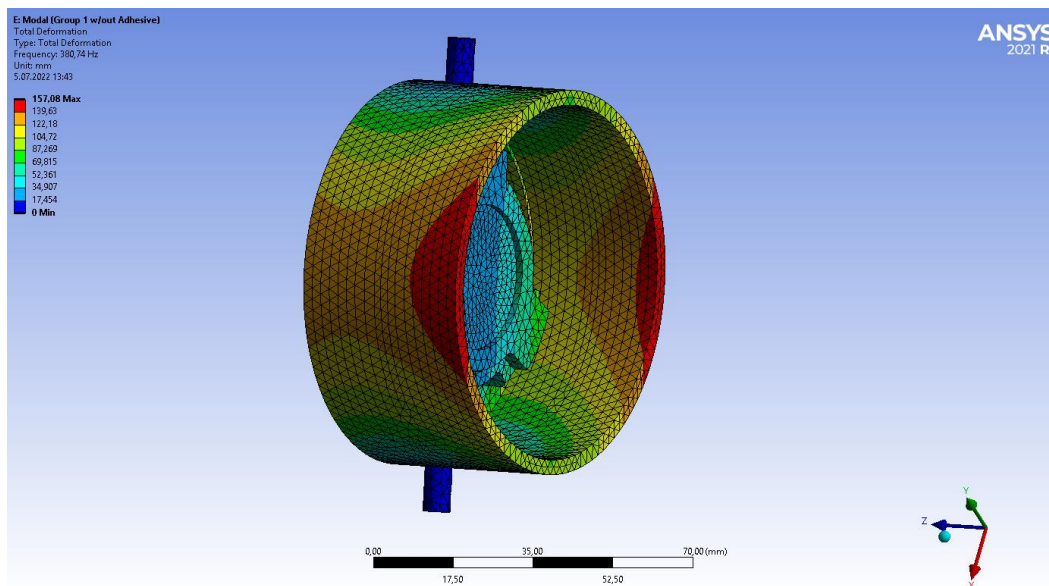
Figure 3.19. First mode shape of the first movable zoom group without adhesive at 381 Hz

For the first movable zoom group with adhesive, the first 20 natural frequencies were found as listed in Table 3.3.

Table 3.3. First 20 natural frequencies of the first movable zoom group with adhesive

	Mode	☑ Frequency [Hz]
1	1,	380,5
2	2,	1237,1
3	3,	2217,4
4	4,	2383,7
5	5,	2484,7
6	6,	3171,6
7	7,	3400,5
8	8,	3896,
9	9,	4228,7
10	10,	4505,5
11	11,	4659,6
12	12,	5748,
13	13,	5795,9
14	14,	6193,5
15	15,	6317,7
16	16,	7594,6
17	17,	7699,3
18	18,	8058,8
19	19,	8195,2
20	20,	8963,2

There was very little difference between the cases with and without the adhesive. There did not appear to be any differences between the mode shapes either, implying that the adhesive did not have any significant elastic mode on its own in the first movable zoom group. None of the mode shapes indicated relative motion of the optical part with respect to the adhesive due to adhesive's elasticity. Hence the adhesive could be assumed as rigid and so it did not need to be included in the dynamic analysis. Figure 3.20 shows the first mode shape of the first movable zoom group with adhesive at 380.5 Hertz. Here, the optomechanical assembly again has a bending structural mode about the axis formed by the pins on the xy plane, giving the same mode shape as the case without adhesive.
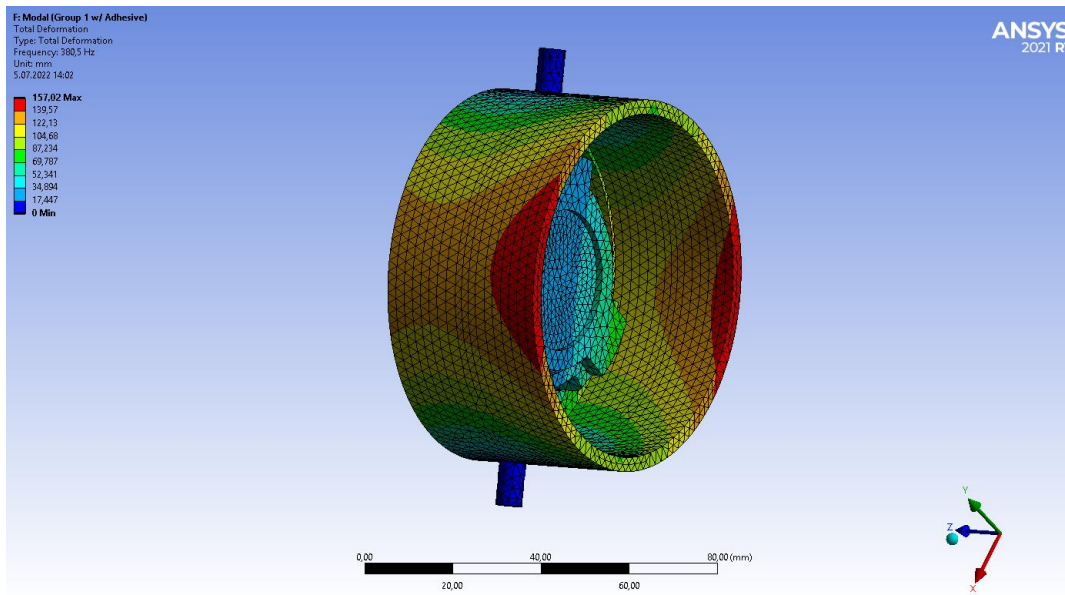
Figure 3.20. First mode shape of the first movable group with adhesive, also at 381 Hz

3.3.2. Modal Analysis of the Second Movable Zoom Group

Modal analysis was also conducted for the second movable zoom group with and without adhesive to determine if the adhesive had its own effects on the dynamic properties of the optomechanical system in the frequency range of interest (10 to 2000 Hz). With respect to the first movable zoom group, only the optical and optomechanical parts were different. The contacts described in Section 3.3.1 were used for the cases with and without adhesive for the second movable zoom group as well.

For the second movable zoom group without adhesive, the first 20 natural frequencies were found as listed in Table 3.4.

50

Table 3.4. First 20 natural frequencies of the second movable zoom group without adhesive

	Mode	✔ Frequency [Hz]
1	1,	883,76
2	2,	4648,
3	3,	5548,8
4	4,	6303,7
5	5,	6692,4
6	6,	7741,4
7	7,	12294
8	8,	17206
9	9,	17467
10	10,	22196
11	11,	24920
12	12,	27690
13	13,	27966
14	14,	28431
15	15,	29308
16	16,	31634
17	17,	31902
18	18,	33176
19	19,	33306
20	20,	33331

As implied by the results, there were no structural modes below 200 Hertz. So, the second movable zoom group could be assumed as rigid and there was no need to consider its elasticity separately. Figure 3.21 shows the first mode shape of the second movable zoom group without adhesive at 883 Hz. As shown in Figure 3.21, the second movable group has a bending structural mode about the axis formed by the two pins parallel to the y-axis, which is the same as in the mode shapes found for the first movable group with and without adhesive (Figures 3.8 and 3.9).
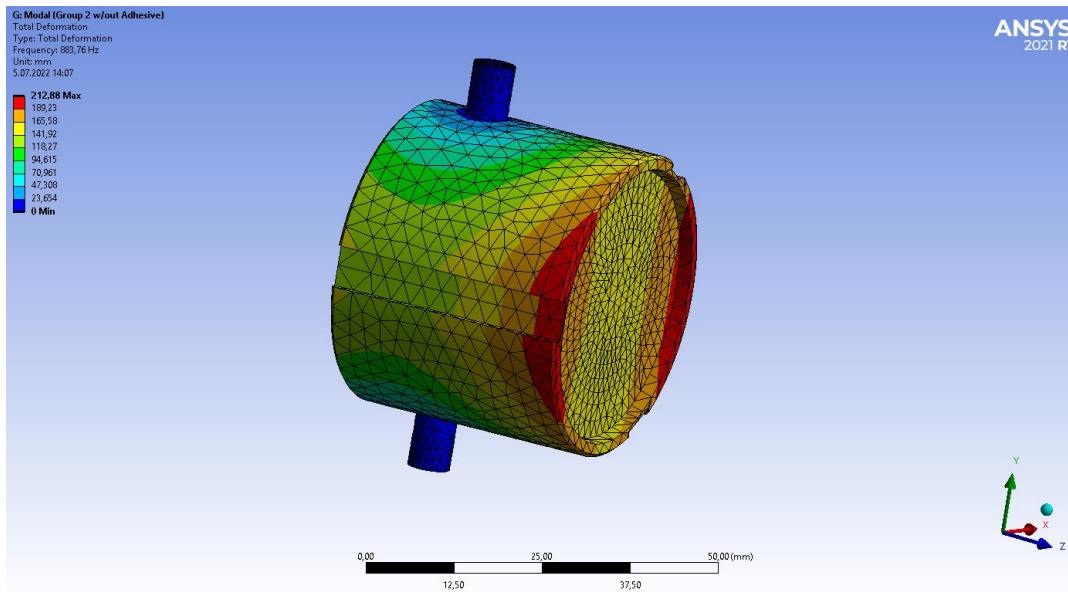
Figure 3.21. First mode shape of the second movable zoom group without
adhesive at 883 Hz

The first 20 natural frequencies and mode shapes of the second movable
group with adhesive were found as listed in Table 3.5.

Table 3.5. First 20 natural frequencies and mode shapes of the second movable zoom group with adhesive

	Mode	✓ Frequency [Hz]
1	1,	878,59
2	2,	4582,3
3	3,	5454,6
4	4,	6242,6
5	5,	6576,1
6	6,	7641,2
7	7,	8966,5
8	8,	8970,
9	9,	9174,8
10	10,	9176,8
11	11,	9196,7
12	12,	9217,8
13	13,	9247,1
14	14,	9265,2
15	15,	9292,2
16	16,	9292,4
17	17,	9296,1
18	18,	9324,6
19	19,	9329,6
20	20,	9335,6

Table 3.5 (cont'd)		
Mode Number	**Frequency (Hz)**	**Category**
1	878.59	Bending structural mode of the movable group (except pins) about the y-axis (parallel to the pins' axis) with no motion on the pins around the fixed supports
2	4582.3	Structural mode as axial vibration of the movable group along the z-axis and the resulting bending of the pins about the x-

		axis around the fixed supports
Table 3.5 (cont'd)		
3	5454.6	Bending structural mode of both the movable group and the pins about the x-axis around the fixed supports
4	6242.6	Structural mode as bending of the movable group about the y-axis and bending of the pins about the z-axis around the fixed supports
5	6576.1	Structural mode as torsion of the movable group about the z-axis and the resulting bending of the pins about the z-axis around the fixed supports
6	7641.2	Structural mode as bending of the movable group and the pins about the x-axis around the fixed supports with additional elastic deformation around the surface of the housing away from the lenses

Table 3.5 (cont'd)		
7	8966.5	Elastic mode of the adhesive part around the optical part in the back as contraction and expansion at a specific point with no motion of any other part
8	8970	Similar to Mode 7
9	9174.8	Elastic mode of the adhesive part around the optical part in the back as contraction and expansion at a specific point close (but not same as) Modes 7 and 8 with no motion of any other part
10	9176.8	Similar to Mode 9
11	9196.7	Elastic mode of the adhesive part around the optical part in the back as contraction and expansion at a specific point opposite to that in Modes 7 and 8 with no motion of any other part
12	9217.8	Similar to Mode 11
13	9247.1	Elastic mode of the adhesive part around the

		optical part in the back at another specific point
Table 3.5 (cont'd)		
14	9265.2	Similar to Mode 13
15	9292.2	Elastic mode of the adhesive part around the optical part in the back at another specific point
16	9292.4	Similar to Modes 13 and 14
17	9296.1	Similar to Mode 15
18	9324.6	Similar to Mode 16
19	9329.6	Similar to Mode 10
20	9335.6	Similar to Mode 19

As described in Table 3.5, out of the first 20 modes, the first 6 modes were the structural modes of the second movable zoom group and their frequencies were close to those of the case without adhesive. So, there were no structural natural frequencies below 200 Hertz. However, modes 7 through 20 were all elastic modes of the adhesive that was used to bond the back lens of the second movable zoom group. Their frequencies were relatively close to each other and in the range of 8950 Hertz to 9350 Hertz. Since these frequencies were out of the frequency range of interest (10 to 2000 Hz) for this thesis, it was again concluded that the adhesive could be assumed as rigid and that it did not need to be modelled separately. Furthermore, none of the mode shapes indicated relative motion of the optical part with respect to the adhesive due to adhesive's elasticity. As shown in Figure 3.22, the first structural mode of the second movable zoom group with adhesive had the same mode shape as the case without adhesive (rotation about the axis formed by the two pins, parallel to the y-axis). Figure 3.23 shows the first elastic mode of the adhesive on its own, which

corresponded to the seventh mode shape of the second movable group in general. All modes numbered between 7 and 20 were in this fashion.
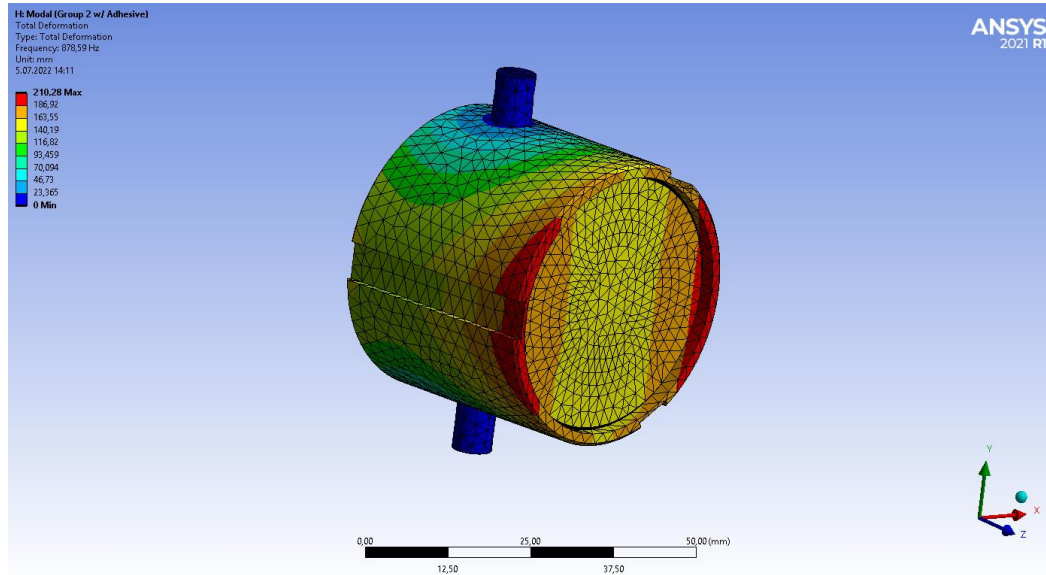
Figure 3.22. First mode shape of the second movable zoom group with adhesive at 879 Hz
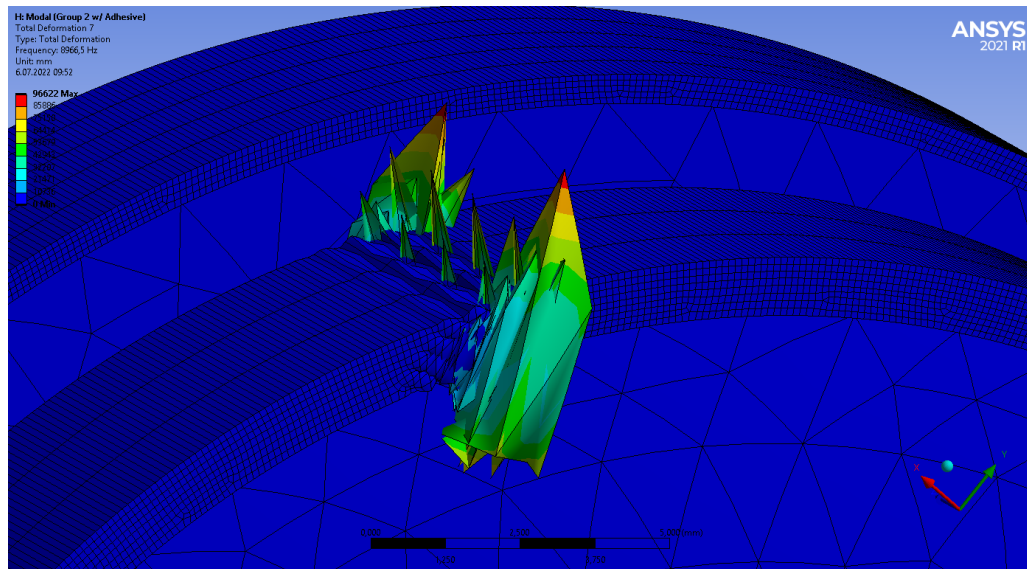
Figure 3.23. First elastic mode shape of the adhesive part in the second movable zoom group on its own

From the results of the above analyses in Sections 3.3.1 and 3.3.2, two conclusions were reached. The first conclusion was that the two movable zoom groups did not need to be analyzed separately since none of them associated with a natural frequency below 300 Hz and so they could be assumed as rigid. The second conclusion was that the adhesive could also be assumed as rigid and so it did not need to be included in the dynamic analysis because it did not cause relative motion of the optical part and its own elastic natural frequencies were far beyond the frequency range of interest. Thus, all optical parts in the system were modelled such that they were directly bonded to the optomechanical parts that held them while keeping the radial space between them empty, which is normally filled with the adhesive in the real-life physical system. As indicated by the results in Tables 3.3 and 3.5, the adhesive did not cause any additional relative motion within the frequency range of interest, and so there would not be a significant loss of accuracy compared to the case where the adhesive was included. The modal analysis of the whole optomechanical system was performed according to these assumptions. The results of this analysis are presented in the following Section 3.3.3.

3.3.3 Modal Analysis of the Whole Optomechanical System with Only Pinball Region Bonded Contacts

For the modal analysis of the whole optomechanical system, the contacts were applied according to the assumptions verified in Sections 3.3.1 and 3.3.2. The interfaces in all optical sub-assemblies were modelled as bonded contacts with pinball regions. The model was fixed at the holes that would normally be used to fix the system onto the testing table in real life use. The first 20 natural frequencies of the system with this boundary condition were found as shown in Table 3.6.

Table 3.6. First 20 natural frequencies and mode shapes of the optomechanical
system

	Mode	✔ Frequency [Hz]
1	1,	643,46
2	2,	860,78
3	3,	935,62
4	4,	1009,2
5	5,	1029,1
6	6,	1145,1
7	7,	1257,
8	8,	1275,3
9	9,	1353,1
10	10,	1490,5
11	11,	1528,9
12	12,	1591,8
13	13,	1610,6
14	14,	1647,
15	15,	1655,
16	16,	1761,7
17	17,	1782,4
18	18,	1870,2
19	19,	1991,
20	20,	2043,7

Table 3.6 (cont'd)		
Mode Number	**Frequency (Hz)**	**Category**
1	643.46	Bending structural mode of the bench around z-axis
2	860.78	Bending structural mode of the bench around x-axis
3	935.62	Bending structural mode of the bench around x-axis
4	1009.2	Combined bending structural mode of the bench around x and y axes

Table 3.6 (cont'd)		
5	1029.1	Bending structural mode of the first movable zoom group around y-axis
6	1145.1	Structural mode of the bench as axial vibration along z-axis (exhibited by one of the thin walls)
7	1257	Structural mode of the bench as axial vibration along z-axis (exhibited by another thin wall)
8	1275.3	Structural mode of the bench as axial vibration along z-axis (similar to Mode 7)
9	1353.1	Bending structural mode of the bench around x-axis with notable movement of both movable zoom groups and Mirror 2
10	1490.5	Bending structural mode of the first movable zoom group, Mirror 1, the movable focus group and Mirror 2 around the x-axis, and bending structural mode of the second movable zoom group around the y-axis (motion of the first movable group is more dominant)
11	1528.9	Bending structural mode of the first and second movable zoom groups and the movable focus group around the x-axis (motion of the first movable group is slightly more dominant)
12	1591.8	Bending structural mode of the first zoom group and movable focus group around the x-axis and bending structural mode of the second zoom group around the y-axis (motion of the first zoom group is more dominant)
13	1610.6	Bending structural mode of the first zoom group and movable focus group around the x-axis

		(motion of the movable focus group is more dominant)
Table 3.6 (cont'd)		
14	1647	Structural mode of the bench as axial vibration along the x-axis (one of the thin walls) and bending structural mode of movable focus group around the x-axis (motion of the bench is more dominant)
15	1655	Structural mode of the bench as axial vibration along the x-axis (same thin wall as Mode 14) and bending structural mode of movable focus group around the x-axis (motions of the bench and movable focus group are almost equally dominant)
16	1761.7	Combined structural mode of the bench as axial vibration along the x-axis (two of the thin walls) and bending around the y-axis (corner of another thin wall) and bending structural mode of the second movable zoom group around the y-axis and bending structural mode of movable focus group around the x-axis (motion of the bench is more dominant)
17	1782.4	Bending structural mode of the first movable zoom group and movable focus group around the x-axis, bending structural mode of the second movable zoom group around the y-axis and structural mode of the bench as axial vibration along the x-axis (motion of the bench is more dominant, followed by the second zoom group and movable focus group)

Table 3.6 (cont'd)		
18	1870.2	Combined structural mode of the bench as bending mode around the y-axis and axial vibration along x-axis, bending structural mode of the second zoom group around the y-axis, and bending mode of movable focus group around the x-axis, (motion of the bench is more dominant, followed by movable focus group)
19	1991	Combined structural mode of the bench as axial vibrations along the x and y axes and bending mode around the x-axis, bending mode of the second movable zoom group around the y-axis and bending mode of movable focus group around the x-axis (motion of the bench is more dominant)
20	2043.7	Bending structural mode of the bench around the x-axis (the corner of the same wall as Mode 16)

In the animations of each of these mode shapes, it was observed that all optical parts had both rigid body motion and elastic deformation. Furthermore, the movable groups had their own modes, which was expected since they were bonded to the external optomechanical components by only the surfaces of the pins at both sides as described in Section 3.2. However, the elastic deformation could not be isolated in the finite element analysis as emphasized by Genberg et al. [3]. The frequencies in Table 3.6 all belong to structural modes rather than elastic modes of the adhesives, which were in the range of 8950 to 9350 Hz as verified in the finite element analyses of the movable zoom groups on their own, whose details are presented in Sections 3.3.1 and 3.3.2. The first mode shape of the optomechanical system is presented in Figure 3.24.
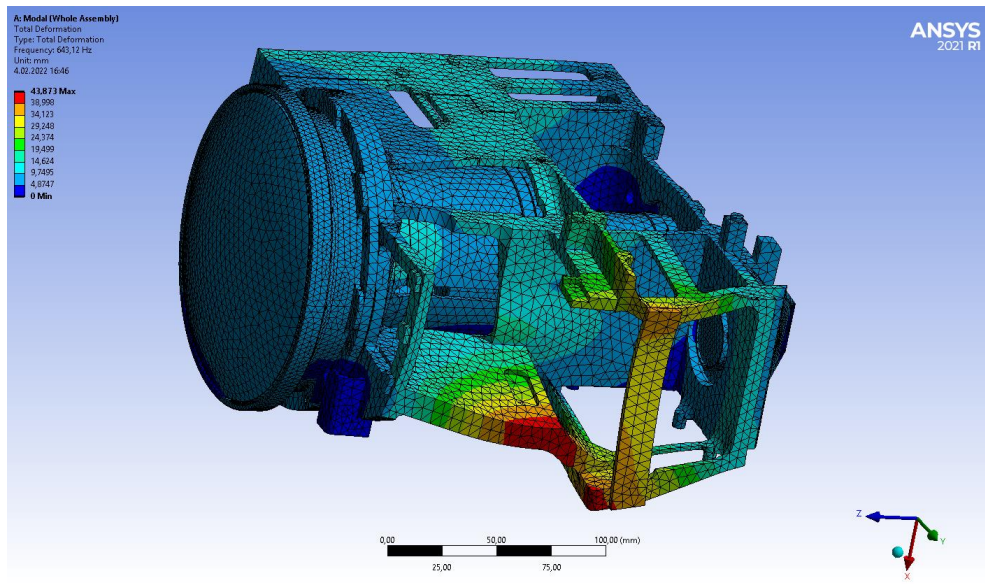
Figure 3.24. First mode shape of the optomechanical system at 643 Hz

The primary result of the modal analysis is that the lowest natural frequency of the optomechanical system is 643 Hz, which is far above the requirement of 100 Hz. The shapes of the first 20 modes imply that except Mode 5, all of the first 9 modes belong to the bench; and except Mode 20, all of the remaining 11 modes are various combinations of the optical sub-assemblies and the bench. The mode shapes are exported from ANSYS into SigFit by adding the related command snippet under the "Solution" tab in "Modal". Further details of this are presented in Chapter 4. With modal analysis results of the optomechanical system at hand, harmonic analysis was also performed; whose results were also necessary for SigFit. This analysis is presented in the following Section 3.4.

3.4 Harmonic Finite Element Analysis

Harmonic response analysis was performed in order to determine the frequency response function (FRF) of the entire optomechanical system. A sinusoidal acceleration of 1g (9800 mm/s^2) was applied to the system in x-direction (the direction along which the system has lowest thickness) at a frequency sweep between 10 and 2000 Hz. The sinusoidal quantity was selected as 1g of acceleration

because this is the dynamic quantity for excitation amplitude that is most commonly applied in the sinusoidal vibration tests; and the direction was selected as the x-direction because this was the axis along which the optomechanical system had the lowest thickness and so it was the most compliant. The FRF was calculated in modal coordinates as a modal response function where all of the first 20 modes contributed to it, rather than by solving the equation of motion of the optomechanical system separately for each excitation frequency. This was because the software used in Chapter 4 recognized the FRF in the form of modal response function. Figure 3.25 shows the definition of the acceleration excitation that is applied to the system to obtain its FRF, and Figure 3.26 shows the plot of this FRF in linear spectrum form in terms of acceleration in mm/s^2.
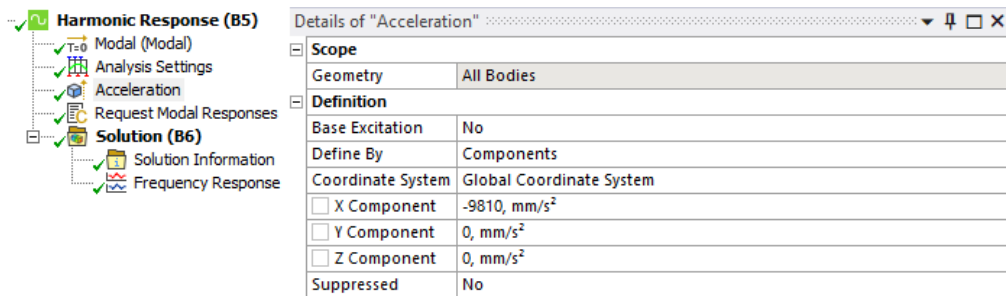
Figure 3.25. Definition of the 1g Acceleration in X-Direction
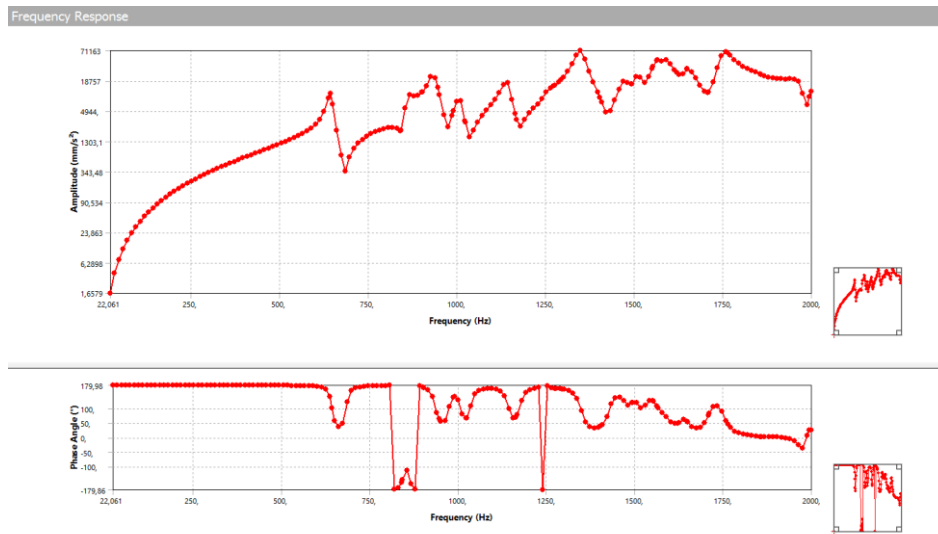
Figure 3.26. FRF of the optomechanical system in terms of linear spectrum and phase angle

The FRF indicates a peak at the natural frequencies of 643, 858, 934 Hz, and so on, as expected. This FRF is exported from ANSYS into SigFit by adding the related command snippet under the "Harmonic Response" tab. Further details of this are presented in Chapter 4. Before performing the Random Vibration finite element analysis, the stationarity of the random vibration data was tested by using the Run and Reverse Arrangement Tests, both of which are described in the following section.

3.5 Verifying the Stationarity of the Random Time-Domain Data

It was verified that the time domain data collected by the inertial measurement unit of the air platform in terms of the gravitational acceleration g was stationary by writing a MATLAB code (shown in Appendix A). Both run and reverse arrangement tests were applied to 32 samples, each containing 60000 data points with a sampling frequency of 400 Hz, amounting to a time of 150 seconds for each sample. The data did not satisfy the requirements of the Run Test, but it satisfied the Reverse Arrangement Test, resulting in stationarity. Afterwards, Fourier transform

was applied to the data to obtain the representative PSD input profile for the optomechanical system in this study.

Performing the Run Test resulted in the following sequence of pluses and minuses, which were represented in MATLAB as 1's and 0's, respectively as shown in Figure 3.27 below.

1x32 double													
1	2	3	4	5	6	7	8	9	10	11	12	13	14
0	1	0	1	1	1	1	1	0	0	1	0	1	0

1x32 double													
15	16	17	18	19	20	21	22	23	24	25	26	27	28
0	0	0	1	0	0	0	0	0	0	1	1	0	1

1x32 double			
29	30	31	32
1	0	0	0

Figure 3.27. Results of the Run Test for each of the 32 observations

As indicated in Figure 3.27, the number of 1's ("plus" observations) was 13 whereas the number of 0's ("minus" observations) was 19. Since the main assumption of the Run Test is that the numbers of "plus" and "minus" observations are equal, the Run Test could not be applied for this set of data to determine its stationarity. The table of values that would have been used for the Run Test is still presented in Appendix B for the sake of reference (Table B.1).

The Reverse Arrangements Test is another option to easily and reliably determine the stationarity of a wide variety of time records. Performing the Reverse Arrangements Test resulted in a value of 269, which is in the range from 201 to 302 as interpolated by using the values in Table B.2 in Appendix B for 32 samples and a confidence level of 95%. Thus, the 32 observations of the time-domain acceleration data are stationary according to the Reverse Arrangements Test as well.

Hence, the operational random environment can be considered as stationary and the regular statistical methods used for handling random data can be applied in this study. For example, the data can be assumed to have a normal (Gaussian) distribution and the term "sigma level" can be applied, which is very useful.

3.6 Random Vibration Finite Element Analysis

Even though the mode shapes and FRF were sufficient to calculate the effect of random vibration excitation on optical performance by using the SigFit software, Random Vibration analysis was also performed in ANSYS. The purpose of this analysis was to obtain the deformations of each optical component in x, y and z-directions, which could then be compared with the deformation results obtained through SigFit in Chapter 4. For additional data, the deformation of the whole optomechanical system in x, y and z-directions was also calculated. The z-direction was along the optical axis and normal to the optical surfaces. The x and y-directions were parallel to the focal plane array of the sensor, with the x-direction being along the thin side of the system.

First, the PSD excitation that was obtained from the air platform in g^2/Hz was entered. This PSD spectrum is shown in Table 3.7.

Table 3.7. The PSD excitation in g2/Hz entered for the Random Vibration analysis in ANSYS

	Frequency [Hz]	✔ G Acceleration [G²/Hz]
1	5,	1,5e-003
2	20,	1,5e-003
3	25,	9,e-002
4	35,	1,e-003
5	50,	1,e-003
6	65,	8,e-002
7	80,	3,e-002
8	130,	1,5e-003
9	200,	1,5e-003
*		

In the Analysis Settings, the damping ratio was selected as constant damping with a value of 0.01. "Directional Deformation" was selected as the quantity of interest. Here, the geometry was selected as "All Bodies", the orientation was selected as "X Axis" and the scale factor was selected as "3 Sigma". The 3-sigma scale factor was selected so that 99.73% of the data points in the response in time domain would not exceed the calculated deformation values in either direction. This

process was repeated for the y and z-directions by selecting the orientation as "Y Axis" and "Z Axis", respectively.

The maximum deformation that occurred in the optomechanical system in the x, y and z-directions were 0.001717, 0.0005071 and 0.0007119 mm (1.7, 0.5 and 0.7 micrometers), respectively. All three of these maximum deformations occurred at the bench rather than the optical components. The highest maximum deformation occurred in the x-direction, which was expected since that was the direction along which the optomechanical system was the most compliant.

Out of the optical components, the maximum deformations in x and z-directions were found to occur on the mechanics that held Optical Part 2 whereas the maximum deformation in y-direction occurred on Optical Parts 3, 4 and 8. The particular deformations of each optical component in x, y and z-directions were calculated and plotted on the components with a color code by selecting only that component in the geometry option with again 3-sigma scale factor. Again, red color shows the maximum deformation. Figures 3.28 and 3.29 show the color-coded deformation plots of the front and back surfaces of the large lens. Here, "front surface" refers to the surface through which the ray enters the optical part and "back surface" refers to the surface through which the ray exits the optical part.
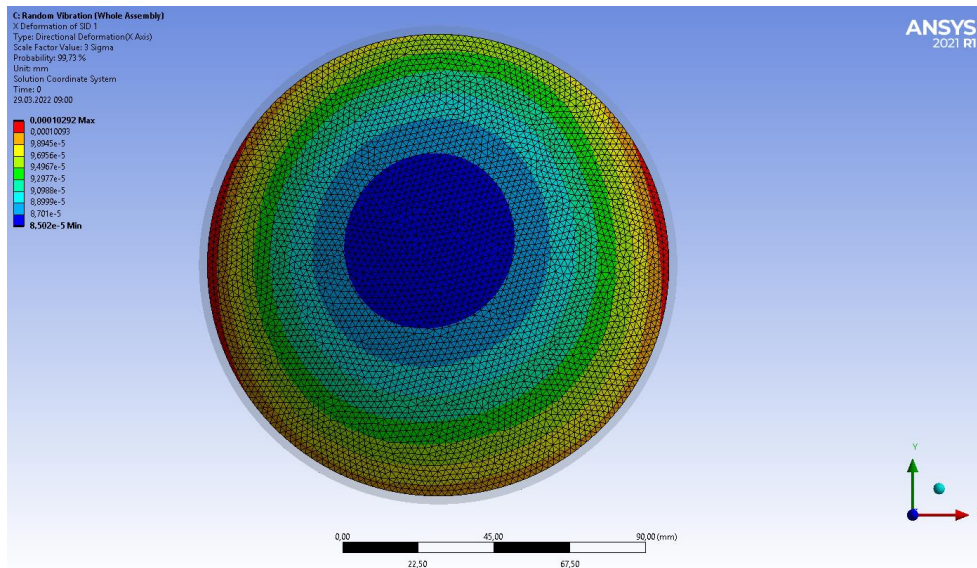
Figure 3.28. Deformation of Large Lens under the given PSD in X-direction (front surface)
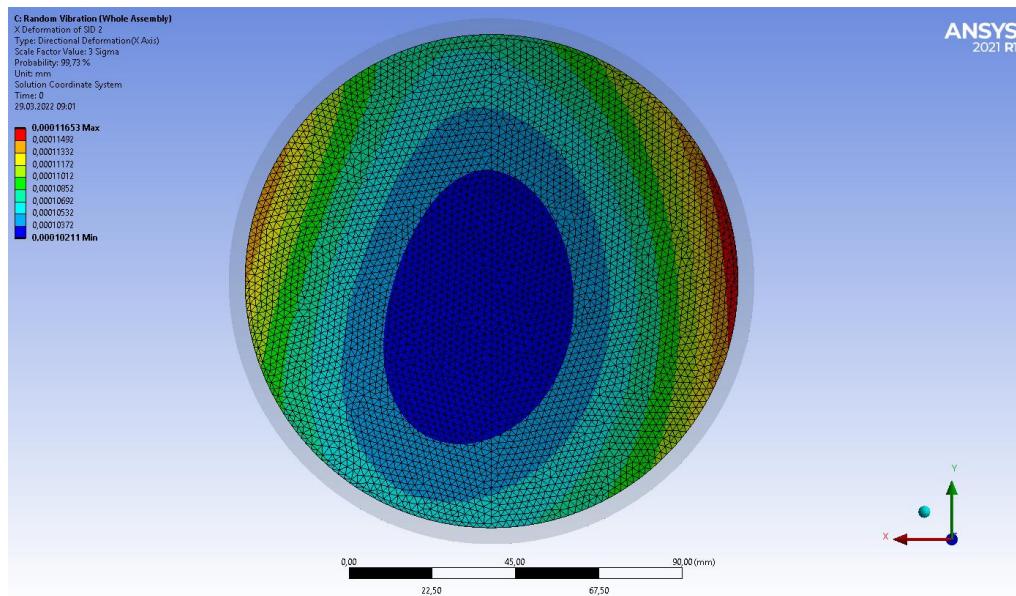
Figure 3.29. Deformation of Large Lens under the given PSD in X-direction (back surface)

Figures 3.28 and 3.29 show that in x-direction, the deformation on the back surface is greater than that on the front surface by an amount of roughly 0.01 micrometers (10%). Similar comments can be made for the other optical parts in all

69

three directions. Table 3.8 lists the maximum deformations observed in each optical component in x, y and z-directions under the PSD excitation shown in Table 3.7 with 3-sigma scale factor, and Figure 3.30 provides a column chart of these values for easier reading. It can again be noted that these deformations include both the rigid-body motion and the elastic deformation of the lenses. As Genberg et al. [3] emphasized, finite element solvers cannot separate these two components even though they may have completely different effects on optical performance.

Figure 3.30 indicates that the maximum deformation was observed in the x-direction (direction of lowest thickness and so highest compliance) for Movable Zoom Lens 2 (MZL2), followed by MZL3, MZL1 and CL (the lens closest to the image plane). From the same figure, it can also be observed that the highest average deformation was along the x-direction, followed by the z and y-directions. Thus, in the specialized software, mode shapes associated with these motions were expected to contribute the most to the line-of-sight jitter components and MTF reduction. Table 3.8 provides a detailed list of the numerical values of these deformations for each of the 9 optical components in the system, together with their averages and vector sums. The vector sum was calculated conservatively by assuming that all three maximum deformation components (x, y and z) on a component occurred at the same point even if this was not the case in the actual analysis results, and so taking the square root of the sum of their squares.

Table 3.8. Maximum deformations of the optical components in x, y and z-directions in micrometers under PSD excitation with 3-sigma scale factor as computed in Random Vibration Module of ANSYS 2021 R1

Optical Part	3-Sigma Maximum Deformation in x-direction (micrometer)	3-Sigma Maximum Deformation in y-direction (micrometer)	3-Sigma Maximum Deformation in z-direction (along the optical axis) (micrometer)	Vector Sum of Maximum Deformations (micrometer)
Large Lens (LL)	0.12	0.063	0.16	0.21
Movable Zoom Lens 1 (MZL1)	0.74	0.036	0.24	0.78
Movable Zoom Lens 2 (MZL2)	1.25	0.11	0.58	1.38
Movable Zoom Lens 3 (MZL3)	1.05	0.11	0.55	1.19
Mirror 1 (M1)	0.18	0.18	0.18	0.31
Movable Focus Lens 1 (MFL1)	0.23	0.27	0.24	0.43
Movable Focus Lens 2 (MFL2)	0.27	0.29	0.24	0.48
Mirror 2 (M2)	0.51	0.44	0.27	0.73

Table 3.8 (cont'd)				
Converging Lens (CL)	0.57	0.28	0.22	0.67
AVERAGE	0.55	0.20	0.30	0.69
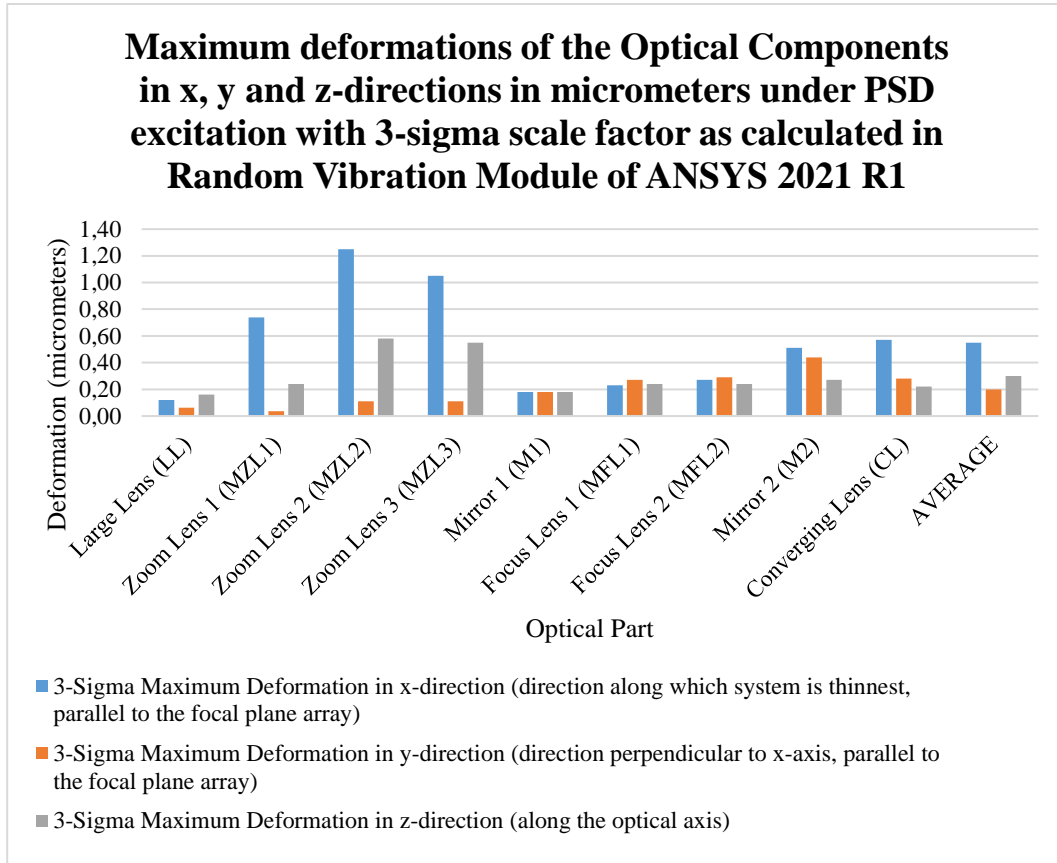
Figure 3.30. Maximum deformations of the optical components in x, y and z-directions in micrometers under PSD excitation with 3-scale sigma factor as calculated in Random Vibration Module of ANSYS 2021 R1

3.7 Finite Element Analysis of the Whole Optomechanical System with Adhesive Model Around Large Lens

As the results of Section 3.6 implied, when the interfaces of all lenses were modelled with bonded contacts and pinball regions, the optical part with the lowest

72

deformation under random vibration was the large lens, with a vector sum of only 0.21 micrometers. Since the rigidity of the adhesive interface was actually verified only around Movable Zoom Lenses 1, 2 and 3 in Sections 3.3.1 and 3.3.2 by applying Bonded contacts everywhere, another analysis was conducted to ensure that the effects of the adhesive's elasticity around other lenses were not disregarded. For this purpose, a second configuration (Configuration 2) of the finite element model was constructed. The definitions of these two configurations can be summarized as below.

- Configuration 1: Initial configuration that was analyzed in Sections 3.3 through 3.6 where all lenses and mirrors have pinball region bonded interface with their holders
- Configuration 2: The configuration analyzed in this section where there is an elastic (E = 2 MPa) adhesive model around only one optical component and all other optical components have the same pinball region bonded interface as Configuration 1

Since the large lens had the lowest deformation in Configuration 1, it was considered as the component most likely to have been over-constrained by the bonded contacts. So, the adhesive model was created around that component. Furthermore, the axial bonded contact between the large lens's shoulder and the flat surface of the holder was deleted to take any relative motion of the large lens with respect to adhesive into account. The definition of this deleted contact is shown in Figure 3.31.
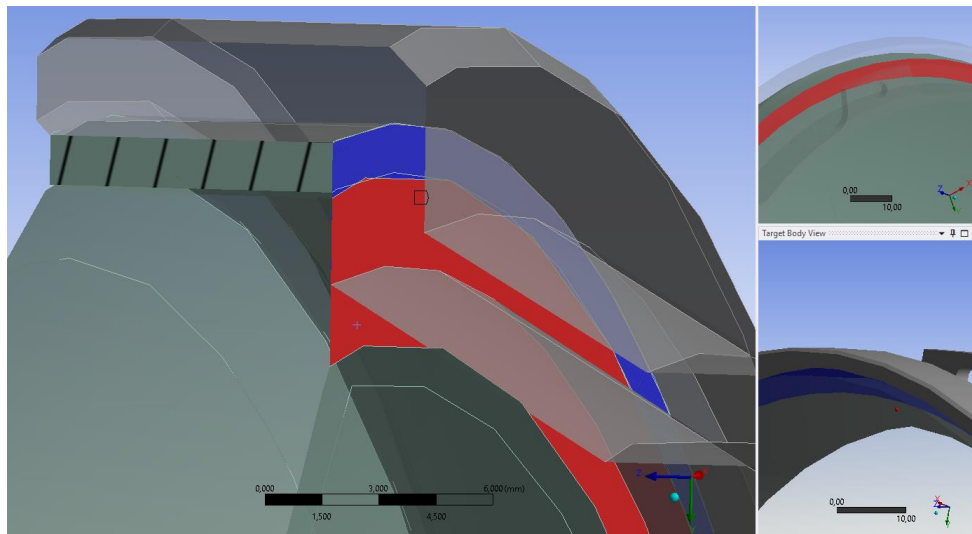
Figure 3.31. The deleted axial bonded contact for the large lens

The axial bonded contact of the lens was deleted because when the modal and random response analyses of the optomechanical system were made with the adhesive model around the large lens while still keeping the axial bond, the results turned out to be almost exactly the same as those presented in Sections 3.3 through 3.6, implying that the adhesive's low Young's modulus did not cause additional lens displacement as long as the axial bonded contact was active. The adhesive had the same material properties as in Table 3.1, with a Young's modulus of 2 MPa. Bonded contacts were defined between the diameters that were in direct contact with each other so that no additional pinball region was needed. The adhesive interface for the large lens was shown in Figures 3.2 and 3.3. As implied in these figures, one bonded contact was defined between the outer diameter of the lens and inner diameter of the adhesive model (shown in red color), and the other bonded contact was defined between the outer diameter of adhesive model and inner diameter of the optomechanical component that held the lens. The bonded contact that was defined between the lens's shoulder and the flat surface of the holder was deleted to take all possible relative motions of the lens with respect to adhesive into account. All other optical components had the same bonded contacts with pinball region as in Section 3.3.3. The same mesh sizes were applied as in Configuration 1, but there were also finer meshes applied to the adhesive model around the large lens with 1.2 mm for

the inner and outer diameter surfaces and 0.3 mm for the side surfaces with 5 divisions along the diameter edge, similar to Figure 3.17. This resulted in a total number of 976924 nodes and 524285 elements. The average quality of the meshes was 0.72 with a standard deviation of 0.21.

For this case, the first 20 natural frequencies and mode shapes were found as follows:

Table 3.9. First 20 natural frequencies and mode shapes of the optomechanical system when large lens has an adhesive model

Mode Number	Frequency (Hz)	Category
1	305.81	Oscillation of the large lens together with the adhesive along the z-axis (optical axis)
2	430.77	Bending mode of the large lens together with adhesive about the y-axis
3	431.89	Bending mode of the large lens together with adhesive about the x-axis (axis along which system is thinnest)
4	472.59	Bending mode of the large lens together with adhesive about the z-axis
5	582.21	Combined bending mode about the x-axis and oscillation along the y-axis of the large lens with adhesive
6	615.49	Combined bending mode about the y-axis and oscillation along the x-axis of the large lens with adhesive

Table 3.9 (cont'd)		
7	656.45	Similar to Mode 5, but the bench also has oscillation along the x-axis at one of its corners
8	871.66	Oscillation of the bench along the y-axis at its corner close to the large lens
9	968.05	Bending mode of the first movable zoom group about the y-axis together with bending of the bench about the x and y-axes (motion of bench is more dominant)
10	1023.6	Bending mode of the first movable zoom group about the y-axis
11	1032.9	Bending mode of the first movable zoom group about the y-axis together with bending mode of Mirror 2 and converging lens about the x-axis (motion of first movable zoom group is more dominant)
12	1147.8	Oscillation of the bench along the z-axis at its corner above the movable zoom groups together with bending of the movable focus group about the x-axis
13	1261.5	Oscillation of the bench along the z-axis at a corner close to Mirror 1
14	1279	Same as Mode 13 but there is also bending mode of the second movable zoom group about the y-axis (motion of bench is more dominant)
15	1351.5	Bending mode of both movable zoom groups together with Mirror 2 and Converging Lens about the x-axis

Table 3.9 (cont'd)		
16	1473.4	Expansion and contraction of the first movable zoom group along the z-axis together with bending of Mirror 1 and movable focus group about the x-axis and bending of Mirror 2 about z-axis (motion of first movable zoom group is more dominant)
17	1527.6	Same as Mode 16 but the bending motions of Mirror 1, movable focus group, and Mirror 2 are more pronounced (motion of the first movable zoom group is still dominant)
18	1584.6	Same as Mode 16 with bending mode of movable focus group and Mirror 2 about the x-axis
19	1640.4	Oscillation of the bench surface along the x-axis
20	1645	Same as Mode 19 with bending mode of movable focus group about the x-axis

As presented in Table 3.9, the lowest natural frequency of the optomechanical system in Configuration 2 is 305 Hz, which is 52% lower than that in Configuration 1 (643 Hz). The shapes of the first 20 modes imply that all of the first 7 modes belong to the large lens with adhesive. Except for Modes 8, 13 and 19, all of the remaining 13 mode shapes involve motions of Movable Zoom Group 1, Movable Zoom Group 2, Movable Focus Group, and Mirrors 1 and 2. So, it can be concluded that introducing a flexible adhesive model around the large lens has reduced the lower natural frequencies significantly by creating their own mode shapes. Again, the mode shapes are exported from ANSYS into SigFit by adding the related command snippet under the "Solution" tab in "Modal". Figure 3.32 shows the first mode shape at 305 Hz.
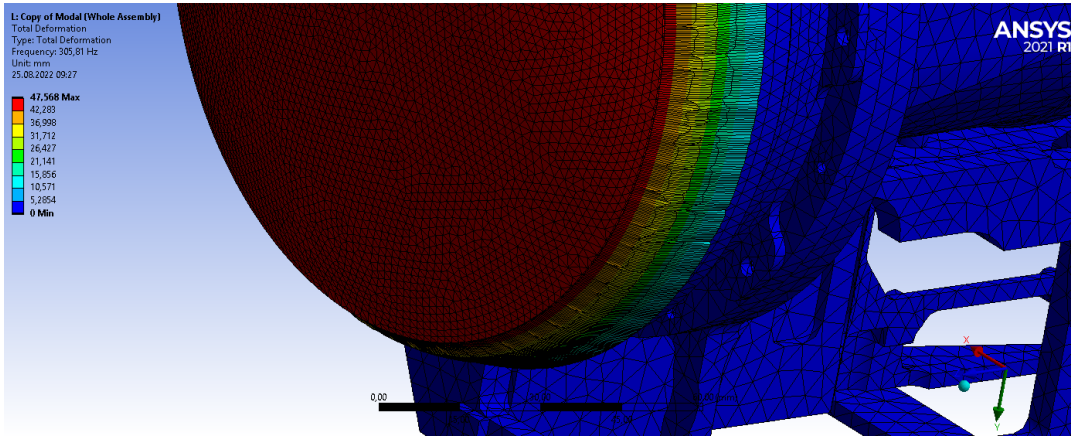
Figure 3.32. First mode shape of the optomechanical system with adhesive model around large lens at 305 Hz

With the results of modal analysis at hand, harmonic response analysis was also conducted with the same load and settings as Section 3.4. The corresponding frequency response function and phase angle diagrams are shown in Figure 3.33 below. The FRF exhibits peaks at the new natural frequencies starting with 305 Hz.
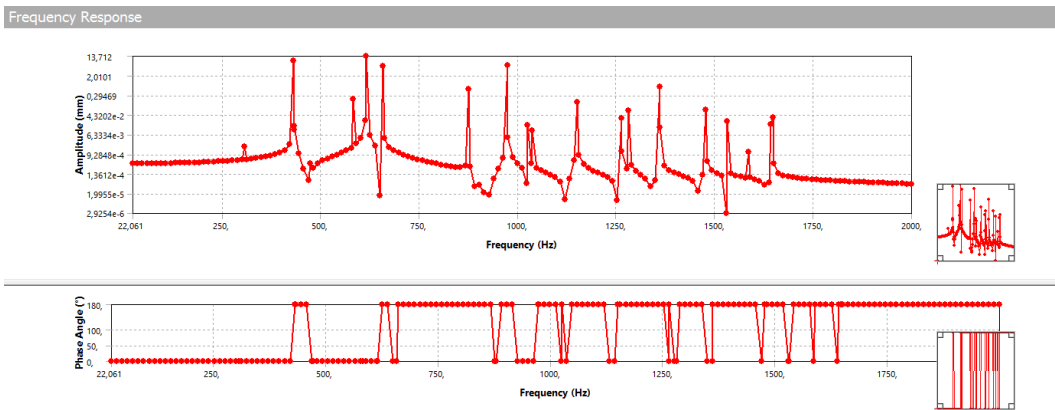
Figure 3.33. FRF of the optomechanical system in terms of linear spectrum and phase angle when large lens has adhesive model

Finally, with the PSD data whose stationarity was verified in Section 3.5, random response analysis was again conducted.

The maximum deformation that occurred in the optomechanical system in the x, y and z-directions were 0.004147, 0.001067, and 0.0041088 mm (4.15, 1.07 and

4.11 micrometers), respectively. All three of these maximum deformations occurred at the bench rather than the optical components. The highest maximum deformation occurred in the x-direction, which was expected since that was the direction along which the optomechanical system was the most compliant. Compared to the initial configuration which indicated 1.7, 0.5 and 0.7 micrometers in x, y and z-directions, there was an increase of 143% (1.5 times) in x-direction.

The 3-sigma maximum deformation results for each optical component in Configuration 2 are also presented below in Table 3.10. The corresponding results in the previous configuration in Section 3.5 are also written below each value in parentheses for easy comparison.

Table 3.10. Maximum deformations of the optical components in x, y and z-directions in micrometers under PSD excitation with 3-sigma scale factor as computed in Random Vibration Module of ANSYS 2021 R1 when large lens has an adhesive model

Optical Part	3-Sigma Maximum Deformation in x-direction (micrometer)	3-Sigma Maximum Deformation in y-direction (micrometer)	3-Sigma Maximum Deformation in z-direction (along the optical axis) (micrometer)	Vector Sum of Maximum Deformations (micrometer)
Large Lens (LL)	4.14 (0.12)	0.062 (0.063)	0.25 (0.16)	4.14 (0.21)
Movable Zoom Lens 1 (MZL1)	0.76 (0.74)	0.019 (0.036)	0.21 (0.24)	0.78 (0.78)
Movable Zoom Lens 2 (MZL2)	0.97 (1.25)	0.1 (0.11)	0.42 (0.58)	1.06 (1.38)
Movable Zoom Lens 3 (MZL3)	0.87 (1.05)	0.089 (0.11)	0.39 (0.55)	0.96 (1.19)
Mirror 1 (M1)	0.16 (0.18)	0.24 (0.18)	0.17 (0.18)	0.33 (0.31)
Movable Focus Lens 1 (MFL1)	0.16 (0.23)	0.22 (0.27)	0.13 (0.24)	0.30 (0.43)

Table 3.10 (cont'd)				
Movable Focus Lens 2 (MFL2)	0.21 (0.27)	0.24 (0.29)	0.13 (0.24)	0.34 (0.48)
Mirror 2 (M2)	0.52 (0.51)	0.4 (0.44)	0.17 (0.27)	0.68 (0.73)
Converging Lens (CL)	0.57 (0.57)	0.27 (0.28)	0.13 (0.22)	0.64 (0.67)
AVERAGE	0.93 (0.55)	0.18 (0.20)	0.22 (0.30)	1.03 (0.69)
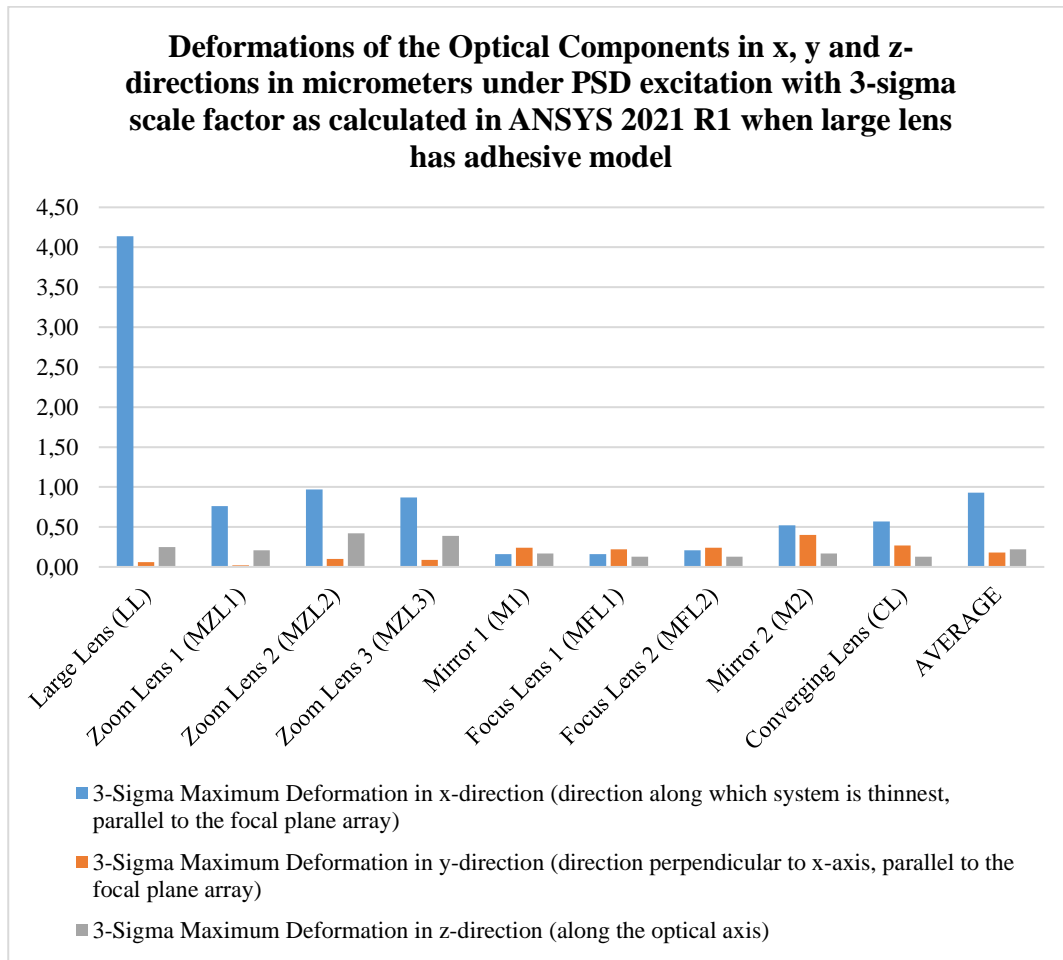
Figure 3.34. Maximum deformations of the optical components in x, y and z-directions in micrometers under PSD excitation with 3-scale sigma factor as calculated in Random Vibration Module of ANSYS 2021 R1 when large lens has adhesive model

As indicated in Table 3.10 and Figure 3.34, there is an order-of-magnitude increase in the maximum deformation of Large Lens in x-direction, whereas most other deformation components have either remained the same or decreased, including the deformations of Large Lens in the y and z-directions. This may be due to the PSD profile going up to only 200 Hz and so failing to excite the natural frequencies of the optomechanical system, which were in the range of 305 to 1645 Hz. Again, the highest average deformation occurs in x-direction, followed by the y and z-directions. The highest maximum deformation occurs on the Large Lens in x-direction, followed by Zoom Lenses 2, 3 and 1.

CHAPTER 4

CALCULATION OF THE OPTICAL PERFORMANCE PARAMETERS UNDER RANDOM VIBRATION

This chapter presents the optical peformance parameters that were calculated for the optomechanical system described in Chapter 3 by employing the files extracted from the finite element analysis in ANSYS 2021 R1. The line-of-sight errors in image space and object space, and the reduction in MTF due to the random excitation were calculated.

4.1 Description of the Software Interface

The 2020R1c version of the SigFit software developed by the Sigmadyne company was used. SigFit is a program that runs different analyses depending on the module that is selected at the start-up of the program. These modules include:

- Polynomial Fitting: Fitting of an even-degree polynomial onto the actual form of an optical surface, which can then be used to produce CSV plots of the static deformation of the surface with and without the subtraction of rigid-body motion. Using this module requires output of static deformation data from ANSYS. The coefficients of the polynomial are taken from the optical design data (prescription) and entered into VSigFit.
- Active Control
- Harmonic Response
- Random Response
- Transient Response
- Thermo-optic
- Stress-optic

- Stress-birefringence

In the scope of this study, the Random Response module was used. SigFit is normally executed through codes, but a graphical user interface called VsigFit is also developed, which conveniently enables the user to input all required parameters by writing them into the appropriate fields in the program. Different options can also be selected or enabled by using the drop-down lists or checkboxes. When VSigFit is first opened, a blank grey screen appears with the File, Edit and Help tabs on top. Clicking "New" through the file tab opens the analysis selection window shown in Figure 4.1.
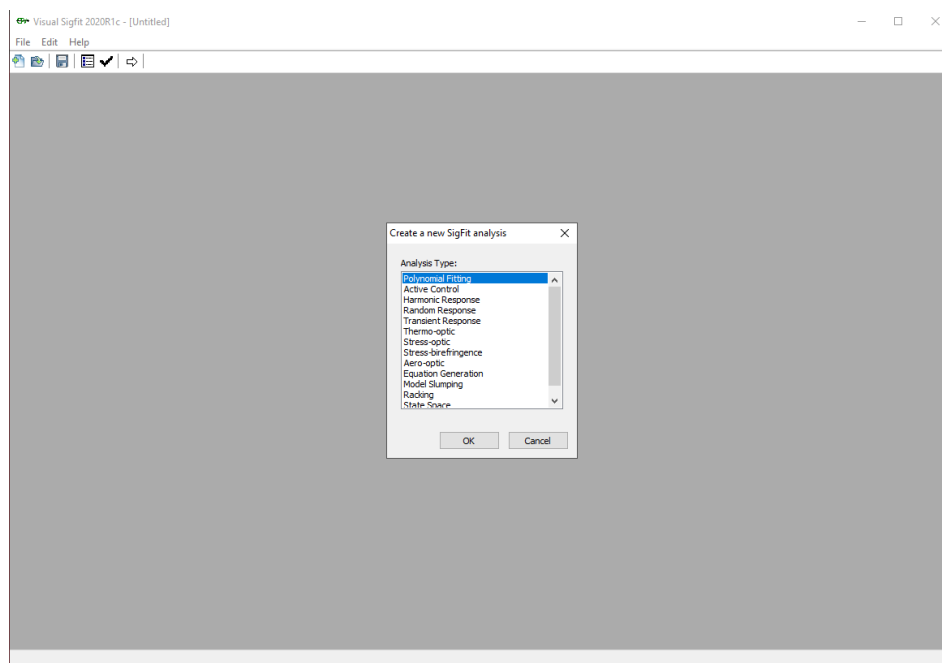
Figure 4.1. Analysis selection window of SigFit

4.2 Extracting the Required Data from ANSYS

In order to study the effect of random vibration on the optical performance of the optomechanical system, first the related data from the finite element analysis should be introduced to VSigFit so that the software recognizes the model it will

work with. This data includes the mode shapes from the "Modal" analysis and the FRF function of the optomechanical system from the "Harmonic Response" analysis.

In ANSYS, related commands should be introduced within the "Modal" and "Harmonic Response" analyses to extract the data. When these commands are executed, they produce a file with "asig" or "mcf" extension with the name stated in the command. These files are stored in the folders that contain the files related to the finite element analysis module. However, ANSYS can execute these commands only if the three library files that come with the installation of SigFit are placed in the related folder in ANSYS, which has been done for this study.

First, the following command was added under the "Solution" tab of the "Modal" analysis module of ANSYS, presented in Figure 4.2:
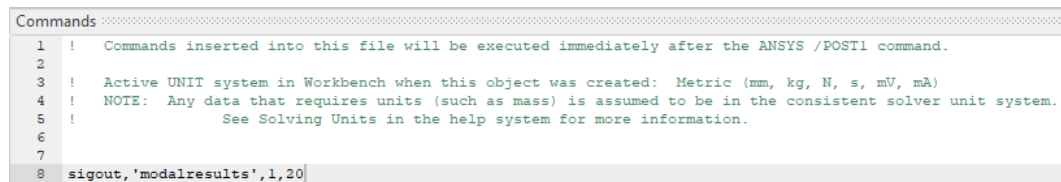

```
Commands
 1   !   Commands inserted into this file will be executed immediately after the ANSYS /POST1 command.
 2
 3   !   Active UNIT system in Workbench when this object was created:  Metric (mm, kg, N, s, mV, mA)
 4   !   NOTE:  Any data that requires units (such as mass) is assumed to be in the consistent solver unit system.
 5   !          See Solving Units in the help system for more information.
 6
 7
 8   sigout,'modalresults',1,20
```

Figure 4.2. The command written in Modal Analysis

The "sigout" command belonged to SigFit's own library, which ANSYS recognized after the SigFit library files were placed in its installation folder. This command produced the .asig file associated with the modal analysis. Then, the name of the .asig file was specified in single quotes next to "sigout", separated by a comma. The name was "modalresults" in this case since the .asig file contained the results of the modal analysis. In SigFit's syntax, all inputs and parameters are separated by commas. The last two values of "1" and "20" indicate the minimum and maximum mode numbers, respectively. They imply that the data associated with modes 1 through 20 (all first 20 modes) were included in the .asig file.

After the Modal analysis was through in ANSYS, the .asig file could be reached by right-clicking the "Solution" segment and selecting "Open Solver Files Directory", which led to the folder containing it.

Then, the following command was written under Harmonic Analysis, presented in Figure 4.3:


```
Commands
 1  !    Commands inserted into this file will be executed just prior to the ANSYS SOLVE command.
 2  !    These commands may supersede command settings set by Workbench.
 3
 4  !    Active UNIT system in Workbench when this object was created:  Metric (mm, kg, N, s, mV, mA)
 5  !    NOTE:  Any data that requires units (such as mass) is assumed to be in the consistent solver unit system.
 6  !               See Solving Units in the help system for more information.
 7
 8
 9  HROPT,MSUP,20,1,YES
```

Figure 4.3. The command written in Harmonic Analysis

Here, the "HROPT" command indicates that the harmonic response data is going to be extracted, "MSUP" indicates that modal superposition will be applied, "20" and "1" indicate the maximum and minimum modes, respectively, and the "YES" command is used to specify that it is desired to obtain the modal calculation files as output. This command produced the .mcf file, which could again be reached by right-clicking the "Harmonic Response" segment and selecting "Open Solver Files Directory".

The mode numbers specified in the modal analysis and harmonic response commands should be the same since SigFit compares the modes in the .asig and .mcf files. In this study, modes 1 through 20 were used for both commands.

With the acquisition of the .asig and .mcf files from the finite element analysis in ANSYS 2021 R1, the VSigFit software was started. The procedures performed in that software are described in the following sections.

4.3   Running the Software

The following data were input to SigFit before the run was started:

- Table of MTF values for the undisturbed optomechanical system (nominal MTF) as found from the optical design file
- Radii of curvature and other geometric parameters of each optical surface

- Working wavelength of the optomechanical system (an average of 4 micrometers was selected for the midwave-IR range in this study)

- Table of input PSD spectrum

- Integration time of the detector (9 milliseconds is selected for this study)

- Sigma level of the output results (one, two or three – three sigma is selected in the scope of this study)

- Destination of the .asig file in the computer used for analysis

- Destination of the .mcf file in the computer used for analysis

Care should be taken to ensure that the .asig and .mcf files correspond to the Modal and Harmonic Response analyses of the system in question. Then, the button is pressed and it is verified that there are no errors in the SigFit analysis definition. Screenshots of all related tabs in SigFit's Random Vibration module that are used in this study are presented in Figures 4.4 through 4.12.
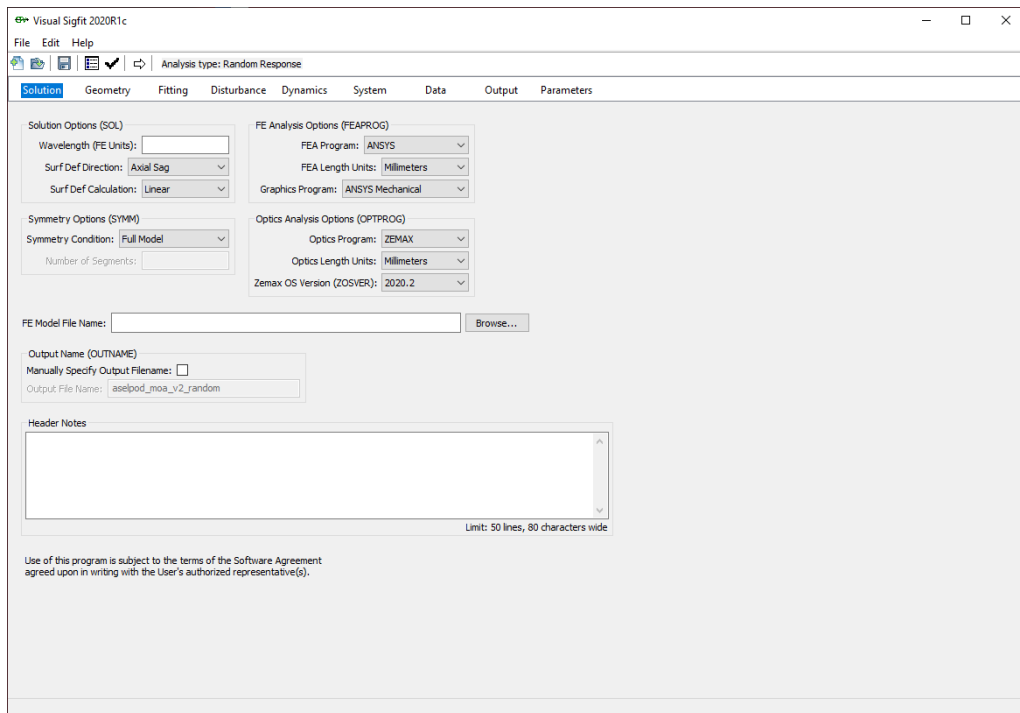
Figure 4.4. The Solution tab of VSigFit where the FEA program information and the .asig file are input
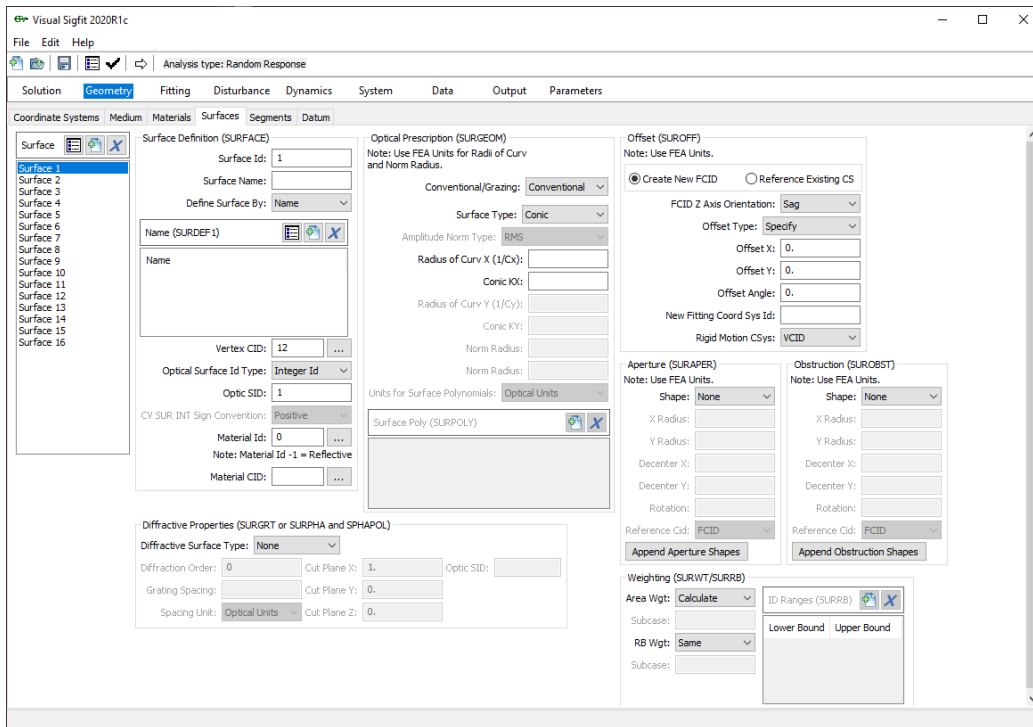
Figure 4.5. The Geometry tab of VSigFit where the data for each optical surface from the optical prescription and coordinate system IDs defined in the FE program are input
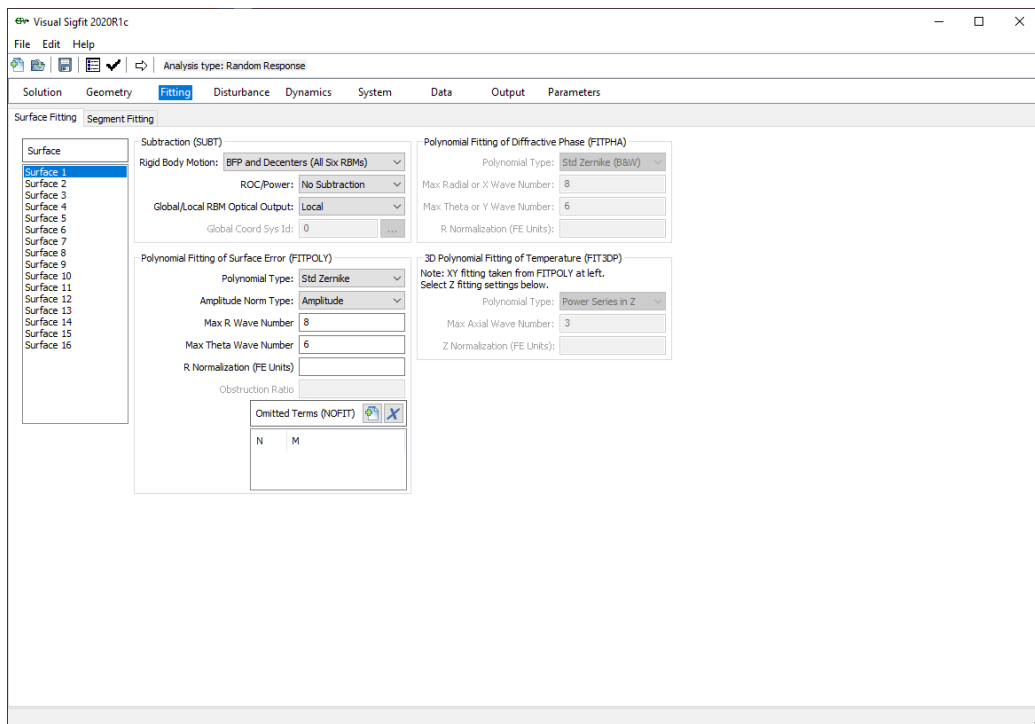
Figure 4.6. The Fitting tab of VSigFit where the options for polynomial fitting of surface error are selected
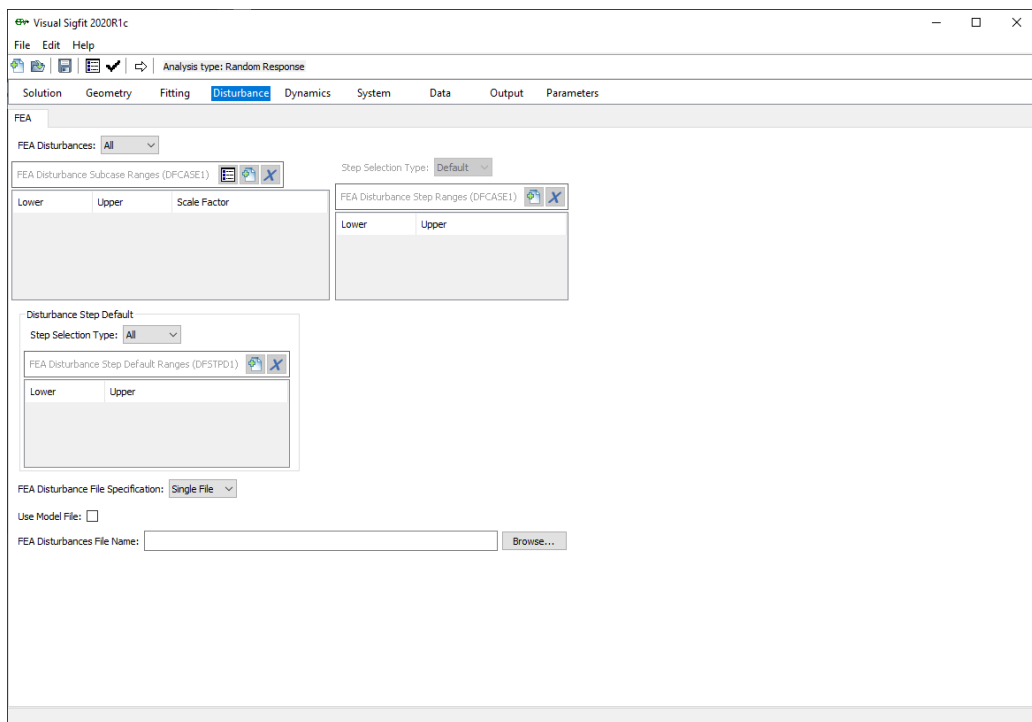
Figure 4.7. The Disturbance tab of VSigFit where the .asig file is again input
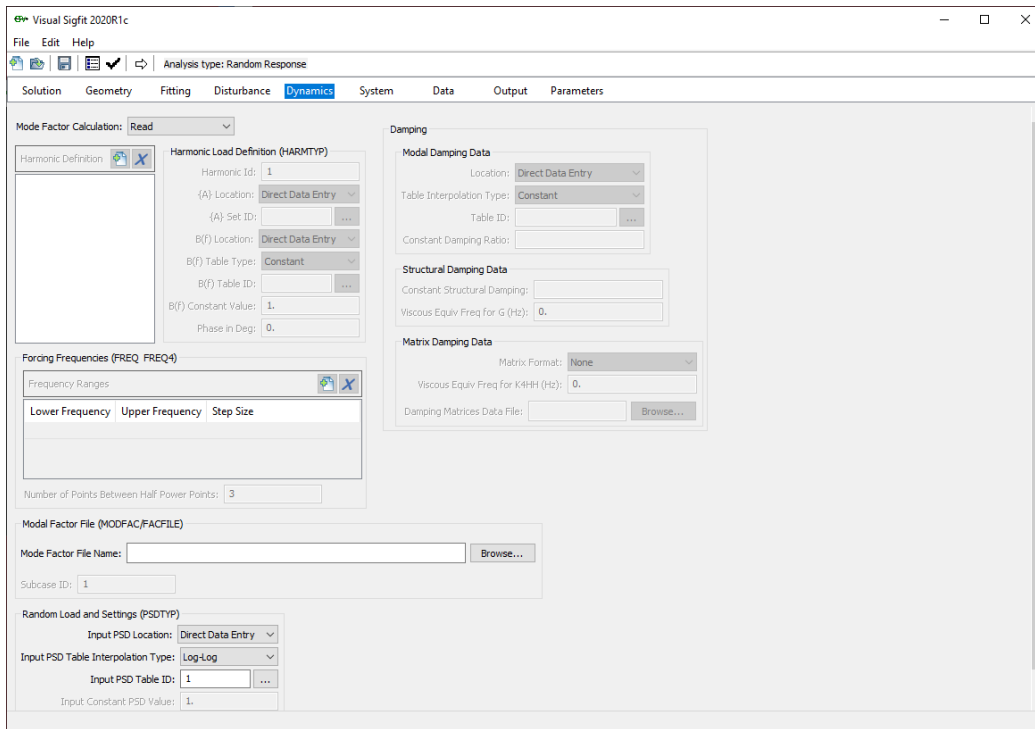
Figure 4.8. The Dynamics tab of VSigFit where the .mcf file is input
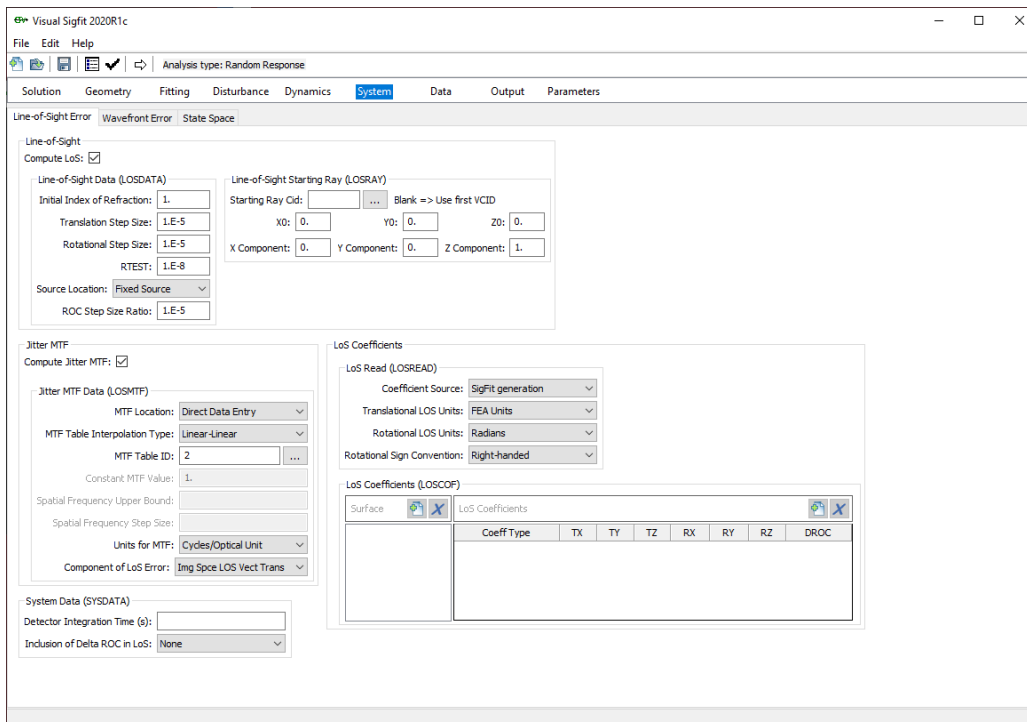
Figure 4.9. The System tab of VSigFit where the detector integration time is input
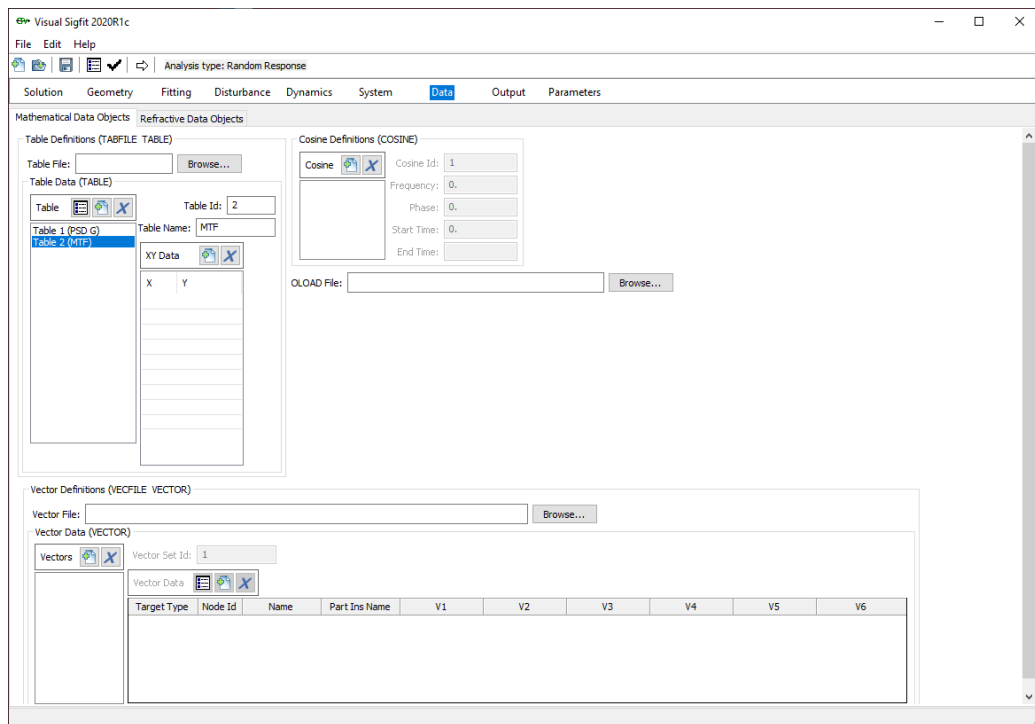
Figure 4.10. The Data tab of VSigFit where the tables of input PSD and nominal MTF values are written
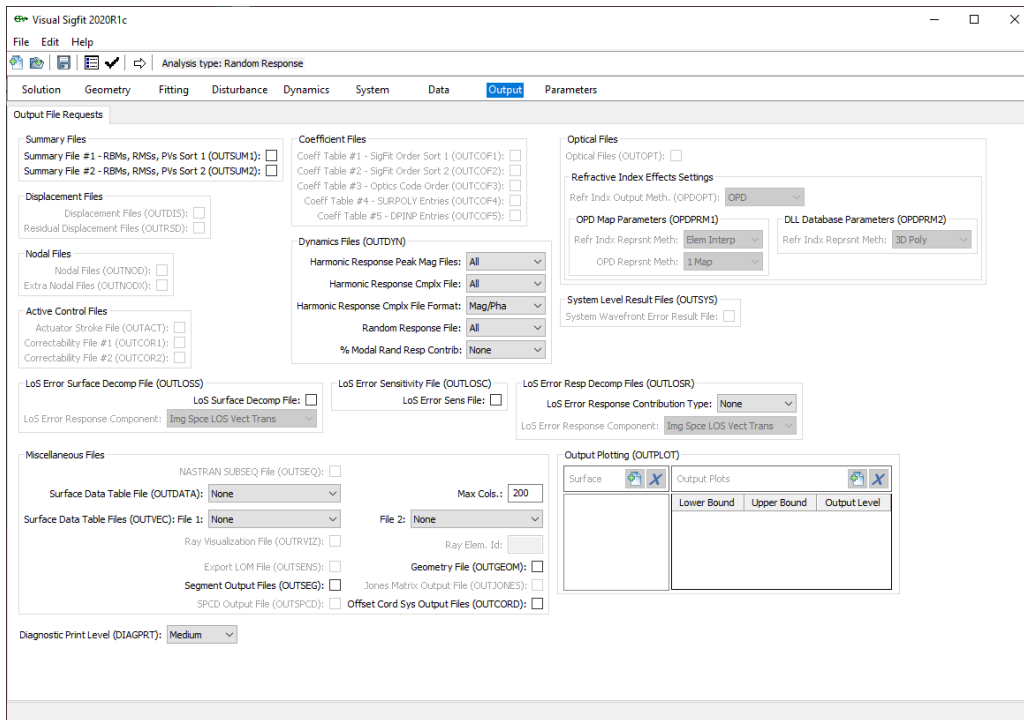
Figure 4.11. The Output tab of VSigFit where the diagnostic print level and additional outputs are selected if necessary
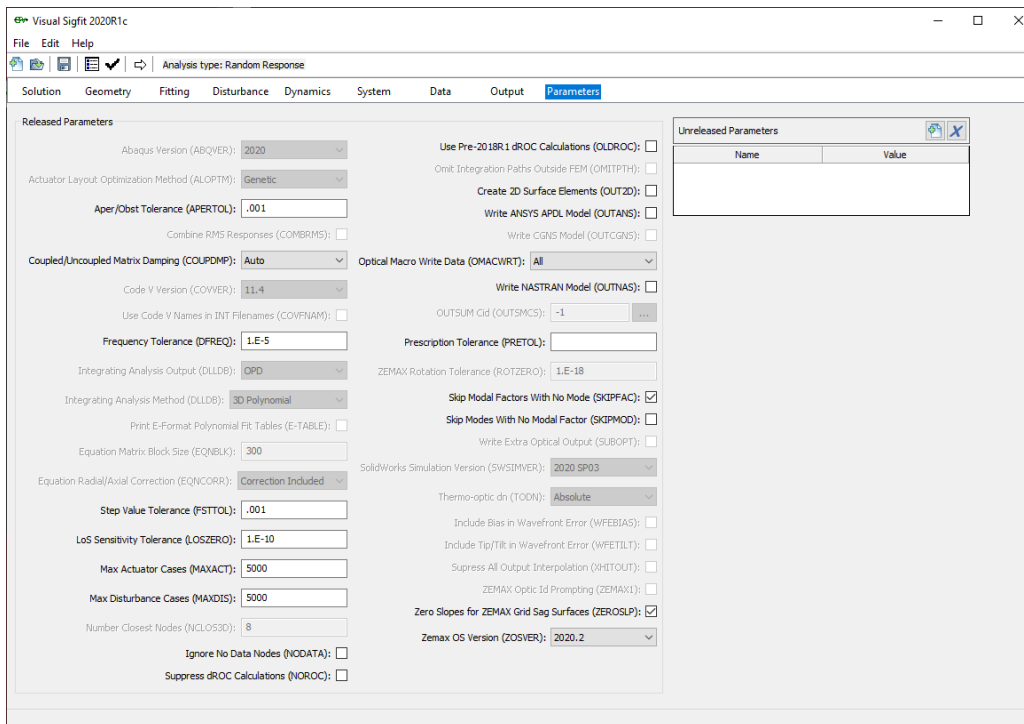
Figure 4.12. The Parameters tab of VSigFit containing other advanced options

4.4 Results and Plots

When SigFit's run is finished, it generates a result file with .fit extension. This file can be opened with the Notepad application. The numerical results can be directly read from here. These results include:

- All 6 components of the line-of-sight jitter displacement in millimeters or radians (2 translation components and 2 rotation components in image space, 2 rotation components in object space) and their corresponding in-plane vector sums)
- Percent contributions of each of the 20 modes of the optomechanical system to the line-of-sight jitter components
- The new MTF values of the optomechanical system after the random excitation is applied

4.4.1 Line-of-Sight Errors

SigFit calculates the overall displacement in the line-of-sight of the optomechanical system as well as the displacements of each optical surface in the six degrees of freedom. The line-of-sight displacement is considered in two separate groups: those caused by the fast jitter and those caused by the slow drift component of the random response. Drift is the slow and jitter is the fast component with respect to the detector integration time. The percentage contribution of each mode to both components in four degrees of freedom of the image space (translation and rotation along the x and y axes parallel to the FPA) and two rotational degrees of freedom of the object space (rotation about the x and y axes) is calculated separately. In this study, the line-of-sight displacement is calculated for three sigma so that the maximum value of displacement is not exceeded 99.7% of the time.

The line-of-sight displacement due to the jitter component of the random response, which is the component that directly affects the MTF under vibration, is considered in detail for the purpose of this study. The extracted results are shown in

Tables 4.1 and 4.2 for translational and rotational degrees of freedom, respectively. The 3-sigma acceleration has been shown in units of both millimeters per second squared and in terms of Earth's gravitational acceleration, g.

Table 4.1. Line-of-sight Jitter 3-Sigma Displacement, Velocity and Acceleration (Translations) due to Jitter Component of Random Response when all Optical Interfaces are Bonded

Degree of Freedom	3-Sigma Displacement (millimeters)	3-Sigma Velocity (millimeters per second)	3-Sigma Acceleration (millimeters per second squared)	3-Sigma Acceleration (g's)
LI-TX	6.23e-04	3.57e-01	245.62	0.025
LI-TY	3.85e-04	2.21e-01	152.21	0.015
LI-TV	7.33e-04	4.20e-01	288.96	0.029

The LI-TX and LI-TY components of 3-sigma displacement on the image plane of the optomechanical system, which are equal to around 0.62 and 0.39 micrometer are close to the average optical part displacement found in Table 3.8 by the Random Vibration module of ANSYS, which are 0.55 and 0.20 micrometer, respectively. The "LI-TV" value denoted the vector sum of the LI-TX and LI-TY components.

Table 4.2. Line-of-Sight Jitter 3-Sigma Displacement, Velocity and Acceleration (Rotations) in Image and Object Spaces due to Jitter Component of Random Response when all Optical Interfaces are Bonded

Degree of Freedom	3-Sigma Displacement (radians)	3-Sigma Velocity (radians per second)	3-Sigma Acceleration (radians per second squared)
LI-RX	5.94e-06	3.41e-03	2.35
LI-RY	5.04e-06	2.89e-03	1.98
LI-RV	7.79e-06	4.47e-03	3.08
LO-RX	1.10e-06	6.33e-04	0.436
LO-RY	1.79e-06	1.02e-03	0.703
LO-RV	2.1e-06	1.20e-03	0.827

In Table 4.2, "LI-RV" denoted the vector sum of the LI-RX and LI-RY displacement components in image space, and "LO-RV" denoted the vector sum of the LO-RX and LO-RY displacement components in object space.

SigFit also calculates the percent contributions of each mode to the line-of-sight jitter components and presents them in the results file. For the purpose of this study, the largest computed line-of-sight jitter translation (excluding the vector sum) was considered, which was "LI-TX". Figure 4.13 shows the color-coded pie chart of these contributions.
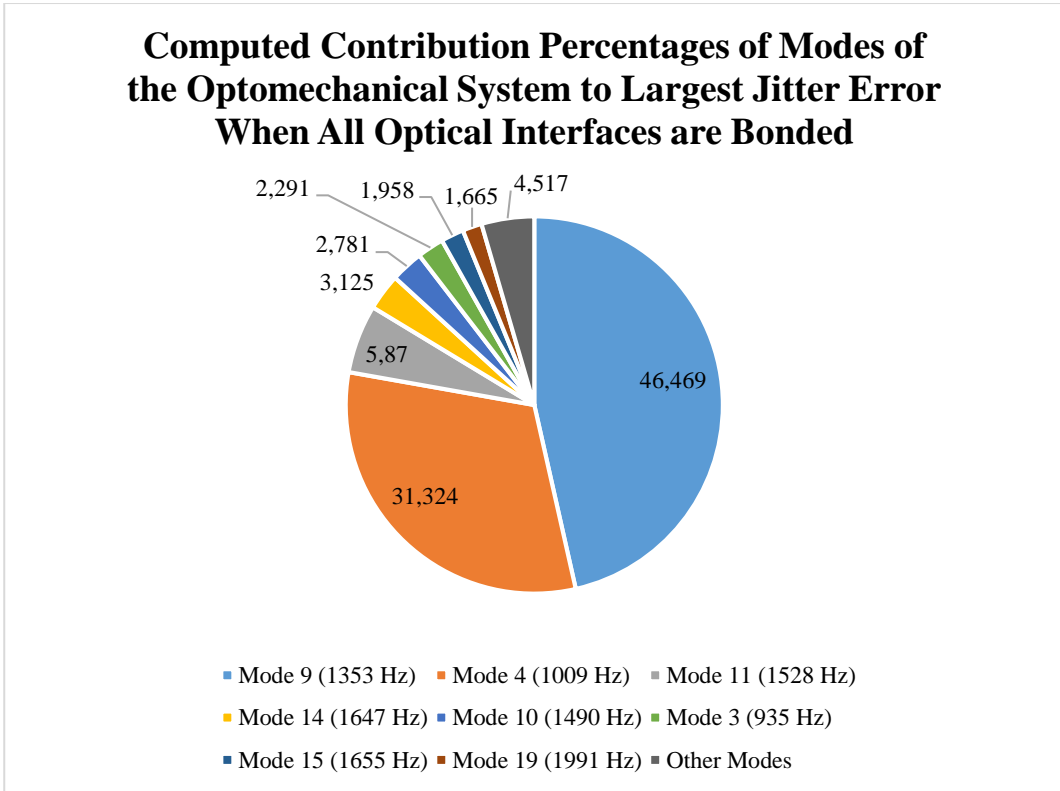
Figure 4.13. Computed contribution percentages of modes of the optomechanical system to largest jitter error when all optical interfaces are bonded

As indicated in Figure 4.13, when all optical interfaces in the system are modelled with bonded contacts, Mode 9 has the highest percent contribution to LI-TX, followed by Modes 4, 11, 14, 10, and 3. The mode numbers correspond to those presented in Table 3.6. From the details of the structural modes written in Table 3.6, it can be noted that the shape of Mode 9 involves significant movement of both Movable Zoom Groups 1 and 2 and the converging lens, which is close to the sensor's FPA (focal plane array). Thus, it is reasonable for Mode 9 to have the highest contribution (46%). The shape of Mode 4, which made the second-highest contribution of 31%, involved motion of the bench only rather than optical components. This also makes sense because the bench had the highest maximum deformation in the whole optomechanical system. Finally, the shape of Mode 11, which made the third-highest contribution of 5%, involved motion of all movable lens groups. This is also reasonable since the Movable Zoom Lens 2 (MZL2) had the

highest maximum deformation. Similar comments could be made about the other modes based on the components that moved in their mode shapes. This could provide insight about which modes contributed the most to line-of-sight jitter. So, necessary cautions could be taken to tune the highest-contributing mode frequencies higher and possibly out of the frequency range of interest.

The above results (line-of-sight jitter components and mode contribution percentages) were also obtained for the finite element model configuration (Configuration 2) in Section 3.7, where the pinball region bonded contact of the large lens was replaced with a flexible adhesive model and the axial bonded contact between the lens's shoulder and the holder surface was deleted. These results are presented as follows.

Table 4.3. Line-of-sight Jitter 3-Sigma Displacement, Velocity and Acceleration (Translations) due to Jitter Component of Random Response when Large Lens has an Adhesive Model

Degree of Freedom	3-Sigma Displacement (millimeters)	3-Sigma Velocity (millimeters per second)	3-Sigma Acceleration (millimeters per second squared)	3-Sigma Acceleration (g's)
LI-TX	4.89e-04	2.81e-01	193.54	0.0197
LI-TY	1.58e-04	8.94e-02	60.22	0.0061
LI-TV	5.13e-04	2.95e-01	202.70	0.0207

Table 4.4. Line-of-Sight Jitter 3-Sigma Displacement, Velocity and Acceleration (Rotations) in Image and Object Spaces due to Jitter Component when Large Lens has an Adhesive Model

Degree of Freedom	3-Sigma Displacement (radians)	3-Sigma Velocity (radians per second)	3-Sigma Acceleration (radians per second squared)
LI-RX	6.77e-07	4.03e-04	2.94e-01
LI-RY	4.34e-06	2.49e-03	1.71e+00
LI-RV	4.39e-06	2.52e-03	1.73e+00
LO-RX	4.52e-07	2.56e-04	1.72e-01
LO-RY	1.40e-06	8.04e-04	5.54e-01
LO-RV	1.47e-06	8.44e-04	5.80e-01

As implied by Tables 4.3 and 4.4, the line-of-sight jitter components are actually lower compared to those in Tables 4.1 and 4.2 for Configuration 1, even though the large lens was permitted more motion by introducing a flexible adhesive model. The largest jitter component is LI-TX in both configurations; but its value is 4.89e-04 millimeters for Configuration 2 whereas it is 6.23e-04 millimeters for Configuration 1, corresponding to a difference of 21.5%.

Figure 4.14. Computed contribution percentages of modes of the optomechanical system to largest jitter error when large lens has an adhesive model

As shown in Figure 4.14, Mode 9 has the largest contribution (63%) to the largest jitter component (LI-TX), followed by Modes 15, 20 and 16. However, the first 7 modes, whose shapes were associated with the recently introduced adhesive model, had almost zero contribution. This may be because these mode shapes mostly involved rigid body motion rather than elastic deformation, which corresponded to zero or very low frequencies. Jitter, however, is related to elastic deformations at higher frequencies.

4.4.2   Reduction in MTF

The final main optical performance parameter calculated by SigFit is the reduction in MTF due to the line-of-sight jitter caused by random vibration. Table 4.5 shows the percent reduction in MTF due to jitter.

Table 4.5. Percent Reduction in MTF due to Jitter as Calculated by SigFit when all Optical Interfaces are Bonded

Frequency (line pairs/mm)	Percent Reduction in MTF Caused by Jitter
10	0.106%
13	0.179%
18	0.343%
23	0.559%
30	0.950%
35	1.29%
40	1.68%
50	2.62%
60	3.75%

SigFit calculates the net MTF under random PSD by multiplying the jitter PSD (which is calculated from Equation 1.5) by the nominal MTF values found in the optical design file. There is a reduction in MTF after the random PSD profile given in Table 3.7 is applied, which is expected.

The above results were also obtained for the finite element model configuration (Configuration 2) in Section 3.7, where the pinball region bonded contact of the large lens was replaced with a flexible adhesive model and the axial bonded contact between the lens's shoulder and the holder surfaces was deleted. These results are presented as follows.

Table 4.6. Percent Reduction in MTF due to Jitter as Calculated by SigFit when Large Lens has an Adhesive Model

Frequency (line pairs/mm)	Percent Reduction in MTF Caused by Jitter
10	0.052%
13	0.088%
18	0.169%
23	0.276%
30	0.468%
35	0.638%
40	0.831%
50	1.295%
60	1.86%

Table 4.6 implies that for Configuration 2, the percent MTF reduction due to jitter is even lower compared to that in Configuration 1 in all spatial frequencies in lp/mm. A possible reason may be that the application of double bonded contact (both between the adhesive's inner and lens's outer diameters and the adhesive's outer and lens holder's inner diameter) may have reduced the mobility of the large lens despite the adhesive's low Young's modulus. In Configuration 1, only one bonded contact with pinball region was used for the same lens.

CHAPTER 5

MEASUREMENT OF THE OPTICAL PERFORMANCE PARAMETERS UNDER RANDOM VIBRATION

In this chapter, experimental measurement of the reduction in MTF due to random excitation for two physically assembled optomechanical systems is presented. In the experimental part of this study, it was aimed to perform the following measurements:

- Measurement of the MTF without random vibration excitation
- Measurement of the MTF under jitter due to random vibration excitation

Then, the percentage difference between these measured MTF values was calculated and presented in this study.

For experimental measurement of MTF, the following apparatus were used:

- Two physically assembled optomechanical systems of the same design
- Portable collimator
- Lifter on wheels carrying the collimator
- Half-moon target
- Shaker table
- Computer connected to the shaker table
- Laptop connected to the portable collimator
- Fixture for the optomechanical system so that it could be mounted onto the shaker

The optomechanical system was mounted onto the shaker table by using the fixture and the appropriately sized screws. The fixture acted as a mechanical interface between the system and the shaker. The height of the collimator was

adjusted by using a lifter so that the optomechanical system would face the target inside the collimator properly. The target was selected as a half-moon target. A half-moon target is one where one half of the target has pitch black and the other half has white color, providing an ideal image for MTF measurement. It was looked at the middle of the separation between these halves through the optomechanical system. The real-time image of the half-moon target was viewed on the laptop connected to the detector as the MTF data was continuously measured and recorded. The MTF was measured both at room temperature in the nominal conditions without random excitation and under the random excitation with the specified profile in Table 3.7. Figures 5.1 through 5.3 show the preparation of the setup for these measurements, and Tables 5.1 through 5.5 list the specifications for the setup. Further information about these specifications can be retrieved through the web sites of the manufacturers [29 – 32].
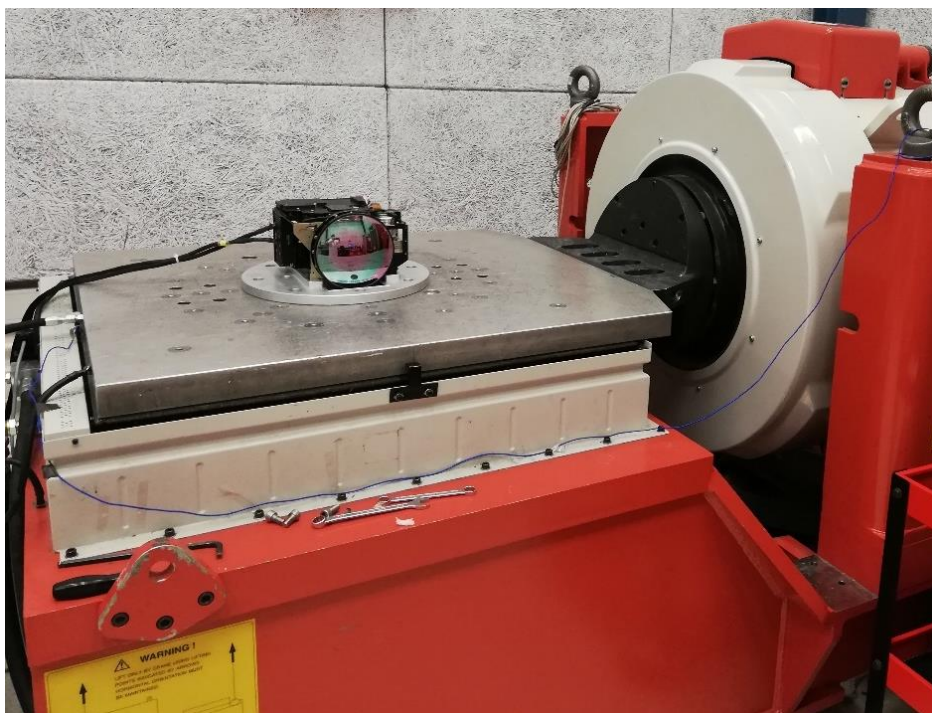
Figure 5.1. The optomechanical system fixed onto the shaker table
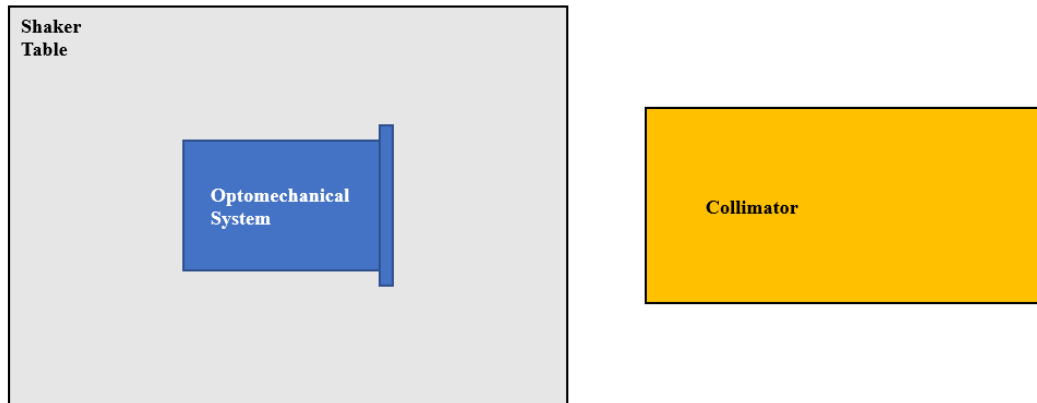
Figure 5.2. Top-view sketch showing the adjustment of the portable collimator in front of the optomechanical system placed on the shaker table

Figure 5.3. Open cover of the collimator showing the target wheel

Table 5.1. Specifications of the Shaker [29]

Name and Contact Information of Manufacturer	Bruel & Kjaer VTS Ltd. Jarman Way, Royston Hertford Shire SG8 5BQ UK Phone: +44 (0) 1223 389800 www.bksv.com
Product	Air Cooled Shaker
Model	V8-440 HBT900C M10-CE (V8-440-SPA56K)
Force Peak (kiloNewton)	66
Maximum Acceleration RMS (g)	100
Maximum Velocity (m/s)	2.5146
Maximum Positive Displacement (mm)	31.75
Maximum Negative Displacement (mm)	31.75
Maximum Drive Voltage (Volts)	5
Minimum Drive Frequency (Hz)	4 (or frequency of the direct current)
Maximum Drive Frequency (Hz)	2500
Effective Mass of Moving Elements (kg)	42

Table 5.2. Specifications of the Power Amplifier Connected to the Shaker [29]

Name and Contact Information of Manufacturer	LDS Test and Measurement Ltd. Jarman Way, Royston Herts, SG8 5BQ UK Phone: +44 (0) 1763 255255 www.lds-group.com
Product	SPA56K Amplifier
Power	56 kVA
Signal-to-Noise Ratio	>68 dB
Amplifier Efficiency	>90%
Rated Output Voltage	100 V RMS (sine)

Table 5.3. Specifications of the Shaker Control System [30]

Name and Contact Information of Manufacturer	Bruel & Kjaer VTS Ltd. Jarman Way, Royston Hertford Shire SG8 5BQ UK Phone: +44 (0) 1223 389800 www.bksv.com
Product	LASER USB Shaker Control System
Number of Channels	From 4 up to 16
Resolution	24-bit
Filtering	Analogue plus 160 dB/octave digital filter
Loop time	100 milliseconds
Dynamic Range	120 dBfs, 110 dB minimum in FFT Mode
Accuracy	±0.08 dB (1 kHz sine at full scale)

Table 5.4. Specifications of the Collimator [31]

Name and Contact Information of Manufacturer	CI Electro-Optical Systems, Inc. 1500 N. Interstate Highway 35, Suite C116, Carrollton, Texas 75006, USA www.ci-systems.com Mail: info@cisystemsinc.com
Product	METS-12-2.9 Collimator
Aperture (mm)	304.8 (12 inches)
Focal Length (mm)	1778 (70 inches)
Field of View (degrees)	2.9
Number of Target Positions	6
Collimator Type	Reflective, Off-Axis
Spectral Band (micrometers)	0.4 to 15
Operating Temperature Range (degrees Celsius)	10 to 35
Optical Resolution	Diffraction limited on axis
Radiation Source	SR-800 4D Differential Blackbody

Table 5.5. Specifications of the Lifter Carrying the Collimator [32]

Name and Contact Information of Manufacturer	Net Mak Metal Mak. San. ve Tic. Ltd. Şti. 2. OSB. Mah. 1. Yol No: 21 Hendek-Sakarya, Turkey www.netlift.com.tr info@netmak.com.tr
Product	NL-TTX50 Lifter
Load Capacity	500 kg
Dimensions of Table (mm)	1600 x 810
Minimum Table Height (mm)	290
Maximum Table Height (mm)	915

The random excitation was applied for 2 minutes by loading the PSD profile in Table 3.7 into the interface program in the computer that was connected to the shaker. As expected, the MTF was lower under random excitation because the oscillation of the shaker caused the oscillation of both the optomechanical system as a whole and each optomechanical component within their clearances, resulting in errors in the line-of-sight and preventing the optomechanical system from distinguishing the contrast between the halves as clearly. Table 5.6 presents the MTF data measured in the nominal conditions and under random vibration at 13 line pairs per mm.

Table 5.6. Percent reduction in MTF due to jitter caused by random vibration for Assembled Optomechanical System 1

Number of line pairs per mm (lp/mm)	Percent Reduction in MTF due to Jitter
13	9.83%

For Assembled Optomechanical System 1, the measured MTF values indicated that at 13 lp/mm, the MTF value was reduced by 9.83% due to random vibration. This is much higher than the computed percent reduction in Table 4.4, which was 0.179% (55 times lower). Possible reasons for this discrepancy are discussed in Chapter 6. This measurement was repeated for another physical assembly of the exact same optomechanical system, whose result is presented in Table 5.7 below.

Table 5.7. Percent reduction in MTF due to jitter caused by random vibrations for Assembled Optomechanical System 2

Number of line pairs per mm (lp/mm)	Percent Reduction in MTF due to Jitter
13	3.45%

For Assembled Optomechanical System 2, the measured MTF values indicated that at 13 lp/mm, the MTF value was reduced by 3.45% due to random vibration. While not as high as Optomechanical System 1, this is still much higher than the computed percent reduction in Table 4.4, which was 0.179% (19 times lower). Possible reasons for this discrepancy are discussed in Chapter 6. Keeping in mind that the fixture and the collimator's positions are not changed, the differences between the measured MTF percent reductions of Assembled Systems 1 and 2 may be due to the slight variations in the dimensions of the manufactured components. Even though very tight tolerances are applied during manufacturing, slight variations in the mating clearances of some components might have caused slightly different MTF reduction. Another possible reason is the mechanical noises coming from the adjacent shakers in the same laboratory. Since several tests are conducted at the same time for different projects in the same laboratory on a tight schedule, the amount of mechanical noises might have been slightly different for Systems 1 and 2 depending on when their MTF reductions were measured. Nevertheless, both optomechanical systems were considered to be acceptable for use on an air platform.

CHAPTER 6

SUMMARY AND CONCLUSIONS

6.1   Summary

This study aims to perform a detailed analysis of the effects of random vibration excitation on the optical performance of an optomechanical system. The purpose is to predict the effects of random excitation on the optical performance parameters of the optomechanical system accurately, especially MTF reduction, by using the appropriate simulation software. This enables the optomechanical designers to determine in advance whether their design will perform as required in the operational standard vibration environment and make the necessary design changes. Without such an analysis, the engineer is forced to rely on the vibration test results, which take place much later in the workflow; after the design is completed and the system is already manufactured. At that point, it is more expensive and time-consuming to make and realize the required design changes. So, this study attempts to improve the early vibration inspection points in the workflow by applying a specialized software to an actual complex optomechanical system consisting of 9 optical parts. It is also aimed to draw attention to the growing research field of predicting optical performance parameters under vibration loads through simulation.

In the scope of this study, a moderately complex optomechanical system consisting of 9 optical parts is subjected to modal and harmonic finite element analyses, through which the natural frequencies and frequency response function of the system are obtained, respectively. The time-domain acceleration data is collected from the air platform during its operation, from which the representative input random excitation PSD is obtained. The stationarity of the time-domain data is verified by the reverse arrangement test by writing the appropriate scripts in

MATLAB. So, the random excitation can be treated by the conventional statistical methods. Then, these pieces of data are introduced to the specialized software, which calculates the changes in optical performance parameters from the nominal values by the formulas that are outlined in this study. These parameters are reduction in MTF and line-of-sight jitter. The aforementioned simulation procedure is performed for two different finite element model configurations. In the first configuration, all lens and mirror interfaces are modelled as bonded contacts with pinball regions. In the second configuration, the interface of the large lens is modelled with an adhesive whereas all other interfaces are kept the same. The simulation results in both configurations are close to each other, results of the first configuration indicating slightly lower optical performance while the opposite was expected. The reduction in MTF is also verified physically by the appropriate experimental setup for two separate physical assemblies of the same design. The setup consists of a portable collimator on wheels, a shaker table and half-moon target. The specialized software indicated a much lower reduction in MTF compared to these measurements in both finite element model configurations, though. Possible reasons are discussed in the "Conclusions" section of this chapter.

6.2   Conclusions

Finite element analysis of the optomechanical system was conducted for two different configurations. In the first configuration (Configuration 1), all optical interfaces were modelled as bonded contacts with pinball regions. Based on the results of the analysis with this first configuration, a second configuration (Configuration 2) was created so that the interface around the lens with the lowest deformation was more flexible. The modal and harmonic response finite element analyses of the optomechanical system were completed each in 1 hour and 13 minutes. For Configuration 1, a mesh size of 5 mm was used for the optomechanical parts and 2 mm was used for the optical parts, resulting in a total number of 795183 nodes and 490300 elements. For Configuration 2, the same mesh sizes were applied, but there were also finer meshes applied to the adhesive model around the large lens

112

with 1.2 mm for the inner and outer diameter surfaces and 0.3 mm for the side surfaces with 5 divisions along the diameter edge. This resulted in a total number of 976924 nodes and 524285 elements. For both configurations, the average quality of the meshes was around 0.74 with a standard deviation of 0.24 and 0.21 for Configurations 1 and 2, respectively. The first 20 natural frequencies were calculated. For Configuration 1, the range of natural frequencies was 643 to 2043 Hz and for Configuration 2, the range of natural frequencies was 305 to 1648 Hz. For both configurations, it was found that while most mode shapes were structural modes of the bench carrying most of the optomechanical parts, there were also some mode shapes where the behavior of one of the movable groups was more dominant. Mode shapes of the large lens around the adhesive model were especially dominant for Configuration 2.

For the harmonic response analysis, a sinusoidal acceleration of 1g was applied in the direction along which the optomechanical system was the thinnest, for both configurations. The resulting frequency response function was a linear spectrum of the acceleration response amplitude in the frequency range from 10 to 2000 Hertz. The FRF exhibited peaks at the previously calculated natural frequencies. Due to the nature of response of a system to random PSD, obtaining the FRF was a prerequisite for running the specialized software and calculating the effects of random PSD on optical performance parameters.

In the random response analysis, the total deformations of the optical parts were found to be in the range of 0.04 to 1.2 micrometers for Configuration 1 and 0.02 to 4.1 micrometers for Configuration 2. The highest deformation belonged to Movable Zoom Lens 2, in x-direction, for Configuration 1 and Large Lens, again in x-direction, for Configuration 2. So, these deformations and the mode shapes associated with these degrees of freedom were expected to contribute the most to the reduction in MTF. The line-of-sight jitter and the percentage contributions of the modes to its largest component was calculated by the specialized software. For Configuration 1, Modes 9, 4 and 11 of the optomechanical system had the three highest contributions, both of which involved significant movement of Movable

Zoom Lens 2 and the bench. As expected, most of these modes were close to the higher end (2000 Hz) of the frequency range. For Configuration 2, however, the modes with the highest contributions (Modes 9, 15, and 20) did not involve the newly introduced adhesive model at all, which were only associated with the first seven modes. This was considered to be due to these modes possibly involving frequencies lower than the jitter threshold.

In both finite element model configurations, the specialized software indicated a much lower reduction in MTF compared to the measurements. The main possible reason is that the applied PSD profile was only up to 200 Hz (Table 3.7) whereas the lowest simulated natural frequency of the optomechanical system was 305 Hz. As a result, it is possible that none of the natural frequencies was excited while the random response of line-of-sight was being calculated, hence the minimal reduction in MTF. The discrepancy may also be due to the differences between the finite element model and the real-life physical assembly. For example, the axial clearance between the two movable zoom groups could not be modelled in FEA and the adhesive was modelled as an elastic material around only one lens, while leaving all other lenses with pinball region bonded contacts. The accuracy of the measurements was also affected by several factors, which included the inability to perfectly center the half-moon target in the collimator with respect to the optical path of the system. In this study, it was attempted to predict the MTF reduction in the early design phase of an optomechanical system while drawing attention to the research field of predicting optical performance parameters under vibration.

Table 6.1 shows the percentage differences between the computed and measured percent reductions in MTF and Figure 6.1 shows a comparative column chart of the measured and computed values.

Table 6.1. Percentage differences between the computed and measured MTF reductions

	Computed Percent Reduction in MTF when All Optical Interfaces are Bonded	Computed Percent Reduction in MTF when Large Lens has an Adhesive Model	Measured Percent Reduction in MTF	Percentage Difference between Closest Results
Optomechanical System 1	0.179%	0.088%	9.83%	5391.62% (55 times larger)
Optomechanical System 2	0.179%	0.088%	3.45%	1827.37% (19 times larger)

Table 6.2 shows the same results as normalized with respect to 1 by dividing all percent reductions by the highest data (9.83 in this case).

Table 6.2. Values of the percent reductions in MTF Normalized with Respect to 1

	Computed Percent Reduction in MTF when All Optical Interfaces are Bonded	Computed Percent Reduction in MTF when Large Lens has an Adhesive Model	Measured Percent Reduction in MTF
Optomechanical System 1	0.018%	0.009%	1%
Optomechanical System 2	0.018%	0.009%	0.35%
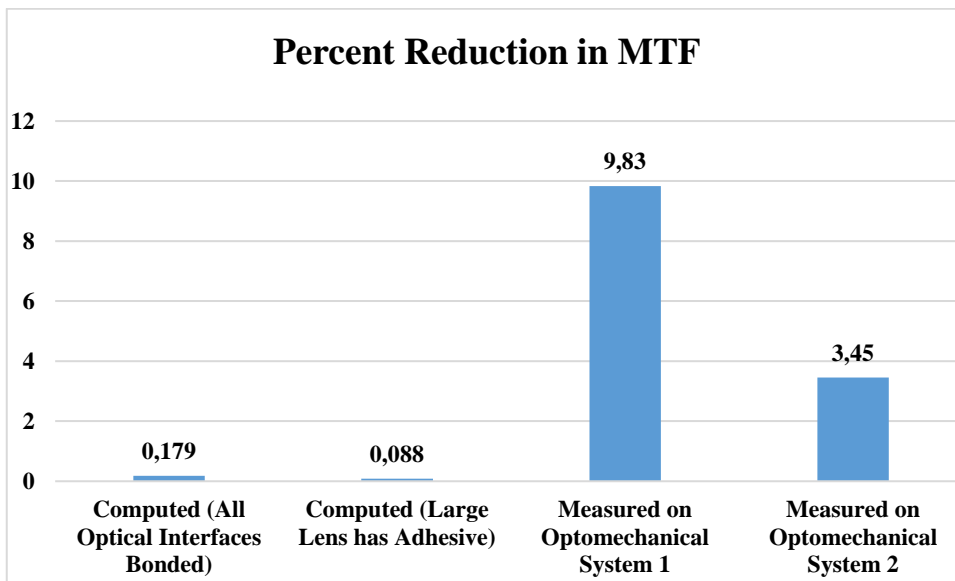
Figure 6.1. Comparative column chart of the computed and measured MTF reductions

As discussed above and Table 6.1 and Figure 6.1 indicate, there is a considerable, an order-of-magnitude difference, between the predicted and measured

MTF reduction values for both finite element model configurations (all lenses bonded and large lens with adhesive).

Even though the software and experimental MTF reduction results did not correlate with each other as targeted, this pilot study provided a solid basis and methodology upon which further, more sophisticated attempts can be made to better predict the MTF reduction of similar or even more complicated systems.

6.3   Future Work

This study can be further improved by:

- Repeating the analyses with a time domain data that was collected at a sampling frequency of at least 4000 Hz,

- Getting the finite element model of the optomechanical system close enough to real life such that its first natural frequency is 200 Hz or below to be able to recreate the MTF reduction caused by the PSD profile of 200 Hz in the tests,

- Repeating the analyses with other configurations where the adhesive model is introduced around each of the 8 remaining optical parts one by one,

- Verifying the natural frequencies of the optomechanical system with a hammer test,

- Considering the motors and electronic cards in the finite element model as solid bodies rather than point masses,

- Considering the axial clearance between the optical groups in the finite element model,

- Designing a set-up to ensure that the target in the collimator and the optical line-of-sight are as precisely aligned as possible,

- Isolating the legs of the lifter from the vibrational noises coming from the adjacent shakers,

- In the long run, conducting tests and experiments to determine the stiffness and damping coefficient of the adhesive used in this optomechanical system as a viscoelastic material.

REFERENCES

[1] U.S. Department of Defense (2019). *MIL-STD-810H: Department of Defense Test Method Standard, Environmental Engineering Considerations and Laboratory Tests*.

[2] Doyle, K. B., Genberg, V. L., & Michels, G. J. (2012). Integrated optomechanical analysis: second edition. https://doi.org/10.1117/3.974624

[3] Genberg, V. L., Michels, G. J., & Doyle, K. B. (2011). Integrated modeling of jitter MTF due to random loads. *Optical Modeling and Performance Predictions V*, *8127* (September 2011), 81270H. https://doi.org/10.1117/12.892585

[4] Kopeika, N. S., & Wulich, D. (1987). Image Resolution Limits Resulting From Mechanical Vibrations. *Optical Engineering*, *26*(6), 529–533. https://doi.org/10.1117/12.949624

[5] Kopeika, N. S., & Wulich, D. (1991). Image Resolution Limits Resulting From Mechanical Vibrations Part 2: Experiment. *Optical Engineering*, *30*(5), 577–589. https://doi.org/10.1117/12.55843

[6] Hadar, Ofer; Fisher, Moshe; Kopeika, N. S. (1992). Image resolution limits resulting from mechanical vibrations. Part III: numerical calculation of modulation transfer function. *Optical Engineering*, *31*(3), 581–589. https://doi.org/10.1117/12.56084

[7] Hadar, Ofer; Dror, Itai; Kopeika, N. S. (1994). Image resolution limits resulting from mechanical vibrations. Part IV: real-time numerical calculation of optical transfer functions and experimental verification. *Optical Engineering*, *33*(2), 566. https://doi.org/10.1117/12.153186

[8] Friedenberg, A. (2008). Simulation of the MTF due to low-frequency and correlated vibrations. *Journal of Modern Optics*, *55*(3), 401–407. https://doi.org/10.1080/09500340701453421

[9] Meza, L., Tung, F., Anandakrishnan, S., Spector, V., & Hyde, T. (2005). Line of sight stabilization for The James Webb Space Telescope. *Advances in the Astronautical Sciences*, *121*, 17–30.

[10] Kasunic, K. J. (2015). *Optomechanical Systems Engineering*.

[11] Vukobratovich, D., & Yoder, P. (2018). *Fundamentals of Optomechanics*.

[12] Hatheway, A. E. (2016). *The Optomechanical Constraint Equations: Theory and Applications*.

[13] Ahmad, A. (2017). *Handbook of optomechanical engineering: 2nd edition*. https://doi.org/10.4324/9781315153247

[14] Schwertz, K., & Burge, J. H. (2012). *Optomechanical Design and Analysis*.

[15] Doyle, K. B., Cerrati, V. J., Forman, S. E., & Sultana, J. A. (1995). Optimal structural design of the Airborne Infrared Imager. *Proc. SPIE Optomechanical and Precision Instrument Design*, *2542*(September 1995), 11–22. https://doi.org/10.1117/12.218659

[16] Bonin, D., & McMaster, B. (2007). Closed loop optimization of opto-mechanical structure via mechanical and optical analysis software. *Proc. SPIE Laser Radar Technology and Applications XII*, *6550*, 65500X. https://doi.org/10.1117/12.719574

[17] Avşar, A. L. (2008). *Dynamic Modeling and Analysis of Vibration Effects on Performance in Optical Systems* [Middle East Technical University]. http://etd.lib.metu.edu.tr/upload/12609778/index.pdf

[18] Unal, U. (2012). *Optomechanical Analysis and Experimental Validation of Bonding Based Prism and Mirror Mounts in a Laser System* [Middle East Technical University]. http://etd.lib.metu.edu.tr/upload/12614161/index.pdf

[19] Ke, D., Bo, Q., & Jiang, B. (2016). Integrated opto-mechanical optimization analysis of large-aperture primary mirror's support position. *8th International Symposium on Advanced Optical Manufacturing and Testing*

Technologies: Large Mirrors and Telescopes, *9682*(October 2016), 968213. https://doi.org/10.1117/12.2242881

[20] Serief, C. (2017). Estimate of the effect of micro-vibration on the performance of the Algerian satellite (Alsat-1B) imager. *Optics and Laser Technology*, *96*, 147–152. https://doi.org/10.1016/j.optlastec.2017.05.035

[21] McBride, W. R., & Stratton, M. (2018). Vibration measurements in the Daniel K. Inouye Solar Telescope. *Proc. SPIE 10700, Ground-Based And Airborne Telescopes VII*, *July 2018*, 16. https://doi.org/10.1117/12.2315038

[22] Pause, P. (2019). The sealed, the athermaled, and the rugged: the wild west of modified opto-mechanical design. *Proc. SPIE 10914, Optical Components and Materials XVI* (1091423, 27 February 2019). https://doi.org/10.1117/12.2509790

[23] Genberg, V. L., Michels, G., & Bisson, G. (2019). Structural optimization of system WFE. *Proc. SPIE 11100, Optomechanical Engineering 2019*, *1110007*(August 2019). https://doi.org/10.1117/12.2525436

[24] Serief, C., & Ghelamallah, Y. (2018). Dynamic MTF estimate of the optical imager onboard Alsat-1B satellite. *Proc. SPIE 11180, ICSO 2018*, *11180*(October 2018), 279. https://doi.org/10.1117/12.2536199

[25] Chen, Y., Xu, Z., Li, Q., & Feng, H. (2008). Image stabilization using motion estimation and micro-mechanical compensation. *Proceedings - 1st International Congress on Image and Signal Processing, CISP 2008*, *3*, 578–582. https://doi.org/10.1109/CISP.2008.663

[26] Zhu, Y., Wang, M., Cheng, Y., He, L., & Xue, L. (2019). An improved jitter detection method based on parallax observation of multispectral sensors for Gaofen-1 02/03/04 satellites. *Remote Sensing*, *11*(1). https://doi.org/10.3390/rs11010016

[27] Can Polat, H., Okan Atak, V., Kocabicak, I. E., Gurcay, E., Guven Gultekin, F., & Erdi Yanteri, E. (2019). Satellite imagery calibration and quality

assessment tests: GÖKTÜRK-1 case study. *Proceedings of 9th International Conference on Recent Advances in Space Technologies, RAST 2019*, 805–811. https://doi.org/10.1109/RAST.2019.8767436

[28] Thorby, D. (2008). Random Vibration. In *Structural Dynamics and Vibration in Practice* (pp. 267–324). https://doi.org/10.1016/b978-0-7506-8002-8.00010-9

[29] Bruel & Kjaer VTS Ltd., LDS V8 Shaker Systems. Available at: http://bruel.hu/wp-content/uploads/2020/08/LDS-V8.pdf. Last visited on 2022, Jul. 18.

[30] Bruel & Kjaer VTS Ltd., LDS LaserUSB Vibration Control System Data. Available at: https://www.bksv.com/-/media/literature/Product-Data/bu3079.ashx. Last visited on 2022, Jul. 18.

[31] CI Systems Inc., METS Modular Electro-Optical System. Available at: https://www.ci-systems.com/Files/METS.pdf. Last visited on 2022, Jul. 18.

[32] Net Mak. Metal Makina San. ve Tic. Ltd. Şti., Manuel Makaslı Platform NL-TTX 50. Available at: https://www.netlift.com.tr/Uploads/GenelDosya/nl-ttx50-100-8398.pdf. Last visited on 2022, Jul. 18.

APPENDICES

A. The MATLAB Code for Testing the Stationarity of the Data Used for PSD Input

```
clc;
clear all;
close all;
%%Loading the recorded .MAT file that contains the raw
%%acceleration data from the workspace
A = load('07_Bhy_455031_515030_[200903_113345]_[200903_113615].mat',
'AtaletselIvmeOlcerPitch');
A = A.AtaletselIvmeOlcerPitch;
B = load('08_Bhy_515031_575030_[200903_113615]_[200903_113845].mat',
'AtaletselIvmeOlcerPitch');
B = B.AtaletselIvmeOlcerPitch;
C = load('09_Bhy_575031_635030_[200903_113845]_[200903_114115].mat',
'AtaletselIvmeOlcerPitch');
C = C.AtaletselIvmeOlcerPitch;
D = load('10_Bhy_635031_695030_[200903_114115]_[200903_114345].mat',
'AtaletselIvmeOlcerPitch');
D = D.AtaletselIvmeOlcerPitch;
E = load('11_Bhy_695031_755030_[200903_114345]_[200903_114615].mat',
'AtaletselIvmeOlcerPitch');
E = E.AtaletselIvmeOlcerPitch;
F = load('12_Bhy_755031_815030_[200903_114615]_[200903_114844].mat',
'AtaletselIvmeOlcerPitch');
F = F.AtaletselIvmeOlcerPitch;
G = load('13_Bhy_815031_875030_[200903_114844]_[200903_115115].mat',
'AtaletselIvmeOlcerPitch');
G = G.AtaletselIvmeOlcerPitch;
H = load('14_Bhy_875031_935030_[200903_115115]_[200903_115345].mat',
'AtaletselIvmeOlcerPitch');
H = H.AtaletselIvmeOlcerPitch;
I = load('15_Bhy_935031_995030_[200903_115345]_[200903_115615].mat',
'AtaletselIvmeOlcerPitch');
I = I.AtaletselIvmeOlcerPitch;
J = load('16_Bhy_995031_1055030_[200903_115615]_[200903_115845].mat',
'AtaletselIvmeOlcerPitch');
J = J.AtaletselIvmeOlcerPitch;
K = load('17_Bhy_1055031_1115030_[200903_115845]_[200903_120115].mat',
'AtaletselIvmeOlcerPitch');
```

```
K = K.AtaletselIvmeOlcerPitch;
L = load('18_Bhy_1115031_1175030_[200903_120115]_[200903_120345].mat',
'AtaletselIvmeOlcerPitch');
L = L.AtaletselIvmeOlcerPitch;
M = load('19_Bhy_1175031_1235030_[200903_120345]_[200903_120615].mat',
'AtaletselIvmeOlcerPitch');
M = M.AtaletselIvmeOlcerPitch;
N = load('20_Bhy_1235031_1295030_[200903_120615]_[200903_120844].mat',
'AtaletselIvmeOlcerPitch');
N = N.AtaletselIvmeOlcerPitch;
O = load('21_Bhy_1295031_1355030_[200903_120844]_[200903_121115].mat',
'AtaletselIvmeOlcerPitch');
O = O.AtaletselIvmeOlcerPitch;
P = load('22_Bhy_1355031_1415030_[200903_121115]_[200903_121345].mat',
'AtaletselIvmeOlcerPitch');
P = P.AtaletselIvmeOlcerPitch;
Q = load('23_Bhy_1415031_1475030_[200903_121345]_[200903_121615].mat',
'AtaletselIvmeOlcerPitch');
Q = Q.AtaletselIvmeOlcerPitch;
R = load('24_Bhy_1475031_1535030_[200903_121615]_[200903_121845].mat',
'AtaletselIvmeOlcerPitch');
R = R.AtaletselIvmeOlcerPitch;
S = load('25_Bhy_1535031_1595030_[200903_121845]_[200903_122115].mat',
'AtaletselIvmeOlcerPitch');
S = S.AtaletselIvmeOlcerPitch;
T = load('26_Bhy_1595031_1655030_[200903_122115]_[200903_122345].mat',
'AtaletselIvmeOlcerPitch');
T = T.AtaletselIvmeOlcerPitch;
U = load('27_Bhy_1655031_1715030_[200903_122345]_[200903_122614].mat',
'AtaletselIvmeOlcerPitch');
U = U.AtaletselIvmeOlcerPitch;
V = load('28_Bhy_1715031_1775030_[200903_122614]_[200903_122844].mat',
'AtaletselIvmeOlcerPitch');
V = V.AtaletselIvmeOlcerPitch;
W = load('23_Bhy_1415031_1475030_[200903_121345]_[200903_121615].mat',
'AtaletselIvmeOlcerPitch');
W = W.AtaletselIvmeOlcerPitch;
X = load('29_Bhy_1775031_1835030_[200903_122844]_[200903_123115].mat',
'AtaletselIvmeOlcerPitch');
X = X.AtaletselIvmeOlcerPitch;
Y = load('30_Bhy_1835031_1895030_[200903_123115]_[200903_123345].mat',
'AtaletselIvmeOlcerPitch');
Y = Y.AtaletselIvmeOlcerPitch;
Z = load('31_Bhy_1895031_1955030_[200903_123345]_[200903_123615].mat',
'AtaletselIvmeOlcerPitch');
Z = Z.AtaletselIvmeOlcerPitch;
```

```matlab
AA = load('32_Bhy_1955031_2015030_[200903_123615]_[200903_123845].mat',
'AtaletselIvmeOlcerPitch');
AA = AA.AtaletselIvmeOlcerPitch;
AB = load('33_Bhy_2015031_2075030_[200903_123845]_[200903_124115].mat',
'AtaletselIvmeOlcerPitch');
AB = AB.AtaletselIvmeOlcerPitch;
AC = load('34_Bhy_2075031_2135030_[200903_124115]_[200903_124345].mat',
'AtaletselIvmeOlcerPitch');
AC = AC.AtaletselIvmeOlcerPitch;
AD = load('35_Bhy_2135031_2195030_[200903_124345]_[200903_124614].mat',
'AtaletselIvmeOlcerPitch');
AD = AD.AtaletselIvmeOlcerPitch;
AE = load('36_Bhy_2195031_2255030_[200903_124614]_[200903_124844].mat',
'AtaletselIvmeOlcerPitch');
AE = AE.AtaletselIvmeOlcerPitch;
AF = load('37_Bhy_2255031_2315030_[200903_124844]_[200903_125115].mat',
'AtaletselIvmeOlcerPitch');
AF = AF.AtaletselIvmeOlcerPitch;
accel = zeros(1, 1920000);
for i=1:60000
    accel(i) = A(i);
end
for i=60001:120000
    accel(i) = B(i-60000);
end
for i=120001:180000
    accel(i) = C(i-120000);
end
for i=180001:240000
    accel(i) = D(i-180000);
end
for i=240001:300000
    accel(i) = E(i-240000);
end
for i=300001:360000
    accel(i) = F(i-300000);
end
for i=360001:420000
    accel(i) = G(i-360000);
end
for i=420001:480000
    accel(i) = H(i-420000);
end
for i=480001:540000
    accel(i) = I(i-480000);
end
```

```
for i=540001:600000
    accel(i) = J(i-540000);
end
for i=600001:660000
    accel(i) = K(i-600000);
end
for i= 660001:720000
    accel(i) = L(i-660000);
end
for i=720001:780000
    accel(i) = M(i-720000);
end
for i=780001:840000
    accel(i) = N(i-780000);
end
for i=840001:900000
    accel(i) = O(i-840000);
end
for i=900001:960000
    accel(i) = P(i-900000);
end
for i=960001:1020000
    accel(i) = Q(i-960000);
end
for i=1020001:1080000
    accel(i) = R(i-1020000);
end
for i=1080001:1140000
    accel(i) = S(i-1080000);
end
for i=1140001:1200000
    accel(i) = T(i-1140000);
end
for i=1200001:1260000
    accel(i) = U(i-1200000);
end
for i=1260001:1320000
    accel(i) = V(i-1260000);
end
for i=1320001:1380000
    accel(i) = W(i-1320000);
end
for i=1380001:1440000
    accel(i) = X(i-1380000);
end
for i=1440001:1500000
```

```matlab
    accel(i) = Y(i-1440000);
end
for i=1500001:1560000
    accel(i) = Z(i-1500000);
end
for i=1560001:1620000
    accel(i) = AA(i-1560000);
end
for i=1620001:1680000
    accel(i) = AB(i-1620000);
end
for i=1680001:1740000
    accel(i) = AC(i-1680000);
end
for i=1740001:1800000
    accel(i) = AD(i-1740000);
end
for i=1800001:1860000
    accel(i) = AE(i-1800000);
end
for i=1860001:1920000
    accel(i) = AF(i-1860000);
end
accel32 = zeros(60000,32);
for i=1:32
    accel32(:,i) = accel(60000*(i-1)+1:60000*i); %Filling the 60000 x 32 matrix of
equal segments column by column
end
%Applying the Run Test
musqr = zeros(1,32);
sigmasqr = zeros(1,32);
psisqr = zeros(1,32);
for i=1:32
    musqr(i) = (mean(accel32(:,i),'omitnan')).^2;
    sigmasqr(i) = var(accel32(:,i),'omitnan');
    psisqr(i) = musqr(:,i) + sigmasqr(:,i);
end
psimean = mean(psisqr);
str = zeros(1,32);
for i=1:32
    if psisqr(i) >= psimean
        str(i) = 1;
    else
        str(i) = 0;
    end
end
```

```matlab
%For 32 samples, the data are considered stationary if the number of runs
%(a successive occurrence of 1's or 0's) is between 11 and 22 (from the
%table of percentage points of run distribution in the lecture notes)
%Applying the Reverse Arrangements Test
revar = zeros(1,32);
for i=1:32
    for j=i+1:32
        if psisqr(i)>psisqr(j)
            revar(i) = revar(i) + 1;
        else
            revar(i) = revar(i) + 0;
        end
    end
end
rev = sum(revar);
%For 32 samples, the data are considered stationary by the reverse
%arrangements test if the sum is between 201 and 302.
```

B. The Tables Used in Stationarity Tests and Additional Information About These Tests

Table B.1. Percentage Points of Run Distribution

Percentage Points of Run Distribution						
Values of $r_{n;\alpha}$ such that $Prob[r_n > r_{n;\alpha}] = \alpha$, where $n = N_1 = N_2 = N/2$						
	α					
$n = N/2$	0.99	0.975	0.95	0.05	0.025	0.01
5	2	2	3	8	9	9
6	2	3	3	10	10	11
7	3	3	4	11	12	12
8	4	4	5	12	13	13
9	4	5	6	13	14	15
10	5	6	6	15	15	16
11	6	7	7	16	16	17
12	7	7	8	17	18	18
13	7	8	9	18	19	20
14	8	9	10	19	20	21
15	9	10	11	20	21	22
16	10	11	11	22	22	23
18	11	12	13	24	25	26
20	13	14	15	26	27	28
25	17	18	19	32	33	34
30	21	22	24	37	39	40
35	25	27	28	43	44	46
40	30	31	33	48	50	51
45	34	36	37	54	55	57
50	38	40	42	59	61	63

Table B.1 (cont'd)						
55	43	45	46	65	66	68
60	47	49	51	70	72	74
65	52	54	56	75	77	79
70	56	58	60	81	83	85
75	61	63	65	86	88	90
80	65	68	70	91	93	96
85	70	72	74	97	99	101
90	74	77	79	102	104	107
95	79	82	84	107	109	112
100	84	86	88	113	115	117

The Method for the Run Test:

If the number of 1's ("plus" observations where the data point is equal to or higher than average) is equal to the number of 0's ("minus" observation where the data point is less than average), then the Run Test can be employed to determine stationarity of the data set. For this test, first the number of "runs" is found. A "run" is an uninterrupted sequence of only 0's or only 1's. If the number of runs is between the values indicated on the third and fourth columns of Table B.1 for half the number of data samples, then the data set is said to be stationary according to the Run Test. However, if the numbers of "plus" and "minus" observations in a data set are not equal; then the Run Test cannot be applied reliably to this data set. This limits the applicability of the Run Test considerably. Thus, the Reverse Arrangements Test has emerged as an alternative method for determining stationarity.

Table B.2. Percentage Points of Reverse Arrangement Distribution

Percentage Points of Reverse Arrangement Distribution						
Values of $A_{n;\alpha}$ such that $Prob[A_N > A_{N;\alpha}] = \alpha$, where $N = $ total number of measurements						
	α					
N	0.99	0.975	0.95	0.05	0.025	0.01
10	9	11	13	31	33	35
12	16	18	21	44	47	49
14	24	27	30	60	63	66
16	34	38	41	78	81	85
18	45	50	54	98	102	107
20	59	64	69	120	125	130
30	152	162	171	263	272	282
40	290	305	319	460	474	489
50	473	495	514	710	729	751
60	702	731	756	1013	1038	1067
70	977	1014	1045	1369	1400	1437
80	1299	1344	1382	1777	1815	1860
90	1668	1721	1766	2238	2283	2336
100	2083	2145	2198	2751	2804	2866

Applying linear interpolation between 30 and 40 samples for 32 samples at $\alpha = 0.95$:

$171 + (319\text{-}171)*((32\text{-}30)/(40\text{-}30)) = 200.6$, which is rounded to 201.

Applying linear interpolation between 30 and 40 samples for 32 samples at $\alpha = 0.05$:

$263 + (460\text{-}263)*((32\text{-}30)/(40\text{-}30)) = 302.4$, which is rounded to 302.

So, in order for a set of 32 samples to satisfy the reverse arrangement stationarity test with a confidence level of 95%, the obtained sum should be between 201 and 302.